

# **Towards Clinico-Pathological Application of Raman Spectroscopy**

*Senada Koljenović*

Cover design:

Raoul Guillermo Wijdenbosch en Senada Koljenović

ISBN 978-90-8559-360-7

Layout and printing:

Optima Grafische Communicatie, Rotterdam, The Netherlands

# Towards Clinico-Pathological Application of Raman Spectroscopy

Op weg naar klinisch-pathologische toepassing  
van Raman spectroscopie

**Proefschrift**

ter verkrijging van de graad van doctor aan de  
Erasmus Universiteit Rotterdam  
op gezag van de  
rector magnificus

Prof.dr. S.W.J. Lamberts  
en volgens besluit van het College voor Promoties.

De openbare verdediging zal plaatsvinden op  
donderdag 20 maart 2008 om 13:30 uur  
door

Senada Koljenović  
Geboren te Ivangrad, Montenegro



**Promotiecommissie**

**Promotoren:**

Prof.dr. H.A.M. Neumann

Prof.dr. J.M. Kros

**Copromotor:**

Dr.ir. G.J. Puppels

**Overige leden:**

Prof.dr. C.J.J. Avezaat

Prof.dr. F.T. Bosman

Prof.dr. A.F.W. van der Steen

*Voor mijn mooie Ramannen en Ramannieke*



## Contents

<b>Chapter 1</b>	Introduction	9
	1.1 Monitoring pathological changes	11
	1.2 Raman spectroscopy	12
	1.3 Raman instrumentation	16
	1.4 Scope of this thesis	18
<b>Chapter 2</b>	Raman microspectroscopic mapping studies of human bronchial tissue.	25
<b>Chapter 3</b>	Detection of meningioma in dura mater by Raman spectroscopy	45
<b>Chapter 4</b>	Discriminating vital tumor from necrotic tissue in human glioblastoma tissue samples by Raman spectroscopy	63
<b>Chapter 5</b>	Tissue characterization using high wave number Raman spectroscopy	83
<b>Chapter 6</b>	Fiber-optic probes for <i>in vivo</i> Raman spectroscopy in the high wavenumber region	105
<b>Chapter 7</b>	Raman spectroscopic characterization of porcine brain tissue using a single fiber-optic probe.	119
<b>Chapter 8</b>	Summary and general discussion	137
	Samenvatting en algemene discussie	145
	Sažetak i diskusija	151
	Curriculum vitae	159
	Publications	161



# Introduction

1



## 1.1 Monitoring Pathological Changes

As the possibilities in the treatment of diseases continue to evolve, early detection and correct diagnosis of pathological changes have become increasingly important. Pathology literally means the study (logos) of suffering (pathos), and it is essentially the discipline that bridges basic science and clinical practice by studying the structural and functional changes in diseased cells, tissues and organs. The focus of diagnostic pathology is to label the morphological and molecular changes in cells and tissues so that the appropriate therapeutic action can be taken. Histopathology is still the “gold standard” of assessing abnormal changes in tissues. In order to make a pathological diagnosis, it is required that changes in the tissues available for evaluation are representative of the disease. Tissue samples are usually obtained by biopsy procedures. Because usually only limited real-time information is available regarding the nature of the tissues to be sampled, sampling errors tend to occur. Another risk induced by lack of real-time information about the nature of diseased tissues, as compared to their normal environment, is incomplete surgical removal of tumor tissue. Therefore, the identification of biochemical characteristics of tissues which are indicative of a particular abnormality or disease and subsequent incorporation of such characteristics in sampling procedures will improve diagnostic accuracy. The same accuracy may assist surgeons in more precise targeting and removing of lesions.

Over the last decades, computed tomography/ magnetic resonance imaging (CT/ MRI)-based devices significantly assist in localizing lesions and have thereby decreased sampling errors. In addition, the safety of surgical procedures has improved because information about the local anatomy. However, these techniques provide only limited information about the histological composition of tissues. Although magnetic resonance spectroscopy (MRS) has proven to be valuable in the diagnosis of brain tumors<sup>1-8</sup> and has provided insights in particular metabolic abnormalities caused by neurodegenerative diseases<sup>9</sup>, its clinical use has been impeded by various factors such as poor signal quality, long acquisition time and difficulties in the interpretation of spectra.<sup>8</sup> Most available systems for image-guided (neuro) surgery are based on three-dimensional brain models calculated from CT and/ or MR images acquired before the operation. These systems do not take into account the dynamic changes that occur during the surgical procedures (e.g., brain shift due to edema, tissue removal and loss of cerebrospinal fluid). The precise targeting of lesions is impaired and the risk of damaging healthy tissues may increase. Recently, intraoperative MRI navigation systems have been promoted as powerful tools for the guidance of (neuro) surgical procedures.<sup>10-22</sup> However, widespread use of such systems is hampered by the high costs and the large size of the equipment and the need for MR-compatible surgical devices.<sup>18</sup>

Changes in the structure and molecular composition of pathologically altered tissues may well provide opportunities for the development of tools for guiding diagnostic and therapeutic procedures. Examples are optical spectroscopic techniques which have shown to be

promising for the characterization of tissues. The application of autofluorescence imaging has improved the sensitivity of detection of early epithelial neoplasia in oesophagus and colon.<sup>23-29</sup> Furthermore, autofluorescence bronchoscopy has significantly increased the diagnostic sensitivity for pre-malignant stages of lung cancer (e.g., dysplasia and carcinoma *in situ*).<sup>30-33</sup> The subject of this thesis is the realization of an *in vivo* Raman spectroscopic method for real-time guidance during diagnostic and/or therapeutic medical procedures. Raman spectroscopy has proven to be a powerful tool for tissue characterization in a great number of *ex vivo* studies. A number of studies have reported on Raman spectral differences between normal tissue and tumors of the skin, colon, larynx, cervix and breast, based on differences in their biochemical composition.<sup>34-41</sup> So far, successful steps towards *in vivo* application of the technique by means of fiber-optic probes have been taken. For instance, Mahadevan-Jansen *et al.* collected *in vivo* spectra from human cervical tissue for the clinical diagnosis of cervical precancers<sup>42</sup>, Buschman *et al.* and Motz *et al.* obtained *in vivo* intravascular Raman spectra from arteries.<sup>43,44</sup> Bakker Schut *et al.* reported on the *in vivo* detection of epithelial dysplasia in rat palate tissue<sup>45</sup>, and Haka *et al.* collected *in vivo* Raman spectra for margin assessment during partial breast resection.<sup>46</sup> Recently, the potential of near-infrared Raman spectroscopy using optical fiber probes for the diagnosis of lung cancer<sup>47</sup> and the differentiation of colonic polyps during gastro intestinal endoscopy<sup>48</sup> was demonstrated. Various miniaturized fiber-optic probes have been designed and successfully applied,<sup>49-51</sup> and high quality *in vivo* Raman spectra were obtained. Bakker Schut *et al.* and later Motz *et al.* have demonstrated that real-time interpretation of *in vivo* spectra is feasible.<sup>52,53</sup>

## 1.2 Raman Spectroscopy

### Raman Effect

Light interacts with molecules through elastic and inelastic light scattering process. In an elastic light scattering process, the scattered light has the same wavelength as the incident light. An example is Rayleigh scattering. In an inelastic light scattering process energy is exchanged between incident light and the molecules. This leads to changes in wavelength of the scattered light (Figure 1). Raman scattering is an inelastic scattering process in which vibrational modes in molecules are excited by the interaction with the incident light.

The Raman effect is divided into Stokes (Figure 2B) and anti-Stokes (Figure 2C) shifts. In case of a Stokes shift, a molecule is excited to a higher vibrational energy level and the energy of the scattered photon decreases. Consequently, the scattered light has a longer wavelength. An anti-Stokes shift occurs when a molecule relaxes to a lower vibrational energy level and transfers energy to the incident photon. This latter process, whereby the scattered light has a shorter wavelength than the incident light, is less efficient at room temperature. Stokes

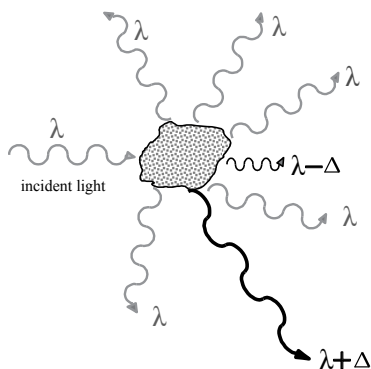


**Figure 1.** Schematic representation of the interaction of light and matter. The major fraction of incident light with wavelength  $\lambda$  is scattered with the identical wavelength (Rayleigh scattering). A small fraction of the incident light however, is scattered at altered wavelengths due to so-called inelastic light scattering, in which energy is exchanged between an incident photon and the molecule.

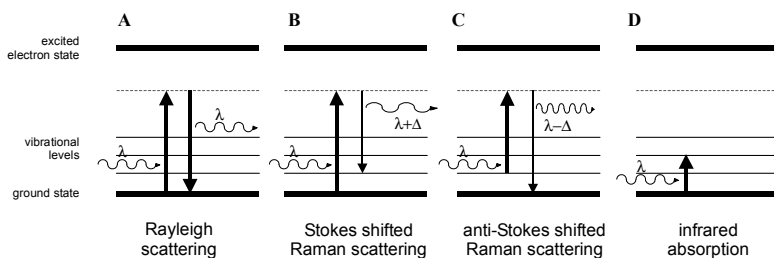


**Figure 2.** Energy level diagrams showing **A)** elastic scattering (Rayleigh), **B)** en **C)** inelastic scattering (Stokes and anti-Stokes, resp.) and **D)** infrared absorption (IR).

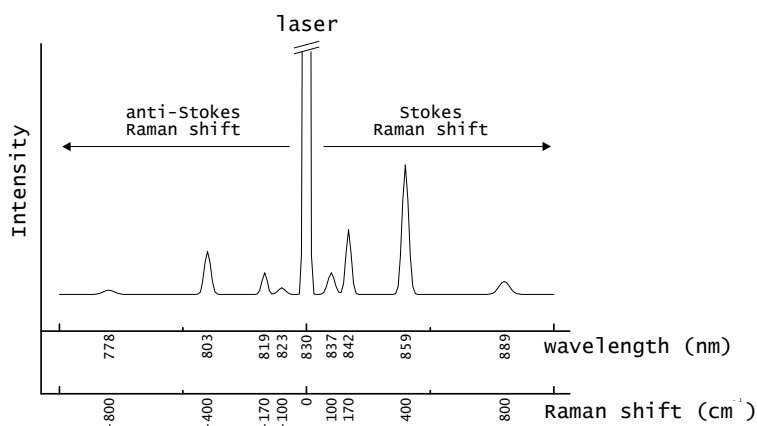


**Figure 3.** A theoretical Raman spectrum with the Stokes and anti-Stokes shifted Raman lines symmetrically distributed around the laser line (in this example 830 nm).

shifted Raman signals are more intense and are used in the projects of this thesis. For comparison, Figure 2D shows the absorption process on which infrared spectroscopy is based.

In order to precisely monitor the changes in wavelength between incident and scattered light, monochromatic light from a laser is used to obtain a Raman signal from a sample. Figure 3 is a schematic representation of a Raman spectrum, where the Stokes and anti-Stokes lines are symmetrically positioned around the Rayleigh scattered light from the laser.

The x-axis corresponds to the wavelength of the different Raman peaks in a spectrum, and is given in relative wavenumbers or Raman shift units. Raman shifts are calculated according to the formula:

$$\Delta cm^{-1} = \left( \frac{1}{\lambda_0} - \frac{1}{\lambda_s} \right) * 10^{-2}$$

Where  $\lambda$  is in meters (m),  $\lambda_0$  stands for excitation wavelength, and  $\lambda_s$  stands for wavelength of scattered light.

The position of a line in the Raman spectrum corresponds to the energy that is required to excite a molecule to a certain vibrational energy level. A molecule can have up to  $3N-6$  independent vibrational modes ( $3N-5$  for linear molecules), where  $N$  is the number of atoms in the molecule.<sup>54</sup> Many of these can be Raman-active, depending on molecular structure.

## History of Raman Spectroscopy

Raman spectroscopy is named after its discoverer, the Indian physicist Chandrasekhara Venkata Raman. In 1928, in a lecture about a new type of light scattering, he said: *"We are obviously at the fringe of a fascinating new region of experimental research, which promises to throw light on diverse problems relating to radiation and wave theory, X-ray optics, atomic and molecular spectra, fluorescence and scattering, thermodynamics and chemistry. It all remains to be worked out"*. Raman and his co-worker K. S. Krishnan had observed that when a liquid sample was irradiated by an intense light source, a fraction of the scattered light had a wavelength different from the wavelengths of the incident light. The shift in wavelength was associated with a change in the rotational and vibrational energy and therefore gave information about the energy levels of the irradiated molecules, correlating with the molecular structure. This phenomenon had been predicted on theoretical grounds five years earlier by Adolf G. Smekal.<sup>55</sup> With their publication in Nature<sup>56</sup> Raman and Krishnan were the first to publish experimental evidence for the phenomenon. At the same time in Moscow, G.S Landsberg and L.I. Mandel'shtam had discovered the light scattering phenomenon independently from Raman and Krishnan in Calcutta, but their study was published just a few months after Ra-

man and Krishnan's.<sup>57</sup> The phenomenon was called the 'Raman effect' and for this discovery Raman received the Nobel Prize in Physics in 1930.

There was great interest in the new phenomenon and numerous publications devoted to the Raman effect appeared in the first decade after its discovery. However, the popularity of Raman spectroscopy as an analytical method gradually declined. Two reasons for the decreasing interest were that Raman spectroscopy is a relatively inefficient scattering process and that Raman signals are very weak. Raman spectroscopy requires an intense monochromatic light source and sensitive detection equipment, for which spectroscopists at that time used a mercury lamp and photographic paper and exposure times of hours or even days. Due to the technical hurdles and the development of Infrared Spectroscopy, which was closely related to Raman spectroscopy but technically more simple to apply, researchers lost interest in Raman spectroscopy and Infrared Spectroscopy became the dominant vibrational spectroscopic technique after the Second World War.

Nevertheless, interest in Raman spectroscopy was re-established with the invention of the laser in the 1960s. Laser is a powerful, highly monochromatic light source that can easily be focused and enables irradiation of a sample with high intensity. Another step forward was the development of electronic measuring devices such as photomultiplier tubes and photodiode arrays, which provided sensitive detectors for the relatively weak Raman signals. Tedious work with photographic film and extremely long exposure times could now be abandoned. Today, Raman spectroscopy has become a well-established technique with widespread application in many fields.

Since the 1980's, the possibility of using Raman as a medical diagnostic device has been the topic of a growing number of papers. Databases of Raman spectra of different tissues have been collected and used to build multivariate statistical models to be used (in real-time) to discriminate between different normal and diseased tissues.

With the development of smaller and more efficient lasers, more sensitive and flexible detection equipment, and faster computers, the technique is now entering the clinical realm.

## Raman Spectroscopic Analysis of Cells and Tissues

An individual peak in a Raman spectrum corresponds to a molecular vibration and consequently, a Raman spectrum, containing many vibrational bands, is highly specific for that particular molecule (Figure 4A). Raman spectra of cells and tissues are very complex because all molecules contribute to the overall Raman spectrum of the cell or tissue. However, based on the known Raman spectra of purified compounds, in many cases peaks in a spectrum of a cell or tissue can be assigned to particular cellular constituents (Figure 4B). Therefore, it is possible to acquire detailed qualitative and quantitative information regarding the molecular composition of tissues on the basis of their Raman spectrum.<sup>58-60</sup>

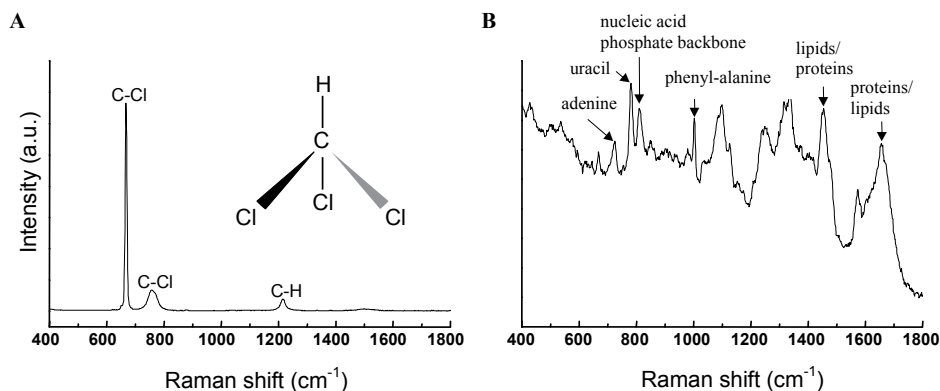


**Figure 4.** Examples of Raman spectra. A: spectrum of chloroform. This small molecule produces a relatively simple Raman spectrum. The peaks in the spectrum can be attributed to specific vibrations within the molecule. B: Raman spectrum of the bacterium *Enterococcus faecium*. Due to the complex molecular composition of the sample involved, a complex Raman spectrum is obtained. Based on the Raman spectra of purified compounds, spectral features can be assigned to specific molecular moieties in the bacterial cell. Some typical vibrations are indicated.

When it is not possible to assign peaks in the tissue spectrum to particular biochemical components, Raman spectra can still be used as highly specific spectroscopic fingerprints, enabling the identification of tissues. Different tissues will differ in their overall molecular composition and because Raman spectra reflect this overall molecular composition, their Raman spectra will also be different. Pathological changes in molecular composition or structure are reflected in the spectra, enabling development of diagnostic tools based on Raman spectroscopy.

The Raman spectroscopic information is contained in two spectral regions: the 400-2000  $\text{cm}^{-1}$  spectral interval, often referred to as the fingerprint region, which is very rich in spectroscopic information, and the 2000-4000  $\text{cm}^{-1}$  region, or high wavenumber region (hereafter referred to as HWVN), which contains the CH-, OH-, and NH-stretching vibrations. Figure 5 shows examples of Raman spectra from both regions.

### 1.3 Raman Instrumentation

The current instrumentation required for Raman measurements is relatively simple. High power monochromatic light for excitation is obtained from a laser and a cooled CCD camera is used for sensitive low-noise recording of the generated Raman spectrum. In the research described in this thesis, two types of Raman setups were used, differing in the way that the light is guided to and from the tissue.

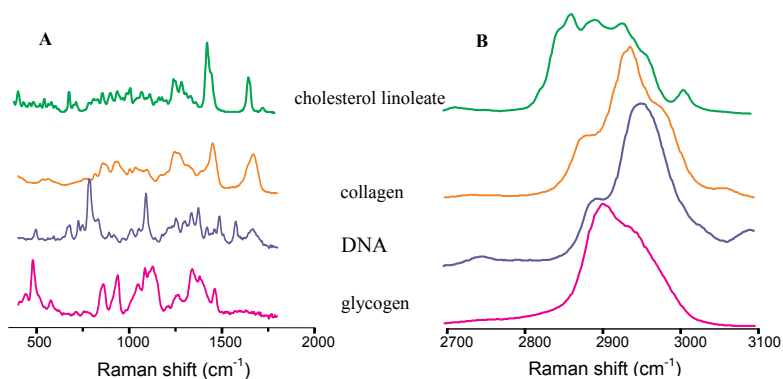


**Figure 5.** Raman spectra of commercially available pure chemical compounds, obtained in fingerprint region (A) and in high wave number region (B).

### *In Vitro* Microscope Setup

The instrument used throughout the *in vitro* mapping measurements presented here (Chapters 2, 3, 4 and 5), consists of a confocal microscope attached to a spectrometer, which a confocal Raman microspectrometer (Figure 6). Laser light is focused on the sample by a microscope objective which also collects backscattered light from the sample. The backscattered light is coupled out of the microscope, filtered to remove the laser light, and guided to a spectrometer where the Raman light is dispersed and imaged on a CCD camera.

Applying a confocal signal collection geometry allows for small measurement volumes to be used.<sup>61</sup> The setup is optimized to measure cells and thin tissue sections of about 20 microns thickness. Furthermore, the setup was automated to collect Raman maps of the sample by performing a scan of the sample whereby sequential confocal measurements were carried out on different x-y positions. By moving the x and y direction translation stage according to a predefined grid and taking a Raman spectrum on each position, a multidimensional data set is acquired. Multivariate statistical techniques are used to extract the relevant biochemical information for each point of the map and to generate contrast in a Raman image of the sample.

### *In Vivo* Fiber-Optic Probe Setup

In the experiments in which fiber-optic probes are used (Chapters 5, 6 and 7 of this thesis) laser light is focused in the core of an optical fiber. The fiber guides the laser light to the sample at the distal end of the fiber. Backscattered laser light and Raman-scattered light from the sample are collected by the same fiber, guided back to the proximal end of the fiber, collimated again and guided into a spectrometer.

Depending on the type of fiber used and the shaping of the probe tip, the probe has an illumination cross section of 50 to 200 microns and it collects Raman scattered light from

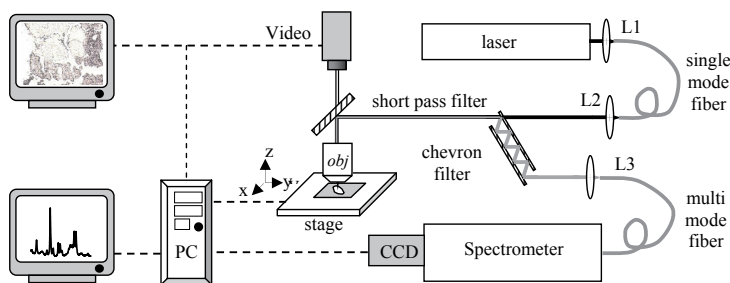


**Figure 6.** Schematic representation of the Raman microscope setup used in the *in vitro* experiments. Light from a Argon pumped Ti:Sapph laser is delivered through a mono-mode fiber to the setup (using lenses L1 and L2 to couple the light in and out respectively). The light is coupled into the microscope objective (*obj*) of a Leica microscope using a short pass filter. The light that is scattered from the sample is coupled out the same way and is then filtered using a chevron type filter to remove the laser light. The light is then focused using lens L3 on a multi-mode fiber which acts as the entrance pinhole for the spectrometer. The spectrometer disperses the Raman light on the CCD camera, and the recorded spectra are acquired using a personal computer (PC). Both the stage and objective of the microscope are automated and can be controlled by the PC. A video camera is used to display a visual image of the sample which can also be recorded by the PC.

the first 100 to 500 microns of tissue. The physical dimensions of the probes are such that they can easily be used in auxiliary channels of endoscopes, cystoscopes, bronchoscopes, biopsy needles etc., which makes the technique suitable for many *in vivo* applications.

## 1.4 Scope of This Thesis

A number of characteristic features of Raman spectroscopy make this nondestructive technique particularly appealing for application in clinico-pathological settings. Because no dyes, labels or other contrast enhancing agents are required for obtaining Raman spectra, tissues can be studied in their native states. Moreover, *in vivo* Raman spectroscopy may help the clinician to target lesions more precisely and thereby provide the pathologist with representative tissue samples for making a diagnosis. Complete removal of lesions while sparing healthy tissues during surgical procedures may be improved by the application of Raman spectroscopy. The main aim of the studies in this thesis was to develop an *in vivo* Raman method for the real-time characterization of tissues. We first investigated whether Raman spectroscopy enables the characterization of normal tissues, the discrimination of tumor tissue from its normal environment, and the identification of different components within a tumor. These issues were addressed by *in vitro* studies that were performed using a Raman-based microspectroscopic setup. Raman mapping experiments were performed on frozen sections of normal bronchial tissue, on meningioma and dura tissue and on

glioblastoma tissue (Chapters 2, 3 and 4). By precise linking of the spectral features with the histological structures, information about the (differences in) biochemical composition of these structures was revealed. A spectral data set of healthy bronchial tissues was established, which may serve as a starting point for future *in vivo* studies in which normal tissues will be discriminated from their premalignant and malignant counterparts. Furthermore, multivariate analysis models were developed for delineation of meningioma from normal dura tissue, which will serve as the basis for real-time assessment of resection margins in surgical removal of meningioma. The heterogeneity of glioblastoma tissue was probed in order to identify the possibilities for the *in vivo* use of Raman spectroscopy for real-time biopsy guidance. A multivariate analysis-based classification model was built that distinguishes viable glioblastoma tissue from necrotic tissue with 100% accuracy. For all of these Raman mapping experiments, the fingerprint spectral region was used because this region is very informative about the biochemical composition of the tissues.

Proof-of-concept of Raman-based technology for the development of clinical diagnostics guidance tools has been reached.<sup>49,51</sup> However, the actual *in vivo* implementation of conventional Raman spectroscopy for clinical purposes is hampered by the fact that in the 400-2000  $\text{cm}^{-1}$  spectral region, intense Raman scattering is generated in the optical fiber itself. This results in a strong background signal, which weakens the signal obtained from the tissue at the end of the fiber. In order to filter out this background signal, complex probe designs are necessary. Unfortunately, the complexity of a probe usually reduces the flexibility which is required for intravascular<sup>43</sup> or intra-cerebral use (i.e., stereotactic brain biopsy). Using the device in an auxiliary channel of an endoscope is hampered<sup>48</sup> and reproducibility of performance is also reduced.<sup>52</sup> The technological hurdle of designing and constructing suitable fiber-optic probes is eliminated by using the HWVN region (2000-4000  $\text{cm}^{-1}$ ) for detection. Because in this spectral region no Raman signal is generated in the fiber itself, a simple standard optical fiber can be used to guide laser light to the tissue and to collect scattered light. In previous studies it was shown that HWVN Raman spectroscopy can be used to determine water concentration in skin and in brain tissue and to obtain information on the compositional heterogeneity of atherosclerotic plaques.<sup>59,62,63</sup> Here we demonstrate that the spectra obtained in the HWVN region contain essentially the same diagnostic information as those obtained from the fingerprint region of the Raman spectrum (Chapter 5). This implies that an important technological problem obstructing the *in vivo* diagnostic application of Raman spectroscopy is eliminated. Based on these results, we have developed a setup for remote Raman spectroscopic tissue characterization during clinical procedures (Chapter 6). The setup consists of a single, unfiltered, optical fiber for guiding laser light to the sample and for collecting scattered light and guiding it back to a spectrometer. This approach was tested on normal, fresh porcine brain tissue (Chapter 7). A spectral data set of various brain parts was created that may serve as the basis for *in vivo* discrimination between different normal brain areas. In future studies, this preliminary work may pave the way for identification and delineation of pathologically altered brain parts.

## References

1. Dowling C, Bollen AW, Noworolski SM, McDermott MW, Barbaro NM, Day MR, Henry RG, Chang SM, Dillon WP, Nelson SJ, Vigneron DB. *Preoperative proton MR spectroscopic imaging of brain tumors: correlation with histopathologic analysis of resection specimens.* Am J Neuroradiol 2001; 22: 604-612.
2. Fountas KN, Kapsalaki EZ, Gotsis SD, Kapsalakis JZ, Smisson HF, Johnston KW, Robinson JS, Papadakis N. *In vivo Proton Magnetic Resonance Spectroscopy of brain tumor.* Stereotact Funct Neurosurg 2000; 74: 83-94.
3. Hall WA, Martin AJ, Lui H, Truwit CL. *Improving diagnostic yield in brain biopsy: coupling spectroscopic targeting with real-time needle placement.* Journal of Magnetic Resonance imaging 2001; 13: 12-15.
4. Hall WA, Lui H, Truwit CL, Martin AJ. *Comparison of stereotactic brain biopsy to interventional Magnetic-Resonance-Imaging-guided brain biopsy.* Stereotact Funct Neurosurg 1999; 73: 148-153.
5. Kurhanewicz J, Vigneron DB, Nelson SJ. *Three-dimensional Magnetic Resonance Spectroscopic Imaging of brain and prostate cancer.* Neoplasia 2000; 2: 166-189.
6. Nygren C, von Holst H, Månsson J-E, Fredman P. *Increased levels of cholesterol esters in glioma tissue and surrounding areas of human brain.* Br J Neurosurg 1997; 11: 216-220.
7. Vigneron D, Bollen A, McDermott M, Wald I, Day M, Moyher-Noworolski S, Henry R, Chang S, Berger M, Dillon W, Nelson S. *Three-dimensional magnetic resonance spectroscopic imaging of histologically confirmed brain tumors.* Magn Reson Imaging 2001; 19: 89-101.
8. Sibtain NA, Howe FA, Saunders DE. *The clinical value of proton magnetic resonance spectroscopy in adult brain tumours.* Clinical Radiology 2007; 62: 109-119.
9. Martin WR. *MR Spectroscopy in Neurodegenerative Disease.* Mol Imaging Biol 2007; 9: 196-203.
10. Black PM, Moriarty T, Alexander E, Stieg P, Woodard E, Gleason PL, Martin CH, Kikinis R, Schwartz RB, Jolesz FA. *Development and implementation of intraoperative magnetic resonance imaging and its neurosurgical applications.* Neurosurgery 1997; 41: 831-845.
11. Seifert V, Zimmermann M, Trantakis C, Vitzthum H-E, Kühnel K, Raabe A, Bootz F, Schneider J-P, Schmidt F, Dietrich J. *Open MRI-guided neurosurgery.* Acta Neurochir (Wien) 1999; 141: 455-464.
12. Zimmermann M, Seifert V, Trantakis C, Kühnel K, Raabe A, Schneider J-P, Dietrich J, Schmidt F. *Open MRI-guided microsurgery of intracranial tumours. Preliminary experience using a vertical open MRI-scanner.* Acta Neurochir (Wien) 2000; 142: 177-186.
13. Zimmermann M, Seifert V, Trantakis C, Raabe A. *Open MRI-guided microsurgery of intracranial tumours in or near eloquent brain areas.* Acta Neurochir (Wien) 2001; 143: 327-337.
14. Nimsky C, Ganslandt O, Cerny S, Hastreiter P, Greiner G, Fahlbusch R. *Quantification of, visualization of, and compensation for brain shift using intraoperative magnetic resonance imaging.* Neurosurgery 2000; 47: 1070-1080.
15. Nimsky C, Ganslandt O, Hastreiter P, Fahlbusch R. *Intraoperative magnetic resonance imaging combined with neuronavigation: a new concept.* Surg Neurol 2001; 56: 357-65.
16. Hastreiter P, Rezk-Salama C, Soza G, Bauer M, Greiner G, Fahlbusch R, Ganslandt O, Nimsky C. *Strategies for brain shift evaluation.* Med Image Anal 2004; 8: 447-464.
17. Albayrak B, Samdani AF, Black PM. *Intraoperative magnetic resonance imaging in neurosurgery.* Acta Neurochir (Wien) 2004; 146: 543-557.
18. Iseki H, Muragaki Y, Nakamura R, Ozawa N, Taniguchi H, Hori T, Takakura K. *Intelligent operating theater using intraoperative open-MRI.* Magn Reson Med Sci 2005; 4: 129-136.
19. Apuzzo ML, Sabshin JK. *Computed tomographic guidance stereotaxis in the management of intracranial mass lesions.* Neurosurgery 1983; 12: 277-285.

20. Barnett GK, Kormos DW, Steiner CP, Weisenberger J. *Use of a frameless, armless stereotactic wand for brain tumor localization with two-dimensional and three-dimensional neuroimaging.* Neurosurg 1993; 33: 674-678.
21. Dorward NL, Alberti O, Velani B, Gerritsen FA, Harkness WF, Kitchen ND, Thomas DG. *Postimaging brain distortion: magnitude, correlates, and impact on neuronavigation.* J Neurosurg. 1998; 88: 656-662.
22. Roberts DW, Hartov A, Kennedy FE, Miga MI, Paulsen KD. *Intraoperative brain shift and deformation: a quantitative analysis of cortical displacement in 28 cases.* Neurosurgery 1998; 43: 749-760.
23. Haringsma J, Tytgat GN, Yano H, Iishi H, Tatsuta M, Ogihara T, Watanabe H, Sato N, Marcon N, Wilson BC, Cline RW. *Autofluorescence endoscopy: feasibility of detection of GI neoplasms unapparent to white light endoscopy with an evolving technology.* Gastrointest Endosc 2001; 53: 642-50.
24. Bergman J. *Diagnosis and therapy of early neoplasia in Barrett's esophagus.* Curr Opin Gastroenterol 2005; 21: 466-71.
25. Moreto M. *Diagnosis of esophagogastric tumors.* Endoscopy 2005; 37: 26-30.
26. Wong Kee Song L-M, and Wilson B. C. 2005. *Endoscopic detection of early upper GI cancers.* Best Practice & Research Clinical Gastroenterology 19: 833-856.
27. DaCosta RS, Wilson BC, Marcon NE. *Optical techniques for the endoscopic detection of dysplastic colonic lesions.* Curr Opin Gastroenterol 2005; 21: 70-79
28. Kara MA, Bergman J. *Autofluorescence Imaging and Narrow-Band Imaging for the Detection of Early Neoplasia in Patients with Barrett's Esophagus.* Endoscopy 2006; 38: 627-631.
29. Dacosta RS, Wilson BC, Marcon NE. *Spectroscopy and fluorescence in esophageal diseases.* Best Pract Res Clin Gastroenterol 2006; 20: 41-57.
30. Lam S, Kennedy T, Unger M, Miller YE, Gelmont D, Rusch V, Gipe B, Howard D, LeRiche JC, Coldman A, Gazdar AF. *Localization of bronchial intraepithelial neoplastic lesions by fluorescence bronchoscopy.* Chest 1998; 113, 696-702.
31. Hirsch FR, Prindiville SA, Miller YE, Franklin WA, Dempsey EC, Murphy JR, Bunn Jr PA, Kennedy TC. *Fluorescence versus white-light bronchoscopy for detection of preneoplastic lesions: a randomized study.* J Nat Cancer Inst 2001; 93: 1385-1391.
32. Feller-Kopman D, Lunn W, Ernst A. *Autofluorescence Bronchoscopy and Endobronchial Ultrasound: A Practical Review.* Ann Thorac Surg 2005; 80: 2395-2401.
33. Read C, Janes S, George J, Spiro S. *Early Lung Cancer: screening and detection.* Prim Care Resp J 2006; 15: 332-336.
34. Mahadevan-Jansen A, Mitchell M.F, Ramanujam N, Malpica A, Thomasen S, Utzinger U, Richards-Kortum R. *Near-infrared Raman spectroscopy for in vitro detection of cervical precancers.* Photochem Photobiol 1998; 68: 123-132.
35. Manoharan R, Schafer K, Perelman L, Wu J, Chen K, Deinum G, Fitzmaurice M, Myles J, Crowe J, Dasari RR, Feld MS. *Raman spectroscopy and fluorescence photon migration for breast cancer diagnosis imaging.* Photochem Photobiol 1998; 67: 15-22.
36. Boustany NN, Crawford JM, Manoharan R, Dasari RR, Feld MS. *Analysis of nucleotides and aromatic amino acids in normal and neoplastic colon mucosa by ultraviolet resonance Raman spectroscopy.* Lab Invest 1999; 79: 1201-1214.
37. Nijssen A, Bakker Schut TC, Heule F, Caspers, Hayes DP, Neumann MH, Puppels GJ. *Discriminating basal cell carcinoma from its surrounding tissue by Raman spectroscopy.* J Invest Dermatol 2002; 119: 64-69.
38. Stone N, Kendall C, Shepherd N, Crow P, Barr H. *Near-infrared Raman spectroscopy for the classification of epithelial pre-cancers and cancers.* Journal of Raman spectroscopy 2002; 33: 564-573.

39. Haka AS, Shafer-Peltier KE, Fitzmaurice M, Crowe J, Dasari RR, Feld MS. *Diagnosing breast cancer by using Raman spectroscopy*. Proc Natl Acad Sci U S A 2005; 102: 12371-12376.
40. Lau DP, Huang Z, Lui H, Anderson D.W, Berean K, Morrison MD, Shen L, Zeng H. *Raman spectroscopy for optical diagnosis in the larynx: preliminary findings*. Lasers Surg Med 2005; 37: 192-200.
41. de Jong BW, Bakker Schut TC, Maquelin K, van der Kwast T, Bangma CH, Kok DJ, Puppels GJ. *Discrimination between nontumor bladder tissue and tumor by Raman spectroscopy*. Anal Chem 2006; 78: 7761-7769.
42. Mahadevan-Jansen A, Mitchell MF, Ramanujam N, Utzinger U, Richards-Kortum R. *Development of a fiber-optic probe to measure NIR Raman spectra of cervical tissue in vivo*. Photochem Photobiol 1998; 68: 427-431
43. Buschman R, Marple ET, Wach ML, Bennett B, Bakker Schut TC, Bruining HA, Bruschke AV, van der Laarse A, Puppels GJ. *In vivo determination of the molecular composition of artery wall by intravascular Raman spectroscopy*. Anal Chem 2000; 72: 3771-3775.
44. Motz JT, Fitzmaurice M, Miller A, Gandhi SJ, Haka AS, Galindo LH, Dasari RR, Kramer JR, Feld MS. *In vivo Raman spectral pathology of human atherosclerosis and vulnerable plaque*. J Biomed Opt 2006; 11: 021003.
45. Bakker Schut TC, Witjes M, Sterenborg M, Speelman O, Roodenburg J, Marple E, Bruining HA, Puppels GJ. *In vivo detection of dysplastic tissue by Raman spectroscopy*. Anal Chem 2000; 72: 6010-6018.
46. Haka AS, Volynskaya Z, Gardecki JA, Nazemi J, Lyons J, Hicks D, Fitzmaurice M, Dasari RR, Crowe JP, Feld MS. *In vivo margin assessment during partial mastectomy breast surgery using raman spectroscopy*. Cancer Res 2006; 66: 3317-3322.
47. Huang Z, McWilliams A, Lui H, McLean D, Lam DIS, Zeng H. *Near-infrared Raman spectroscopy for optical diagnosis of lung cancer*. Int J Cancer 2003; 107: 1047-1052.
48. Molckovsky A, Wong Kee Song L-M, Shim MG, Marcon NE, Wilson BC. *Diagnostic potential of near-infrared Raman spectroscopy in the colon: differentiating adenomatous from hyperplastic polyps*. Gastrointestinal Endoscopy 2003; 57: 396-402.
49. Motz JT, Hunter M, Galindo LH, Gradecki JA, Kramer JR, Dasari RR, Feld MS. *Optical fiber probe for biomedical Raman spectroscopy*. Appl Opt 2004; 20: 542-554.
50. Shim MG, Song LM, Marcon NE, Wilson BC. *In vivo near-infrared Raman spectroscopy*. Photochem Photobiol 2000; 72: 146-150.
51. Puppels GJ, van Aken M, Wolthuis R, Caspers PJ, Bakker Schut TC, Bruining HA, Romer TJ, Buschman HPJ, Wach M, Robinson JS. *In vivo tissue characterization by Raman spectroscopy*. Proc SPIE Biomed Soc 1998; 3257: 78-85.
52. Boere IA, Bakker Schut TC, van den Boogert J, de Bruin RWF, Puppels GJ. *Use of fiber-optic probes for detection of Barrett's epithelium in the rat oesophagus by Raman spectroscopy*. Vibrational Spectroscopy 2003; 32: 47-55.
53. Motz JT, Gandhi SJ, Scepanovic OR, Haka AS, Kramer JR, Dasari RR, Feld MS. *Real-time Raman system for in vivo disease diagnosis*. J Biomed Opt 2005; 10: 031113.
54. Tu AT. *Raman Spectroscopy in Biology*. John Wiley & Sons; Ltd., New York; 1982.
55. Smekal A. *Zur Quantentheorie der Dispersion*. Naturwissenschaften 1923; 11: 873-875.
56. Raman CV, Krishnan KS. *A new type of secondary radiation*. Nature 1928; 121 :501-502.
57. Landsberg GS, Mandelshtam L I. *Naturwissenschaften*1928; 16: 557.
58. Caspers PJ, Lucassen GW, Bruining HA, Puppels GJ. *Automated depth-scanning confocal Raman microspectrometer for rapid in vivo determination of water concentration profiles in human skin*. J Raman Spectrosc 2000; 31: 813-818.

59. Caspers PJ, Lucassen GW, Carter EA, Bruining HA, Puppels GJ. *In vivo confocal Raman microspectroscopy of skin: noninvasive determination of molecular concentration profiles*. J Invest Dermatol 2001; 116: 434-442.
60. van de Poll SW, Römer TJ, Volger OL, Delsing DJ, Bakker Schut TC, Princen HM, Havekes LM, Jukema JW, van der Laarse A, Puppels GJ. *Raman spectroscopic evaluation of the effects of diet and lipid-lowering therapy on atherosclerotic plaque development in mice*. Arterioscler Thromb Vasc Biol 2001; 21: 1630-1635.
61. Puppels GJ, de Mul FF, Otto C, Greve J, Robert-Nicoud M, Arndt-Jovin DJ, Jovin TM. *Studying single living cells and chromosomes by confocal Raman microspectroscopy*. Nature 1990; 347: 301-3.
62. Wolthuis R, van Aken M, Fountas K, Robinson Jr JS, Bruining HA, Puppels GJ. *Determination of water concentration in brain tissue by Raman spectroscopy*. Anal Chem 2001; 73: 3915-3920.
63. van de Poll SWE, Moelker A, Wolthuis R, Bakker Schut TC, Koljenović S, van der Laarse A, Puppels GJ. *Chemical characterization of atherosclerotic plaque by high-wavenumber Raman spectroscopy, (unpublished results)*.



# Raman Microspectroscopic Mapping Studies of Human Bronchial Tissue

*Journal of Biomedical Optics*  
2004, 9 (6): 1187-1197

2

S. Koljenović  
T.C. Bakker Schut  
J.P. van Meerbeeck  
A.P. Maat  
S.A. Burgers  
P.E. Zondervan  
J.M. Kros  
G.J. Puppels

## Abstract

Characterization of the biochemical composition of normal bronchial tissue is a prerequisite for understanding the biochemical changes that accompany histological changes during lung cancer development. In this study, 12 Raman microspectroscopic mapping experiments were performed on frozen sections of normal bronchial tissue. Pseudocolor Raman images were constructed using principal component analysis and K-means cluster analysis. Subsequent comparison of Raman images with histologic evaluation of stained sections enabled the identification of the morphologic origin (e.g., bronchial mucus, epithelium, fibrocollagenous stroma, smooth muscle, glandular tissue and cartilage) of the spectral features. Raman spectra collected from the basal side of epithelium consistently showed higher DNA contributions and lower lipid contributions when compared with superficial epithelium spectra. Spectra of bronchial mucus revealed a strong signal contribution of lipids, predominantly triolein. These spectra were almost identical to the spectra obtained from submucosal glands, which suggests that the bronchial mucus is mainly composed of gland secretions. Different parts of fibrocollagenous tissue were distinguished by differences in spectral contributions from collagen and actin/myosin. Cartilage was identified by spectral contributions of glycosaminoglycans and collagen. As demonstrated here, *in situ* analysis of the molecular composition of histologic structures by Raman microspectroscopic mapping creates powerful opportunities for increasing our fundamental understanding of tissue organization and function. Moreover, it provides a firm basis for further *in vitro* and *in vivo* investigations of the biochemical changes that accompany pathologic transformation of tissue.

## Introduction

The prognosis for patients with lung cancer essentially depends on the stage of the disease at the time of diagnosis. Because of this, there has been a shift in diagnostic and therapeutic standards from a focus on cancer that presents itself clinically, toward pre-malignant lesions [i.e., dysplasia and carcinoma *in situ* (CIS)]. A number of optical techniques are being evaluated as tools for detection of pre-malignant bronchial tissue. Different studies have reported that laser-induced fluorescence endoscopy (LIFE), when used as an adjunct to standard white light bronchoscopy (WLB), resulted in higher overall sensitivity for detecting dysplasia and CIS when compared with WLB alone.<sup>1-5</sup> However, this improvement in sensitivity is associated with a statistically significant decrease in specificity.<sup>5</sup> Hence, there is a need for additional tools that can detect pre-malignant epithelial changes with higher sensitivity and specificity, and therefore could facilitate the treatment of lung cancer. To make it possible to detect biochemical alterations that accompany the development of lung cancer, knowledge about the biochemical composition of different structures in normal lung tissue is essential. Raman spectroscopy provides information about the molecular composition, molecular structures, and molecular interactions in tissue,<sup>6-9</sup> but so far this technique has not been used to study bronchial epithelium.

Raman spectroscopy is a nondestructive optical technique, based on inelastic scattering of light by the molecules in a sample. Since different types of tissue will vary in their overall molecular composition, their Raman spectra will also be different and can, therefore, be used as tissue-specific spectroscopic fingerprints. Pathologic changes in molecular composition or structure are reflected in the spectra enabling development of diagnostic tools based on Raman spectroscopy. Application of Raman spectroscopy as a nondestructive technique for *ex vivo* and *in vivo* tissue characterization (e.g., normal, pre-cancerous, cancerous tissues) has shown significant progress in recent years.<sup>6-16</sup> Miniaturization of flexible fiber-optic probes that are suitable for Raman spectroscopy is opening new pathways towards *in vivo* clinical applications e.g., in cardiology and oncology.<sup>15,16</sup> A complicating factor is heterogeneous structure and chemical composition of tissues. For a thorough understanding of tissue Raman signal, it is necessary to analyze the contribution of different structures in the tissue to the overall Raman signal. *In vitro* Raman microspectroscopic mapping studies of thin tissue sections provides a clear insight into this matter and allows an *in situ* biochemical analysis at micron scale. So far, only one study on lung tissue using Raman spectroscopy has been reported.<sup>14</sup> However, that study, which addressed the feasibility of measuring *in vivo* Raman spectra without fluorescence background using 1064 nm excitation and a newly developed InP/InGaAsP multichannel detector, did not focus on a detailed characterization of the chemical composition of normal lung tissue.

We report on the use of Raman microspectroscopic mapping experiments and hematoxylin and eosin (HE) staining of unfixed thin section of normal human bronchial tissue, to iden-

tify tissue regions with different chemical composition and to relate these regions to tissue morphology. This investigation serves as a starting point for a study of malignant transformation of bronchial epithelium and furthermore, sheds light on the issue of composition and origin of the bronchial mucus.

## Materials and Methods

### Sample Handling

The tissue specimens that were used in this study originated from resection material obtained during surgical procedures at the Department of Cardiothoracic Surgery of the Erasmus MC Rotterdam. After excision, tissue samples were snap frozen by immersion in liquid nitrogen and kept at  $-80^{\circ}\text{C}$  until further use. For sectioning, these frozen samples were mounted on the cryotome-stage using Tissue Tek<sup>®</sup>. Care was taken to only embed the side of the sample needed for mounting in order to avoid contamination of the rest of the specimen by Tissue Tek<sup>®</sup>. Mounted samples were cut into 20- $\mu\text{m}$ -thick sections and placed onto calcium fluoride ( $\text{CaF}_2$ ) microscope slides. The passively dried, unfixed, tissue sections were used without further treatment. To confirm whether tissue was normal and to identify different structures within the bronchial wall, 5- $\mu\text{m}$ -thick adjacent sections were cut before cutting 20- $\mu\text{m}$  sections. Adjacent sections were stained with HE and histopathologically evaluated. Bright-field images of the unstained tissue sections revealed heterogeneity in tissue structure, which could be linked to the structural heterogeneity observed in the stained adjacent sections. This assessment was used to select regions for Raman mapping. To provide a direct comparison of the Raman mapping results with histology, the 20- $\mu\text{m}$  tissue sections were HE stained as well, after Raman mapping measurements were completed. To confirm whether the tissue morphology was consistent over the thickness, comparison with adjacent sections was performed for all 20- $\mu\text{m}$  sections after they have been microscopically scanned and HE stained. In this study, a total of 12 Raman mapping sessions were performed on 10 unstained cryosections of normal bronchial tissue derived from 8 patients.

The Medical Ethics Review Board of the Erasmus MC approved the study and written informed consent was obtained from eight patients.

### Reference Spectra

Reference Raman spectra were obtained of triolein, deoxyribonucleic acid (DNA), collagen type I, actin and tryptophan (Sigma-Aldrich Chemie, Zwijndrecht, The Netherlands). These compounds were used without further purification. DNA (from calf thymus) was dissolved in demineralized water (20 mg/ml). In addition, we also recorded the spectra of the tissue embedding agent used in this study (Tissue Tek<sup>®</sup>).

## Raman Microspectrometer

A near-infrared multichannel Raman microspectrometer, built in-house, was used to collect the Raman spectra of tissue sections. This Raman system was recently described in detail.<sup>17</sup> Briefly, laser light of 847 nm was focused on the sample by an 80x objective, optimized for use in the near-infrared (NIR) spectral region (MIR-plan 80x/0.75, Olympus, Japan). Raman signal was collected in the spectral interval from 400 to 1800  $\text{cm}^{-1}$ , with a spectral resolution of 8  $\text{cm}^{-1}$ .

Automatic scanning of unstained cryosections (20  $\mu\text{m}$ ) of bronchus tissue was enabled by an xyz- motorized, computer-controlled sample stage (Leica DM STC, Cambridge, UK). The laser light was focused below the surface of the tissue at such a depth that the signal intensity was maximized. For each Raman mapping experiment the tissue area and the scanning step size were selected. Thereby the area of interest was divided up into small square areas (hereafter termed Raman pixel). Spectra were obtained consecutively from the tissue in each of these Raman pixels with a resolution that varied between 1  $\mu\text{m}$  and 12  $\mu\text{m}$ , in different experiments. The 80x microscope objective focused the laser light to a spot of less than 1  $\mu\text{m}^2$ . To obtain a spectrum that is representative for the tissue in a Raman pixel, the area of the Raman pixel was scanned during each spectral measurement. Tissue samples were excited with 90 – 110 mW of laser power during Raman experiments. Spectra were obtained using 10 s of signal collection time per Raman pixel.

Acquisition of Raman spectra and microscopic stage movement was controlled by the WiRE 1.2 software (Renishaw) running under Grams/32 Spectral Notebase Software (Galactic Industries Corp., Salem, NH, USA). Raman mapping software was implemented in Array Basic (the internal software platform of Grams) and controlled the Leica microscope unit and the microscope stage.

## Data Analysis

### *Pretreatment of Spectra*

Following data acquisition, the spectra were first calibrated and corrected for the wavelength-dependent signal detection efficiency of the Raman setup, as described earlier.<sup>18</sup> Interfering background Raman signal originating in the optical elements in the laser light delivery pathway and the  $\text{CaF}_2$  slide measured separately was subtracted from the tissue Raman spectra.

### *Raman Maps*

Pseudocolor Raman maps were constructed from the spectral data set using multivariate statistical techniques. The first derivative of the spectra was calculated (using the Savitzky-Golay method with a smoothing window of 9 points) and the resulting spectra were subsequently scaled so that all the derivative spectra of a map had zero mean and unit standard

deviation (auto-scaling or standard normal variate scaling).<sup>18</sup> In this way, the influence of any slowly varying fluorescence or background scatter in the spectra, which is noninformative, was minimized.

To orthogonalize and reduce the number of parameters needed to represent the signal variance in the spectral data set, principal component analysis (PCA)<sup>19</sup> was used. PCA finds the orthogonal directions in spectral space (Principal Components or PCs) that describe the major sources of spectral variance. The first PC reflects the average spectrum: each subsequent PC is orthogonal to the former and describes a continuously decreasing part of the total variance in the dataset. These PCs are then used as new coordinates, and all spectra in the dataset are expressed as scores on these new coordinates (PCA scores). The scores on the first PCs, together accounting for 99.9% of the variance captured, served as input for K-means cluster analysis (KCA).<sup>20</sup> Cluster analysis was performed to find groups of spectra that have resembling spectral characteristics. KCA was used here because it can easily handle the large amounts of data as obtained during Raman mapping experiments.

KCA divides the data set in a predetermined number of clusters by the following procedure (with  $N$  the number of clusters). First  $N$  spectra are chosen at random from the dataset. These spectra are taken as initial cluster centers. Then the distance of all spectra to these cluster centers is calculated, and the spectra are assigned to the nearest cluster (-center). Then for each cluster a new center is calculated, being the average of all spectra, assigned to that cluster. This procedure is repeated until a stable solution is reached. This procedure has recently been used and described in several *in vitro* Raman studies.<sup>11,12</sup>

A Raman spectrum presents the overall molecular composition of the measurement volume in the tissue, because all molecules in the measurement volume contribute to the Raman signal. Spectra that are highly similar, and therefore were obtained of tissue areas of very similar molecular composition, end up in the same clusters. The cluster-membership information was plotted as a pseudocolor map by assigning a color to each cluster. The location of differently colored areas in the pseudocolor Raman maps was compared with the HE-stained tissue section.

Depending on the size of the selected area and mapping resolution, the number of pixels per Raman map varied from 50 to 900 pixels for five Raman maps of small areas within different bronchial structures (mapped with 1- $\mu\text{m}$  resolution) and from 1620 to 12544 pixels in seven experiments where larger tissue regions were mapped (with 4.4- $\mu\text{m}$  to 12- $\mu\text{m}$  resolution), comprising epithelium and submucosa.

### *Raman Difference Spectra*

Information about differences in biochemical composition of the various tissue structures can be obtained from positive difference spectra, which are calculated by scaled subtraction of the cluster averages from each other in such a way that the difference spectrum does not show negative Raman features.

### Spectral Modeling

A routine least-squares fitting procedure was performed to obtain information about the differences in chemical composition between various histologic structures. The Raman spectra of individual histologic features were fitted with the spectra obtained from surrounding tissue plus the reference spectra of one or more compounds (i.e., collagen, actin, triolein and DNA). This (nonrestricted) fitting procedure resulted in positive or negative fit contributions of the reference spectra that point out higher or lower concentrations of the corresponding compounds in tissue structures that were compared. Relative scattering cross-sections were not determined and therefore all fit contributions are presented as arbitrary units and not as weight percentages.

## Results

To provide an impression of the normal bronchial histology, standard paraffin sections (HE-stained) were prepared. Photographs are displayed in Figure 1. Panel A shows the basic structure of the bronchial wall segment that comprises a ciliated columnar epithelium (indicated E) with underlying lamina propria (indicated Lp, pointed with arrow) and subepi-

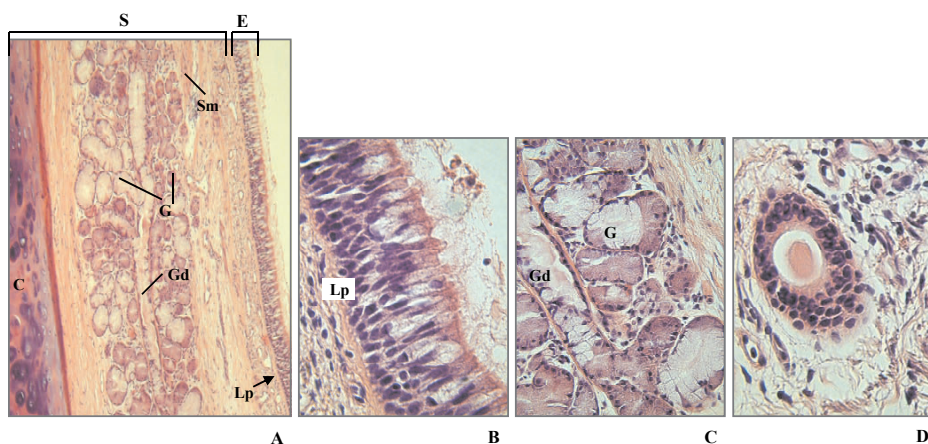


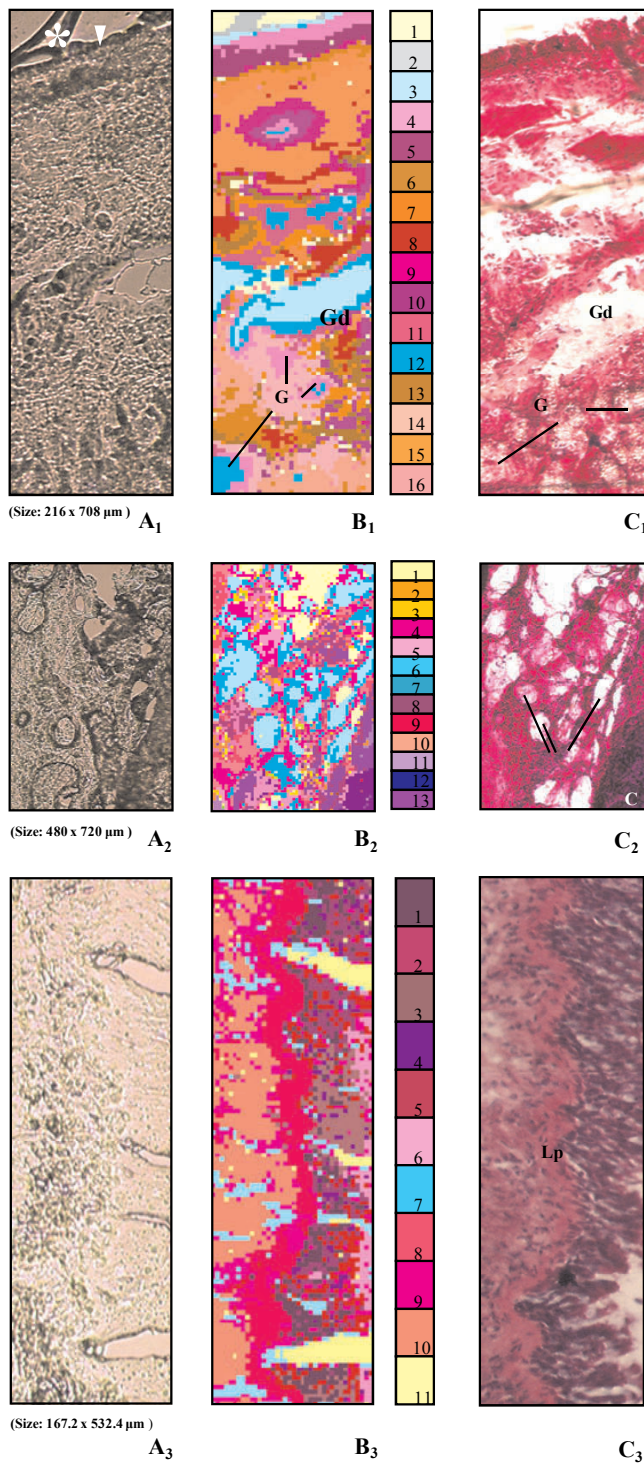
**Figure 1. A:** Micrograph (original magnification, x 10) of a HE-stained section showing a transversally cut bronchial wall segment with the pseudostratified columnar ciliated epithelium (indicated E), underlying lamina propria (indicated Lp, pointed by arrow), and submucosa (indicated S). Note the seromucous glands (indicated G), band of smooth muscle (indicated Sm), a large, longitudinally cut, excretory gland duct (indicated Gd) and a part of cartilage plate (indicated C), in submucosa. **B to D:** Micrographs showing (original magnification, x 60) the histological structure of bronchial wall in more detail. **B:** Within the epithelium it is evident that the most of the nuclei are located at the basal side. Lamina propria (Lp) is also visible. Bronchial mucus is mostly washed away and therefore visible as a discontinuous epithelial coat. **C:** Seromucous glands (G) with the (main) excretory duct (Gd). **D:** Excretory gland duct at a transversal cut with surrounding fibrocollagenous stroma. (Note pink-stained bronchial secretion in the lumen of gland duct.)

thelial tissue termed submucosa (indicated S). The pseudostratified bronchial epithelium (Figure 1 panel B) is made up of several cell types with the nuclei at the different heights within the epithelium. Bronchial epithelium is coated by a liquid layer termed bronchial mucus, which plays an important role in the defense of the respiratory tract from inhaled airborne particles that are trapped in this epithelial lining and constantly cleared by the action of ciliary epithelial cells. Due to the staining procedure bronchial mucus is mostly washed away and therefore visible as a discontinuous epithelial coat in panels A and B (Figure 1). The submucosa contains variable amounts of smooth muscle (indicated Sm), a partial cartilaginous ring (indicated C) and fibrocollagenous stroma with variable quantities of glands (indicated G) and gland ducts (indicated Gd). The bronchial glands are of the seromucous type and have a branched architecture with secretory cells arranged in islands termed acini. These glands are located superficially and deeply in the submucosa between and beneath cartilaginous plates. They empty into the bronchial lumen through short or long ducts depending on their location in the bronchial wall. Glands and gland ducts are shown in more detail in panel C and a transversally cut gland duct is shown in the medium-power micrograph in panel D.

**Figure 2, following page.** *Raman microspectroscopic mapping experiments.* **A1:** Microphotograph of an unstained section of bronchial wall. Note the presence of a hair-like structure (asterisk; Tissue Tek artefact) and the liquid layer lining the epithelium (triangle). **B1:** A gross overview Raman map based on KCA using 16 clusters. Spectra (4248) were obtained at a resolution of 6  $\mu\text{m}$  and each spectrum is represented by one pixel. Cluster 1 consists of the spectra obtained at the edge of the tissue section where no tissue was present. A hair-like structure and bronchial mucus (i.e., the liquid layer lining the epithelium) are represented by clusters 2 and 3, respectively. Clusters 4 and 5 correspond with the pseudostratified bronchial epithelium. The superficial part of epithelium, consisting of cytoplasmic components, is represented by cluster 4, cluster 5 represents the basal part that is nuclei rich. Clusters 7 and 15 coincide with submucosal fibrocollagenous stroma tissue and cluster 8 coincides with a band of smooth muscle (due to loss of tissue during staining procedure not well preserved in HE section). Cluster 9 represents the fibrocollagenous tissue surrounding a transversally cut gland duct. Furthermore, there is a good correspondence of glandular tissue (i.e., seromucous glands and their ducts) with clusters 4, 10, 12, 14 and 16. Note that cluster 3 indicates both the bronchial mucus lining the epithelium and the secretions within the lumen of gland ducts. **C1:** HE stain of the same tissue section showing a segment of the bronchial wall with epithelium and underlying submucosal tissue. Due to the staining procedure bronchial mucus and gland secretions were washed away.

**A2:** Unstained bronchial tissue section containing numerous glands and a partial cartilage. **B2:** A pseudocolor map (480 spectra, 8  $\mu\text{m}$ -resolution) based on KCA using 13 clusters. The secretory glands (main clusters 6 and 7), fibrocollagenous stroma (clusters 4, 5, 9 and 10) and the cartilage tissue (clusters 12 and 13) are clearly distinguishable and can be easily re-located in the HE-stained section. **C2:** HE staining of the same tissue section showing secretory glands (indicated with lines) and slightly blue stained cartilage (C). The gland secretions were washed out after HE procedure, as shown in Figure 1C.

**A3:** Unstained section of an area consisted of a part of the bronchial epithelium and a part of the submucosa. **B3:** Raman spectra (4598), obtained at a 4.4- $\mu\text{m}$  resolution, were analyzed by KCA using 11 clusters resulting in a pseudocolor map. At this higher resolution, basal epithelial side is captured by several clusters (clusters 1-5) indicating small areas with higher/lower nuclear contents. Cluster 6 coincides with the luminal epithelial side. **C3:** HE-stained section with the clearly visible lamina propria (Lp) that separates bronchial epithelium from underlying submucosal tissue.



## Pseudocolor Raman Maps

The results of three Raman mapping experiments, which are representative of the 12 mapping experiments that were carried out, are shown in Figure 2. After scanning of the unstained tissue sections (Figures 2A<sub>1</sub>, 2A<sub>2</sub>, and 2A<sub>3</sub>), the acquired Raman spectra were analyzed by principal component analysis (PCA) followed by K-means cluster analysis (KCA). This procedure groups similar spectra in one cluster. Each cluster was assigned a color resulting in a pseudocolor Raman map (Figures 2B<sub>1</sub>, 2B<sub>2</sub>, and 2B<sub>3</sub>). The HE staining caused some loss and displacement of tissue, but the overall morphologic aspect of the bronchial wall was preserved (Figures 2C<sub>1</sub>, 2C<sub>2</sub>, and 2C<sub>3</sub>). Comparison of these HE-stained sections with corresponding adjacent sections revealed that in all sections measured, the tissue morphology was consistent over the thickness of 20  $\mu\text{m}$ . This implies that the morphological origin of the spectra that were recorded was well defined. In Figure 2B<sub>1</sub> a Raman map with a pixel size of 6  $\mu\text{m}$  x 6  $\mu\text{m}$  is displayed. A comparison of this pseudocolor map with the images of the unstained (Figure 2A<sub>1</sub>) and the HE-stained (Figure 2C<sub>1</sub>) tissue section shows that different colors in the Raman map correspond with distinct histologic features in the bronchial epithelium and submucosal tissue. The hair-like structure (asterisk) and the bronchial mucus lining the epithelium (triangle) that are visible in the unstained section clearly coincide with clusters 2 and 3 of the Raman map. Such hair-like structures were frequently observed in the unstained sections but were washed away together with the bronchial mucus during the standard HE staining procedure and proved to be artifacts. The Raman spectra of this structure (not shown) contain signal contributions of both the medium in which the tissue was embedded before sectioning (Tissue Tek®, spectrum shown in Figure 6E) and of the bronchial mucus. The bronchial epithelium is divided up into two clusters in the pseudocolor Raman map. Cluster 4 coincides with the superficial part, cluster 5 with the basal part of epithelium. This division reflects the fact that the nuclei are predominantly located on the basal side of the epithelium. Therefore cluster 5 will be referred to as “nuclear epithelial cluster” and cluster 4 will be referred to as “cytoplasmic epithelial cluster”. The fibrocollagenous stroma tissue (clusters 7 and 15) and smooth muscle (cluster 8) are clearly distinguished from glands and their excretory ducts (clusters 4, 10, 12, 14, 16). It is evident that the luminal content (i.e., gland secretions) of large gland ducts (indicated Gd in Figure 2B<sub>1</sub>) coincides with cluster 3 associated with the bronchial mucus at the epithelial surface. Due to the staining procedure that washes away the secretory contents from glands and their ducts, these structures appear empty in the HE-stained section as shown in Figure 2C<sub>1</sub>. Figures 2A<sub>2</sub>, 2B<sub>2</sub>, and 2C<sub>2</sub> show a region with numerous glands and cartilage, (Figure 2A<sub>2</sub>) scanned with 8- $\mu\text{m}$  resolution. Again the gland secretions were washed out after routine staining. The Raman map (Figure 2B<sub>2</sub>) and HE section (Figure 2C<sub>2</sub>) correspond well. Clusters 6 and 7 in the Raman map represent the inner parts of most glands. Cartilage tissue (indicated C in Figure 2C<sub>2</sub>) is captured by clusters 12 and 13 in the Raman map.

A more detailed Raman map of bronchial epithelium (Figure 2B<sub>3</sub>) was obtained at a resolution of 4.4  $\mu\text{m}$ . As is evident from the HE-stained section (Figure 2C<sub>3</sub>), epithelium is separated from submucosa by a clearly visible lamina propria indicated by cluster 8. Also in this Raman map, there is a clear division between the luminal side of the epithelial cells (cluster 6) and the basal side of the epithelial cells, which at this higher resolution is captured in several clusters (clusters 1 to 5).

## Spectral Analysis

### Bronchial Mucus

The average spectrum obtained from bronchial mucus at the epithelial surface is displayed in Figure 3A (cluster 3 in Figure 2B<sub>1</sub>). Comparison with a spectrum of pure triolein (Figure 3 spectrum B) reveals a strong overlap. The difference of the spectra of bronchial mucus and triolein (Figure 3 spectrum C) reveals peaks at  $\sim 1159$  and  $\sim 1525$   $\text{cm}^{-1}$ , which suggests the presence of carotenoids in bronchial mucus.<sup>21</sup> These carotenoid signal contributions were

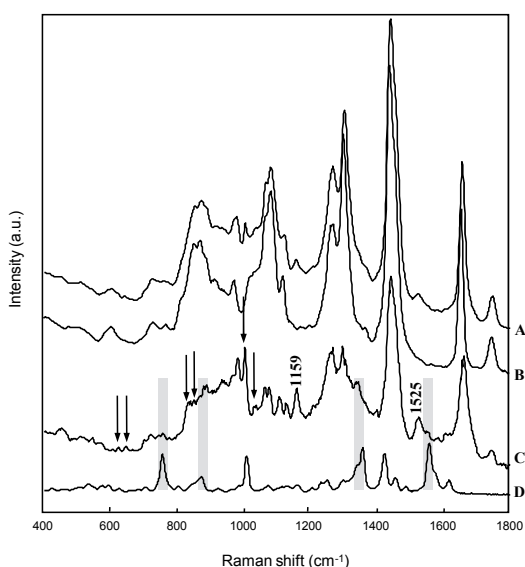


**Figure 3.** Raman spectrum of bronchial mucus. **A:** Cluster-average spectrum obtained from bronchial mucus (BM) at the epithelial surface from the unstained tissue section as shown in Figure 2A<sub>1</sub> (cluster 3 in Figure 2B<sub>1</sub>). **B:** Raman spectrum of pure triolein shows a striking correspondence with BM spectrum. **C:** Difference spectrum “BM minus triolein”. The Raman peaks at  $\sim 1159$  and  $\sim 1525$   $\text{cm}^{-1}$  suggest the presence of carotenoids. Spectral contribution from proteins is suggested by peaks assigned to phenylalanine (at 623, 1002 and 1031  $\text{cm}^{-1}$ ) and tyrosine (at 643, 833 and 849  $\text{cm}^{-1}$ ), indicated by arrows. Comparison with the Raman spectrum of pure tryptophan (**D**) reveals that, although the presence of tryptophan signal contributions cannot be completely excluded (gray bars), there is no clear evidence of the lysozyme presence in the difference spectrum.

found in tissue samples from four patients. The phenylalanine peaks at 623, 1002 and 1031  $\text{cm}^{-1}$  and tyrosine peaks at 643, 833 and 849  $\text{cm}^{-1}$  were observed in the tissue specimens of all patients. This suggests that there is a slight contribution of proteins in the spectra of bronchial mucus. Lysozyme is an important anti-bacterial constituent of bronchial secretions.<sup>22-24</sup> The Raman spectrum of lysozyme is characterized by strong signal contributions of tryptophan (Figure 3 spectrum D).<sup>25</sup> For comparison we have obtained the Raman spectrum of pure tryptophan. This shows that, although the presence of tryptophan signal contributions cannot be completely excluded (Figure 3, gray bars), the difference spectrum does not provide clear evidence of the presence of lysozyme.

### *Epithelium*

As illustrated by Figures 1 and 2, the pseudostratified bronchial epithelium consists of a single layer of cells with most of the nuclei located on the basal epithelial side. The averaged spectra of the “nuclear epithelial cluster” (cluster 1 in Figure 2B<sub>3</sub>) and the “cytoplasmic epithelial cluster” (cluster 6 in Figure 2B<sub>3</sub>) are shown in Figure 4 (spectra A and B, respectively). To investigate the underlying differences in molecular composition, a difference spectrum (spectrum C) between these two cluster averages was calculated (“nuclear epithelial cluster” minus “cytoplasmic epithelial cluster”). The difference spectrum reveals prominent Raman peaks at 501, 727, 784, 1096 and 1576  $\text{cm}^{-1}$ , which can be assigned to DNA (spectrum D, gray bars). As expected, the “nuclear epithelial cluster” contains a higher DNA concentration than the “cytoplasmic epithelial cluster”. In the same way, the “nuclear epithelial cluster” was subtracted from the “cytoplasmic epithelial cluster” resulting in the difference spectrum shown in Figure 4 spectrum E. The strong bands at 1262 and 1305  $\text{cm}^{-1}$  are most likely due to fatty acid signal contributions and therefore are probably indicative of a higher concentration of lipids in the cytoplasmic epithelial cluster. A higher protein concentration in this cluster can be deduced from the presence of proteins small peaks assigned to phenylalanine (621, 1004 and 1033  $\text{cm}^{-1}$ ) and tyrosine (644, 831 and 852  $\text{cm}^{-1}$ ). Furthermore, the Raman bands in the 1546-1583  $\text{cm}^{-1}$  region are indicative of the presence of heme-proteins<sup>15</sup> such as catalase.<sup>24</sup>

### *Submucosa*

Various spectral clusters were found in the submucosa, including those that represent groups of secreting glands and their ducts (Figure 2B<sub>1</sub>, main clusters 10, 4, 12), fibrocollagenous stroma with smooth muscle bands (Figure 2B<sub>1</sub>, clusters 7 and 8 respectively) and cartilage (Figure 2B<sub>2</sub>, clusters 12 and 13).

*Fibrocollagenous Stroma.* The differences in chemical composition of the main fibrocollagenous stroma cluster (cluster 7 of Figure 2B<sub>1</sub>) and smooth muscle bands (cluster 8 of Figure 2B<sub>1</sub>) were analyzed by means of a least-squares fit procedure (Figure 5). Fibrocollagenous stroma

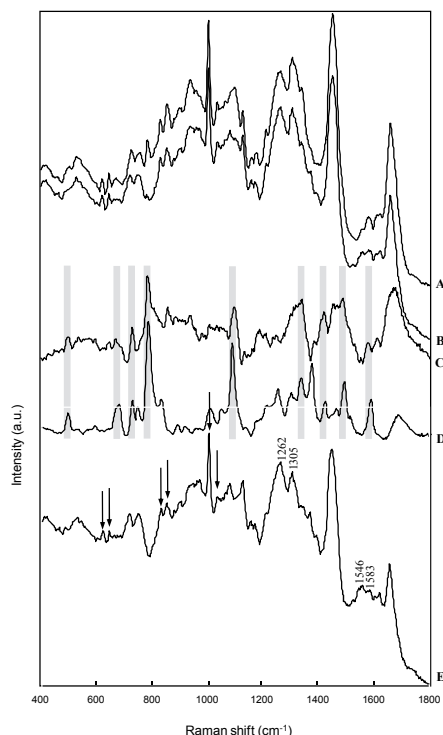


**Figure 4.** Raman spectra obtained from the bronchial epithelium. **A:** Average spectrum of “nuclear epithelial cluster” (cluster 1 in Figure 2B<sub>3</sub>) and **B:** Average spectrum of “cytoplasmic epithelial cluster” (cluster 6 in Figure 2B<sub>3</sub>). **C:** The difference spectrum between these two spectra (“nuclear epithelial cluster” minus “cytoplasmic epithelial cluster”) shows many spectral features (gray bars) of DNA. **D:** Raman spectrum of pure DNA. **E:** The difference spectrum “cytoplasmic epithelial cluster” minus “nuclear epithelial cluster”. The presence of protein signal contributions is suggested by spectral features of phenylalanine (621, 1004 and 1033  $\text{cm}^{-1}$ ) and tyrosine (644, 831 and 852  $\text{cm}^{-1}$ ), indicated by arrows. The prominent bands at 1262 and 1305  $\text{cm}^{-1}$  imply the significant signal contributions of lipids in the “cytoplasmic epithelial cluster”. Furthermore, the Raman bands in the 1546 - 1583  $\text{cm}^{-1}$  region are indicative of heme-proteins such as catalase.

contains a high concentration of collagen and smooth muscle contains a high concentration of actin and myosin.<sup>23,24</sup> Actin and myosin have similar Raman spectra.<sup>26</sup> The average spectrum of cluster 7 was fitted with the average spectrum of cluster 8 and the spectra of pure collagen and actin, which are shown as the fit-spectra (spectra B, C, and D) after multiplication by the fit-coefficients that resulted from the least-squares fit. Fit-residual is shown in Figure 5 spectrum E. Therefore a positive/negative spectrum signifies that more/less of that compound is present in cluster 7 than in cluster 8. It follows that in fibrocollagenous stroma the concentration of collagen was higher and the concentration of actin was lower than in smooth muscle. For clarity, the spectra of pure collagen (Figure 5 spectrum F) and pure actin (Figure 5 spectrum G) are also shown.

*Glands and Gland Ducts.* Figure 6 displays a comparison of a cluster-averaged Raman spectrum obtained from the tissue layer lining the lumen of the glands and their ducts (spectrum A, cluster 12 in Figure 2B<sub>1</sub>) with spectrum of bronchial mucus at the epithelial surface and from gland duct (spectrum B, cluster 3 in Figure 2B<sub>1</sub>). A high spectral resemblance is evident. Raman spectra collected from the periphery of gland duct (spectra C and D, clusters 4 and 10 in Figure 2B<sub>1</sub>) are also shown. It is notable that there is a decrease in lipid signal contribution from the luminal side of the gland duct towards its periphery. Prominent Raman bands of lipids (gray bars) are present at 1301, 1440, 1656, and 1746  $\text{cm}^{-1}$ . Furthermore, we have analyzed whether there was Tissue Tek<sup>®</sup> contamination of the spectra we have obtained. As displayed in Figure 6E (open bars) Raman spectrum of Tissue Tek<sup>®</sup> shows specific bands at 633, 916, 1364, and 1734  $\text{cm}^{-1}$ , which do not contribute to the spectra recorded from bronchial

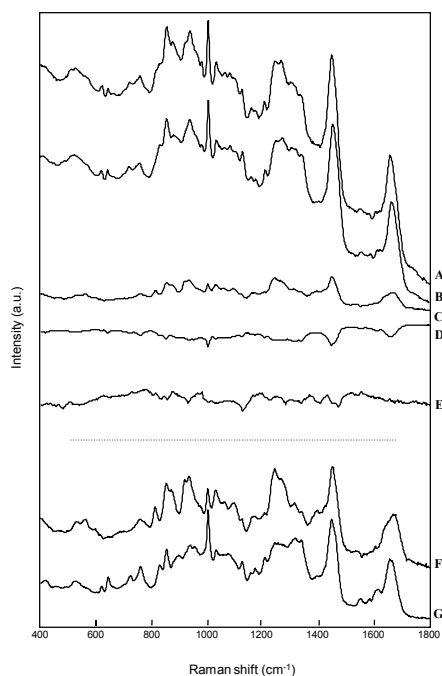


**Figure 5.** The differences in chemical composition between fibrocollagenous stroma and smooth muscle analyzed by means of a least-squares fit procedure. The average spectrum of fibrocollagenous stroma (spectrum A, cluster 7 in Figure 2B<sub>1</sub>) was fitted with the average spectrum of smooth muscle (cluster 8 in Figure 2B<sub>1</sub>) and the spectra of pure collagen and pure actin. The fit-spectra (spectra B, C and D) are the average spectra of smooth muscle and of collagen and actin respectively, which are shown after multiplication by the fit-coefficients that resulted from the least-squares fit. The fit-residual (spectrum E) suggests a higher collagen contribution and lower actin contribution in fibrocollagenous spectrum than in smooth muscle spectrum.

For comparison with the fit-spectra the Raman spectra of pure collagen (spectrum F) and of pure actin (spectrum G) are also shown. For clarity of presentation collagen spectrum was divided by factor 8 and actin spectrum by factor 10.

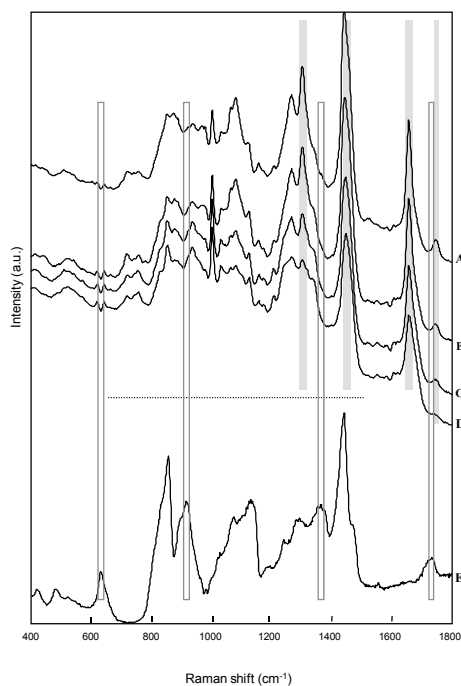


**Figure 6.** Raman spectra obtained from bronchial mucus and from bronchial gland secretions. **A:** Average spectrum obtained from bronchial mucus at the epithelial surface (cluster 3 in Figure 2B<sub>1</sub>). **B to D:** The cluster averages from the excretory gland duct, collected from the luminal surface towards the periphery of duct (clusters 3, 4 and 10 respectively, in Figure 2B<sub>1</sub>). There is a very high resemblance between spectra of bronchial mucus and spectra obtained from the tissue layer at the luminal side of gland duct. Prominent Raman bands of lipids at 1301, 1440, 1656, and 1746 cm<sup>-1</sup> (gray bars) show a decrease in signal from the luminal side of duct towards its periphery.

For comparison, spectrum obtained of pure Tissue Tek® is shown (spectrum **E**). Open bars highlight the absence of Tissue Tek® specific bands (at about 633, 916, 1364, and 1734 cm<sup>-1</sup>) in the spectra shown in A to D.

mucus or from gland tissue. The tissue area captured in cluster 9 (Figure 2B<sub>1</sub>) demarcates a transition area between fibrocollagenous tissue and gland duct tissue. The spectrum of the transition area (Figure 7 spectrum A) can be almost completely reconstructed from the spectrum of the fibrocollagenous stroma (cluster 7 of Figure 2B<sub>1</sub>) and the spectrum of the bronchial mucus on the epithelial surface (cluster 3 of Figure 2B<sub>1</sub>), as is evident from the very small fit-residual (Figure 7 spectrum D). It suggests that some of the bronchial gland secretion diffuses into the fibrocollagenous tissue surrounding the ducts. The fit-spectra (e.g., averaged spectra from fibrocollagenous stroma and from bronchial mucus) are shown after multiplication by the fit-coefficients (Figure 7 spectra B and C).

**Cartilage.** The Raman signal obtained from the cartilage (unstained tissue section; Figure 2A<sub>2</sub>) is shown in Figure 8 (spectrum A). Significant Raman bands, which are mainly due to collagen (spectrum B), are highlighted (gray bars). Furthermore, Raman peaks at 413, 974,

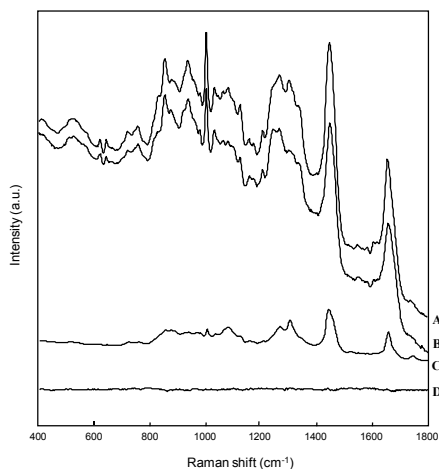


**Figure 7.** Average spectrum of the tissue area (cluster 9 in Figure 2B<sub>1</sub>) between fibrocollagenous stroma and gland duct (spectrum **A**) was fitted with the average spectrum of fibrocollagenous stroma (cluster 7 of Figure 2B<sub>1</sub>) and the spectrum of bronchial mucus (cluster 3 of Figure 2B<sub>1</sub>). The fit-spectra **B** and **C** are the average spectra of fibrocollagenous stroma and of bronchial mucus respectively, which are shown after multiplication by the fit-coefficients. The fit-residual (spectrum **D**) implies that some of the secretion from the gland duct diffuses into the surrounding fibrocollagenous stroma

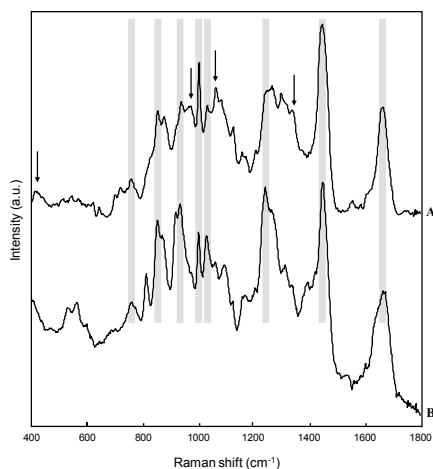


**Figure 8.** Raman spectrum obtained from the bronchial wall cartilage. Comparison of Raman average spectrum of cartilage (spectrum **A**) with the spectrum of pure collagen (spectrum **B**). Spectral regions of the most prominent resemblance are highlighted by gray bars. For clarity of presentation, collagen spectrum was divided by factor 6. Furthermore, the Raman bands visible at 413, 974, 1062, and 1337  $\text{cm}^{-1}$  (arrows) can be assigned to sulfated glycosaminoglycans (GAGs) such as chondroitin sulfate.

1062, and 1337  $\text{cm}^{-1}$  (arrows) suggest the presence of chondroitin sulfate,<sup>27</sup> which belongs to the group of sulfated glycosaminoglycans (GAGs). (Note the strong band at 1062  $\text{cm}^{-1}$ , which can be identified as the symmetric stretching vibration of the  $\text{OSO}_3^-$  group.<sup>27</sup>)

## Discussion

To date, only a few studies have addressed the lipid composition of bronchial mucus. Neutral lipids were the predominant lipids in normal airway secretions studied by Bhaskar *et al.*<sup>28</sup> In other studies, phospholipids represented the main content of bronchial mucus and cholesterol was the principal neutral lipid.<sup>29</sup> Slomiany *et al.* reported that bronchial secretions consisted of similar quantities of neutral lipids and glycolipids.<sup>30</sup> Here we demonstrate that detailed analysis of Raman spectra (see Figure 3) obtained from bronchial mucus reveals triolein as the major component of bronchial mucus. This is in line with studies describing neutral lipids as the primary compound of bronchial mucus. Furthermore, the Raman bands in the 1546 to 1583  $\text{cm}^{-1}$  region (Figure 4 spectrum E) are indicative of the presence of heme-proteins such as enzyme catalase in the cytoplasm of bronchial epithelial cells. This finding could be explained by secretion of anti-oxidants such as catalase by bronchial epithelium, to provide protection against potentially injurious agents.<sup>24</sup> In comparison with the “nuclear epithelial cluster” higher lipid and protein signal contributions and lower DNA signal contributions (Figure 4) were observed in the “cytoplasmic epithelial cluster”. As expected, collagen and actin/myosin were the major discriminators between fibrocollagenous stroma tissue and smooth muscle, although spectral features remain in the fit-residual (Figure 5 spectrum E). This is most probably due to the fact that aside from differences in collagen and actin concentration, these histological structures contain the different amounts of a number of other compounds such as glycosaminoglycans, supportive cells (e.g., fibroblasts and fibrocytes in fibrocollagenous stroma, myofibroblasts in smooth muscle), elastic fibers, and fat. Characteristic Raman spectra of cartilage, which is mainly composed of glycosaminoglycans (GAGs) that are associated with collagen fibers,<sup>27</sup> were also obtained.

Contradictory reports on the origin of lipids in the bronchial mucus have been published. In our study, a very high resemblance between the cluster-averaged Raman spectra obtained from the bronchial mucus at the epithelial surface and the luminal content of the glands and their ducts was found (Figure 7). This implies that bronchial mucus is probably primarily produced by submucosal glands and transported to the epithelial surface via gland ducts. This is in line with reports claiming that the tracheobronchial mucus is mainly secreted by the airway secretory cells, although it may also contain some components from alveolar sources.<sup>28,31,32</sup> Some authors suggest the existence of “conductive airway surfactant” that has different biochemical and surface-tension properties compared to alveolar surfactant.<sup>32,33</sup>

We have studied tissue samples that were snap frozen directly after collection and performed the Raman analysis without any preceding processing (e.g., dices, labels). Although some artifacts were recognized (see Figure 2A<sub>1</sub> and 2B<sub>1</sub>) that were due to the use of Tissue Tek® as an embedding agent (see Materials and Methods), spectral analysis revealed that there was no spectral contamination, neither of the bronchial mucus nor of the tissue. This

was very easy to confirm, since Tissue Tek<sup>®</sup> specific bands were not present in the spectra we collected (Figure 6 E, open bars). Other approaches to study the composition of bronchial lining secretion, like those on material obtained after laryngectomy or tracheotomy, tracheal aspirates, bronchopulmonary washings, sputum, surgically removed bronchogenic cysts and secreting cells cultures are hampered by potential contamination of the sample by alveolar components or sputum.<sup>32,34</sup> In addition, sometimes only a fraction of the bronchial secretions was investigated (e.g., soluble phase only or fibrillar network only). It is clear that the uncertainty whether the sample that is being analyzed is actually representative of bronchial mucus is taken away by *in situ* analysis on unfixed tissues.

## Concluding Remarks

In this study, we analyze the Raman spectra obtained from snap frozen human bronchial tissue sections. Raman mapping experiments were performed and directly compared with the histology of the tissue sections. By precise linking of spectral features with the histologic structures, information about the (differences in) molecular composition of these structures was revealed. Hence, Raman spectroscopy may become an important tool in increasing our fundamental understanding of biological structures and their aberrations. A clear illustration of the power of such an approach is the straightforward way in which the main composition and source of the bronchial mucus could be analyzed. In various studies it was suggested that in diseases such as chronic bronchitis, asthma and cystic fibrosis, the bronchial hypersecretion is accompanied by changes in biochemical composition of bronchial mucus.<sup>22,29,31</sup> Likewise, the presence of (pre-) malignant tissue may affect the formation and/or composition of the bronchial mucus. These are topics of continued research efforts in this area. In future *in vivo* measurements, most likely by means of fiber-optics, the tissue volumes from which signal will be obtained will be much larger than in this study. This implies that several different tissue layers and structures will contribute to the Raman signal that will be obtained. The detailed information obtained in this study will be valuable for the interpretation of such spectra. With similar studies to be performed for pathologic conditions of bronchial tissue, such as malignancies and pre-malignant tissues, the development of *in vivo* diagnostic applications can be put on a solid basis.

## References

1. Lam S., T. Kennedy, M. Unger, Y. E. Miller, D. Gelmont, V. Rusch, B. Gipe, D. Howard, J. C. LeRiche, A. Coldman, and A. F. Gazdar, "Localization of bronchial intraepithelial neoplastic lesions by fluorescence bronchoscopy," *Chest* 113, 696-702 (1998).
2. Venmans B. J., J. C. van der Linden, A. J. van Boxem, P. E. Postmus, E. F. Smit, and G. Sutedja, "Early detection of pre-invasive lesions in high risk patients. A comparison of conventional fiberoptic and fluorescence bronchoscopy," *J. Bronchol.* 5, 280-283 (1998).
3. Kusunoki Y., F. Imamura, H. Uda, M. Mano, and T. Horai, "Early detection of lung cancer with laser-induced fluorescence endoscopy and spectrofluorometry," *Chest* 118, 1776-1782 (2000).
4. Hirsch F. R., W. A. Franklin, and P. A. Bunn, "Early detection of lung cancer: clinical perspectives of recent advances in biology and radiology," *Clin. Cancer Res.* 7, 5-22 (2001).
5. Hirsch F. R., S. A. Prindiville, Y. E. Miller, W. A. Franklin, E. C. Dempsey, J. R. Murphy, P. A. Bunn Jr., and T. C. Kennedy, "Fluorescence versus white-light bronchoscopy for detection of preneoplastic lesions: a randomized study," *J. Nat. Cancer Inst.* 93, 1385-1391 (2001).
6. Tu A. T., *Basic concept and elementary theory: Raman spectroscopy in biology*, New York: John Wiley & Sons (1982).
7. Puppels G. J., F. F. De Mull, C. Otto, J. Greve, D. J. Arndt-Jovin, and T. M. Jovin, "Studying single living cells and chromosomes by confocal Raman microspectroscopy," *Nature (London)* 347, 301-303 (1990).
8. Mahadevan-Jansen A., M. F. Mitchell, N. Ramanujam, A. Malpica, S. Thomasen, U. Utzinger, and R. Richards-Kortum, "Near-infrared Raman spectroscopy for in vitro detection of cervical precancers," *Photochem. Photobiol.* 68, 123-132 (1998).
9. Hanlon E. B., R. Manorahan, T. W. Koo, K. E. Shafer, J. T. Motz, M. Fitzmaurice, L. R. Kramer, I. Itzakan, R. R. Dasari, and M. S. Feld, "Prospects for in vivo Raman spectroscopy," *Phys. Med. Biol.* 45, R1-R59 (2000).
10. Bakker Schut T. C., M. Witjes, M. Sterenborg, O. Speelman, J. Roodenburg, E. Marple, H. A. Bruining, and G. J. Puppels, "In vivo detection of dysplastic tissue by Raman spectroscopy," *Anal. Chem.* 72, 6010-6018 (2002).
11. Nijssen A., T. C. Bakker Schut, F. Heule, P. J. Caspers, D. P. Hayes, M. H. A. Neumann, and G. J. Puppels, "Discriminating basal cell carcinoma from its surrounding tissue by Raman spectroscopy," *J. Invest. Dermatol.* 119, 64-69 (2002).
12. Koljenović S., L-P. Choo-Smith, T. C. Bakker Schut, J. M. Kros, H. J. van den Berge, and G. J. Puppels, "Discriminating vital tumor from necrotic tissue in human glioblastoma tissue samples by Raman spectroscopy," *Lab. Invest.* 82, 1265-1277 (2002).
13. Boustany N. N., J. M. Crawford, R. Manoharan, R. R. Dasari, and M. S. Feld, "Analysis of nucleotides and aromatic amino acids in normal and neoplastic colon mucosa by ultraviolet resonance Raman spectroscopy," *Lab Invest.* 79, 1201-1214 (1999).
14. Kaminaka S., T. Ito, H. Yamazaki, E. Kohda, and H. Hamaguchi, "Near-infrared multichannel Raman spectroscopy toward real-time in vivo cancer diagnosis," *J. Raman Spectrosc.* 33, 498-502 (2002).
15. Buschman R., E. T. Marple, M. L. Wach, B. Bennett, T. C. Bakker Schut, H. A. Bruining, A. V. Bruschke, A. van der Laarse, and G. P. Puppels, "In vivo determination of the molecular composition of artery wall by intravascular Raman spectroscopy," *Anal. Chem.* 72: 3771-3775 (2000).

16. Utzinger U., D. L. Heintzelman, A. Mahadevan-Jansen, A. Malpica, M. Follen, and R. Richards-Kortum, "Near-infrared Raman spectroscopy for detection of cervical precancers", *Applied Spectroscopy* 55, 955-959 (2001).
17. van de Poll S. W. E., T. J. Romer, O. L. Volger, D. J. M. Delsing, T. C. Bakker Schut, H. M. G. Princen, J. W. Jukema, L. Havekes, A. van der Laarse, and G. J. Puppels, "Raman spectroscopic evaluation of the effects of diet and lipid-lowering therapy on atherosclerotic plaque development in mice", *Arterioscler. Thromb. Vasc. Biol.* 21, 1630-1635 (2001).
18. Wolthuis R., T. C. Bakker Schut, P. J. Caspers, H. P. Buschman, T. J. Römer, H. A. Bruining, and G. J. Puppels, "Raman spectroscopic methods for in vitro and in vivo tissue characterization", Chap. 32 in *Fluorescent and luminescent probes for biological activity*, Mason W.T., Editor, pp. 433-455, Academic Press, San Diego (1999).
19. Jolliffe I. T., *Principal component analysis*, Springer-Verlag, New York (1986).
20. Jain A. K. and R. C. Dubes, "Algorithms for clustering data", Prentice Hall: Engelwood Cliffs (1988).
21. Puppels G. J., H. S. P. Garritsen, J. A. Kummer, and J. Greve, "Carotenoids located in human lymphocyte subpopulations and natural killer cells by Raman microspectroscopy", *Cytometry* 14, 251-256 (1993).
22. Widdicombe J. H. and J. G. Widdicombe, "Regulation of human airway surface liquid", *Respiration Physiology* 99, 3-12 (1995).
23. Stevens A. and J. Lowe, *Human histology*, Times Mirror International Publishers Limited, London, 1997.
24. van der Velden V. H. J., H. F. J. Savelkoul, and M. A. Versnel, "Bronchial epithelium: morphology, function, and pathophysiology in asthma", *European Cytokine Network* 9, 585-598, (1998).
25. Blanch E. W., L. A. Morozova-Roche, L. Hecht, W. Noppe, and L. D. Barron, "Raman optical activity characterisation of native and molten globule states of equine lysozyme: Comparison with hen lysozyme and bovine  $\alpha$ -lactalbumin", *Biopolymers (Biospectroscopy)* 57, 235-248 (2000).
26. Carew E. B., H. E. Stanley, J. C. Seidel, and J. Gergely, "Studies of myosin and its' proteolytic fragments by laser Raman spectroscopy", *Biophys. J.* 44, 219-224 (1983).
27. Bansil R., I. V. Yannas, and H. E. Stanley, "Raman spectroscopy: a structural probe of glycosaminoglycans", *Biochimica et Biophysica Acta* 541, 535-542 (1978).
28. Bhaskar K. R., D. D. O'Sullivan, J. Seltzer, T. H. Rossing, J. M. Drazen, and L. M. Reid, "Density gradient study of bronchial mucus aspirates from healthy volunteers (smokers and non-smokers) and from patients with tracheostomy", *Exp. Lung Res.* 9, 289-308 (1985).
29. Kim K. C., H. Opaskar-Hincman, and K. R. Bhaskar, "Secretions from primary hamster tracheal surface epithelial cells in culture: mucine-like glycoproteins, proteoglycans, and lipids", *Exp. Lung Res.* 15, 299-314 (1989).
30. Slomiany A., V. L. N. Murty, M. Aono, C. E. Snyder, A. Herp, and B. L. Slomiany, "Lipid composition of tracheobronchial secretions from normal individuals and patients with cystic fibrosis", *Biochim. Biophys. Act.* 710, 106-111 (1982).
31. Reid L. M. and K. R. Bhaskar, "Macromolecular and lipid constituents of bronchial epithelial mucus", *Symp. Soc. Exp. Biol.* 43, 201-219 (1986).
32. Widdicombe J. G., "Role of lipids in airway function", *Eur. J. Respir. Dis.* 71, 197-204 (1987).
33. Girod S., C. Fuchey, C. Galabert, S. Lebonvallet, N. Bonnet, D. Ploton, and E. Puchelle, "Identification of phospholipids in secretory granules of human submucosal gland respiratory cells", *J. Histochem. Cytochem.* 39, 193-198 (1991).
34. Roussel P., P. Degand, G. Lamblin, A. Laine, and J. J. Lafitte, "Biochemical definition of human tracheobronchial mucus", *Lung* 154, 241-260 (1978).

# Detection of Meningioma in Dura Mater by Raman Spectroscopy

*Analytical Chemistry*  
2005, 77 (24): 7958-7965



S. Koljenović  
T.C. Bakker Schut  
A. Vincent  
J.M. Kros  
G.J. Puppels

## Abstract

Radical tumor resection is the treatment of choice for patients suffering from meningioma. However, recurrence of these tumors is a problem. Tumor recurrences are attributed to residual nests of meningioma within the regional dura. Therefore complete removal of all tumor-infiltrated dura is important. Meningioma and normal dura were studied by Raman microspectroscopy to assess the possibility of developing an *in vivo* Raman method for guidance of meningioma resections. Pseudocolor Raman maps were constructed of cryosections of dura and meningioma, obtained from 20 patients. Comparison of these maps with histopathology enabled assignment of the spectra to either meningioma or dura. Large differences exist between the Raman spectra of dura and meningioma, because of the high collagen content of dura and the increased lipid content of tumors. A classification model for dura and tumor tissue based on linear discriminant analysis of Raman spectra yielded an accuracy of 100%. A first attempt was made to determine the minimum amount of meningioma in dura that is detectable by Raman spectroscopy. It is concluded that Raman spectra enable meningioma to be distinguished from dura, which makes Raman spectroscopy a viable candidate for guidance of surgical resection of meningioma.

## Introduction

Meningiomas are the most common tumors of the meninges, composed of neoplastic meningotheelial (arachnoidal) cells. They account for about 20% of all brain tumors.<sup>1</sup> There are many different histological subtypes of meningioma most of which are histologically benign.<sup>1</sup> Meningiomas are usually broadly attached to dura and are slowly growing tumors usually not infiltrating brain tissue. Despite their benign growth pattern these tumors are responsible for serious morbidity. Complete resection is the treatment of choice for lesions that are surgically accessible.<sup>2</sup> Although predominantly benign, meningiomas often recur, even following apparently complete resection.<sup>3</sup> 15-year recurrence rates of over 30% have been observed after complete tumor resection.<sup>4</sup> A number of studies have addressed predictive factors for recurrence of meningiomas. These include histological subtype, mitotic index, age, gender, and also the extent of surgical excision.<sup>4,5</sup> In a classic paper by Simpson this issue was addressed.<sup>6</sup> It was postulated that residual nests of meningioma within the regional dura would play a major role, confirmed by later studies.<sup>7,8</sup> Surgical removal of all dura infiltrated by tumor during resection is therefore important. Thusfar no objective per-operative tools are available to verify whether all tumor tissue has been removed.

In the study reported here, we have investigated the possibility of using Raman spectroscopy to distinguish between meningioma and dura to identify possibilities for the development of an *in vivo* Raman method as the basis for real-time guidance during surgical resection of meningioma. We used some of the most common subtypes of meningioma, e.g., syncytial and transitional subtypes, and the less common microcystic subtype of meningioma.<sup>1</sup> Raman spectroscopy is a non-destructive vibrational spectroscopic technique, based on inelastic scattering of light by the molecules in a sample. A Raman spectrum provides information about the molecular composition, molecular structures and molecular interactions in a tissue and can therefore be used to obtain specific biochemical information about a given tissue or disease state.<sup>9,10</sup> In recent years, significant progress has been reported in the application of Raman spectroscopy for *in vitro* characterization of tissues. A number of studies reported on Raman spectra of various normal tissues and on spectral differences between normal tissue and neoplastic tissue of the skin, colon, larynx, cervix and breast.<sup>11-20</sup> So far only few studies have reported on the use of Raman spectroscopy for brain tissue characterization. Mizuno *et al.* analyzed Raman spectra of different anatomical and functional structures of rat brain and they were the first to publish spectra of different brain tumors.<sup>21,22</sup> Wolthuis *et al.* demonstrated that water concentration in brain tissue can be very accurately determined by Raman spectroscopy.<sup>23</sup> Recently, we published the results of an *in vitro* study on human glioblastoma tissue describing the potential of Raman spectroscopy for brain biopsy guidance. In that study, a classification model, based on spectra obtained, for discrimination between vital and necrotic glioblastoma tissue yielded 100% accuracy.<sup>24</sup> The fact that Raman spectroscopy is noninvasive and does not rely on extrinsic contrast

enhancing agents makes it particularly attractive for *in vivo* use. Successful steps towards *in vivo* application of the technique, by means of fiber-optic probes have been reported. The potential of Raman spectroscopy for the clinical diagnosis of cervical precancers based on *in vivo* spectra has been published by Mahadevan-Jansen *et al.*<sup>25</sup> Buschman *et al.* obtained *in vivo* intravascular Raman spectra from arteries and Bakker Schut *et al.* reported on the *in vivo* detection of epithelial dysplasia in rat palate tissue.<sup>26,27</sup> More recently, the use of optical fiber probes by near-infrared Raman spectroscopy for diagnosis of lung cancer and for differentiation of colonic polyps during gastro-intestinal endoscopy has been demonstrated.<sup>28,29</sup> Several groups have reported on miniaturized fiber-optic probes which have enabled high quality *in vivo* Raman spectra to be obtained.<sup>30-32</sup>

Here we show that Raman spectra enable discrimination between dura and tumor for the three different subtypes of meningioma that were studied (e.g., transitional, syncytial, microcystic). We used Raman microspectroscopy to obtain spectra of unfixed thin sections of human dura and meningioma tissue samples. The thin sections were scanned to create pseudocolor Raman maps, which were compared with the histopathological evaluation of the same tissue sections. In this way we were able to identify the histological origin of the spectral features that were collected.

A classification model was developed which discriminates between dura and meningioma. A quantitative model was developed to predict the minimal amount of meningioma that still is detectable by Raman spectroscopy.

## Materials and Methods

### Sample Handling and Sample Preparation

The study was approved by the Medical Ethics Review Board of the Erasmus-university Medical Center Rotterdam and informed consent was obtained from each patient.

Tissue specimens originated from resection material obtained during neurosurgical procedures at the Neurosurgery Department of Erasmus-university Medical Center Rotterdam. Resection material was obtained from 20 patients (12 females, 8 males, mean age 59 years) of which 8 were with microcystic tumor type, 7 with transitional tumor type and 2 with syncytial tumor type. From three patients only healthy dura tissue was obtained.

After excision, tissue samples were snap frozen by immersion in liquid nitrogen and then stored at -80°C until further use. For Raman experiments, these frozen samples were cut into 25 µm thick sections with a microtome at -20°C and placed onto calcium fluoride (CaF<sub>2</sub>) microscope slides. These unfixed tissue sections were dried in air and used without further treatment. To confirm whether tissue was dura and/or tumor, 5 µm thick adjacent sections were also obtained and stained with hematoxylin and eosin (HE) for histopathological evaluation. Following Raman measurements, the 25 µm tissue sections were HE stained as well,

to provide a direct comparison of the Raman mapping results with the histopathology. In this study, a total of 38 Raman mapping sessions were performed on unstained cryosections of dura and meningioma tissues. Raman mapping experiments were performed on tissue samples either containing dura and tumor or only dura or only tumor. In some cases more than one sample was obtained from the same patient and sometimes more than one mapping experiment was performed on same sample.

## Raman Mapping

Raman spectra of the tissue sections were obtained by a near-infrared multichannel Raman microspectrometer built in-house. This system has been described in detail by van de Poll *et al.*<sup>33</sup> Laser light of 847 nm is focused on the sample by an 80x near-infrared optimized microscope objective (Olympus, Japan). The objective also collects light that is scattered by the sample, which is then analyzed by the spectrometer. Raman signal was collected in the spectral interval from 400 to 1800  $\text{cm}^{-1}$ , with a spectral resolution of 8  $\text{cm}^{-1}$ . Raman mapping procedure is detailed elsewhere.<sup>24</sup> Briefly, unstained cryosections (25  $\mu\text{m}$ ) of meningioma and/ or dura tissue were placed on an xyz- motorized, computer controlled sample stage (Leica DM STC, Cambridge, UK), which enabled automatic scanning of the sample. The area to be scanned and the scanning step size were chosen thereby dividing the area of interest into small square areas (hereafter referred to as Raman-pixels). Spectra were obtained consecutively from the tissue in each of these Raman pixels, the size of which varied between  $16\mu\text{m}^2$  ( $4 \times 4\mu\text{m}^2$ ) and  $900\mu\text{m}^2$ , ( $30 \times 30 \mu\text{m}^2$ ) depending on the size of tissue sections. The 80x microscope objective focused the laser light to a spot of less than  $1 \mu\text{m}^2$ . Therefore, to obtain a spectrum that is representative for the tissue in a Raman pixel, the area of the Raman pixel was scanned during each measurement. Tissue samples were excited with 70 - 80mW of laser power during Raman experiments. Spectra were obtained using 10 seconds of signal collection time per Raman-pixel.

## Reference Spectra

Reference spectra of collagen, cholesterol, cholesterol-linoleate, linoleic acid and calcium hydroxyapatite were obtained from commercially available compounds (Sigma-Aldrich Chemie, Zwijndrecht, The Netherlands).

## Raman Signal Analysis

The Raman data were analyzed with software developed in-house that operates in the Matlab environment (The MathWorks, Inc., Natick, MA, USA) using the multivariate statistical analysis toolbox PLS-toolbox 2.0.0c (Eigenvector Research, Inc., Manson, WA).

### *Pretreatment of Spectra*

The acquired spectra were first calibrated using Raman calibration standards as described earlier.<sup>34</sup> The reference spectrum of a tungsten-band lamp of known temperature was used to correct for the wavelength-dependent signal detection efficiency of the Raman setup. Subtraction of interfering background Raman signal originating in the optical elements in the laser light delivery pathway and the  $\text{CaF}_2$  slide was also included in the spectral pre-treatment.

### *K-means Cluster Analysis*

Raman maps were constructed from the spectral data set using multivariate statistical techniques. Principal component analysis (PCA) was used to orthogonalize and reduce the number of parameters needed to represent the variance in the spectral data set.<sup>35</sup> The PCA scores accounting for 99.9% of the variance captured served as input for K-means cluster analysis (KCA). KCA, which can easily handle large amounts of data as obtained during Raman mapping experiments, was performed to find groups of spectra that have resembling spectral characteristics.<sup>36</sup> The algorithm was initiated by allowing the user to choose the number of clusters. The criteria used to determine the number of clusters to be included in the analysis were that the final cluster averaged spectra displayed meaningful spectral differences (i.e., above noise level) and that the clusters could be related to histologically distinct areas in the tissue sections. The cluster-membership information was plotted as a pseudocolor map by assigning a color to each different cluster.

The location of each differently colored area in the pseudocolor Raman maps was compared with the histopathology. Depending on whether different colors corresponded with dura or with tumor regions within HE-stained section, each Raman cluster was labeled “dura” or “tumor”.

### *Raman Difference Spectra*

Information about differences in biochemical composition of the various structures can be extracted from “positive” difference spectra, which are calculated by scaled subtraction of the cluster averaged spectra from each other. In short: for two given spectra, A and B, a difference spectrum A-B is calculated, where B is scaled in such a way that the difference spectrum does not show negative Raman features. The resulting difference spectrum gives a good impression of which molecular species are present in a relatively higher amount in spectrum A than in spectrum B.

### *Hierarchical Cluster Analysis of Cluster Averages*

Based on the histopathological cluster assignment, a data set consisting of cluster averages of meningioma and dura spectra was created to analyse the influence of inter patient variance in discriminating between meningioma and dura spectra. (A cluster averaged

spectrum dubbed “cluster average”, is the mean of the spectra contained in 1 cluster). The dataset served as input for a hierarchical cluster analysis (HCA), using Ward’s clustering algorithm and the Euclidean distance measure. Before cluster analysis, the spectra were first scatter-corrected using a 5<sup>th</sup> order polynomial.<sup>37</sup> Then a PCA was performed on this data set to obtain a representation of the spectra in a reduced number of orthogonal variables. The scores on these new variables were used as input for the HCA.

#### *Linear Discriminant Analysis (LDA) to Discriminate between Meningioma and Dura*

An LDA model was built to assess the possibilities for discriminating between meningioma and dura spectra. LDA is a supervised modeling technique that finds the best linear combination of variables to discriminate between the two groups.<sup>38</sup> As input for the LDA, the scores on the first two principal components, which showed the highest discrimination between meningioma and dura, were used. The LDA model was evaluated with leave-one-patient-out testing. In this test, the classification of all cluster averages from maps from one patient is predicted using an LDA model that has been developed on cluster averaged spectra from the Raman maps of all other patients.

#### *Partial Least Squares (PLS) to Predict the Tumor Amount in Mixed Dura- Meningioma Spectra*

In clinical practice, in which spectra would be obtained *in vivo* e.g., by means of fiber-optic probes, one will also measure spectra that do not solely consist of one tissue type. Where the tumor infiltrates the dura, one will measure mixed spectra containing signal contributions of both dura and tumor tissue, especially near the tumor border, and determination of residual tumor in resection border is of great importance. To assess the accuracy with which one can detect the amount of tumor in a mixed spectrum we used the Partial Least Squares (PLS) calibration method. PLS is a multivariate calibration technique by which information about the concentration of a constituent in a sample can be obtained. The PLS algorithm determines which spectral information best correlates with known concentrations of such a constituent. The output of the PLS algorithm, which correlates spectral features of training samples with known concentrations of the constituent in these samples, is a regression vector. Multiplication of this regression vector with a spectrum of a sample containing an unknown amount of the constituent yields a prediction for the concentration of the constituent in that sample.<sup>39</sup> To develop the PLS model we used cluster averaged spectra of dura and cluster averaged spectra of meningioma obtained from the Raman mapping experiments. These spectra were assumed to represent examples of 100% tumor tissue and 100% dura. As input to the PLS algorithm we used a data set of mixed dura-meningioma spectra, that was constructed by random selection of a meningioma cluster average spectrum, multiplying that spectrum by a tumor concentration factor, and then adding a dura cluster average spectrum, multiplied by 1 minus that same concentration factor.

In this way 500 spectra were constructed using one half of the meningioma and dura spectra, and representing a tumor concentration range between 0-100%. The PLS model was then tested using 500 spectra, constructed from the other half of the meningioma and dura spectra. Tissue samples obtained from 10 patients (6 females, 4 males, median age 58 years) were used to construct the model data set, and tissue samples from 10 other patients (6 females, 4 males, median age 60 years) were used to construct the test data set.

## Results

Thirty-eight Raman mapping experiments were performed on unstained, unfixed cryosections of meningioma and/or dura tissue samples obtained from 20 patients. The maps varied in size from 225 pixels (in one case, in which a small structure within a section was mapped at high resolution) to 16 006 pixels (for larger areas in tissue sections). In all samples, the pseudocolor Raman maps and the microscopic image of the HE stained section were found to correlate very well.

An example of the results of a Raman mapping experiment on a thin section of human meningioma (microcystic subtype) attached to dura is shown in Figure 1. The area within the unstained tissue section that was selected for Raman mapping ( $1392\ \mu\text{m} \times 828\ \mu\text{m}$ ) is shown in the bright field image in panel A. The Raman image (8084 spectra, lateral resolution  $12\ \mu\text{m}$ ) based on a three-cluster KCA is shown in panel B. Comparison of pseudocolor Raman map with the microscopic image of the tissue section after HE staining (panel C) enabled identification of cluster 1 as meningioma (labeled “m” in panel C) and cluster 2 as dura (labeled “d” in panel C). Cluster 3 represents areas where no tissue was present. The cluster averaged Raman spectra are shown in panel D. It clearly shows that the cluster averaged spectrum of meningioma (spectrum a) is markedly different from the cluster averaged spectrum of dura (spectrum b). The bands at about  $854\ \text{cm}^{-1}$  and  $938\ \text{cm}^{-1}$  in the dura spectrum are a typical feature of the Raman signal of collagen (spectrum c). In all tissue samples dura and meningioma were clearly separated in the Raman maps. In some cases a strong biochemical heterogeneity was noticed in meningioma tissue. In a number of Raman maps different tumor tissue regions ended up in different clusters reflecting the regional variance in the biochemical composition of meningioma (Figure 2). The bright field image of the area scanned ( $576\ \mu\text{m} \times 520\ \mu\text{m}$ ) within a frozen section of microcystic meningioma is shown in panel A. In this image numerous crystal-like structures can be observed at the left side of the tissue area that was scanned. In the pseudocolor Raman map shown in panel B (4680 spectra, lateral resolution  $8\ \mu\text{m}$ ) tumor tissue is divided into two clusters (clusters 1 and 2). The area where no tissue was present corresponds with cluster 3. The microscopic image of the HE stained tissue section is shown in panel C. From a comparison of the Raman map with the unstained and stained image it can be seen that cluster 1 corresponds with

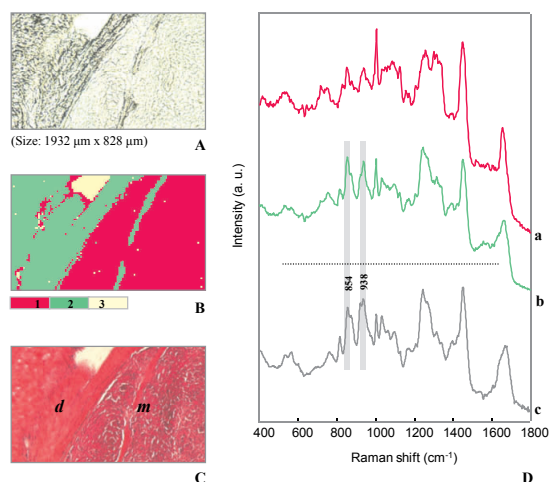


**Figure 1.** Discrimination between dura and meningioma in a KCA pseudocolor map based on the Raman spectra. **A**, Photograph of unstained frozen section of meningioma (microcystic subtype) attached to dura (original magnification x5). **B**, Pseudocolor Raman map of the tissue section shown in A, based on a three-cluster KCA of the collected spectra (pixel size:  $12 \times 12 \mu\text{m}^2$ ,  $116 \times 69$  pixels). **C**, Microscopic image of the tissue section of panel A after HE staining. Dura is indicated with “d”, meningioma with “m”. As follows from a comparison with the image of the HE stained tissue section, cluster 1 corresponds to meningioma and cluster 2 corresponds to dura; (Cluster 3 represents the areas where no tissue is present in the section). **D**, Cluster averages of Raman spectra collected from the scanned area. **(a)** Average spectrum of meningioma. **(b)** Average spectrum of dura. **(c)** Spectrum of pure collagen.

the tumor area on the left side of both images. In the HE-image, the tumor present in this area contains vacuoles. This implies that some of the tumor contents have been washed out during the staining procedure. The rest of the tumor is captured by cluster 2. Panel D shows the averages of the spectra belonging to cluster 1 (spectrum a) and to cluster 2 (spectrum b), which serves to illustrate the spectral variance encountered in tumor tissue. The characteristic differences were highlighted by calculating a positive difference spectrum (see Materials and Methods) a minus b (spectrum a – b, 2 times enlarged). The difference spectrum is very similar to a cholesterol-ester spectrum (such as e.g., cholesterol-linoleate, spectrum c). This suggests that cholesterol (-esters) signal contributions (highlighted with gray bars) are more prominent in the average spectrum of the tumor area represented by cluster 1 than in the tumor area represented by cluster 2. Analysis of Raman spectra from microcystic meningiomas (from five patients) and of transitional meningiomas (from two patients) shows that the presence of esterified cholesterol is one of the most prominent biochemical differences between different regions in these tumors.

Calcifications were observed in two frozen sections of microcystic and transitional meningioma. As revealed by the evaluation of HE-stained section (not shown), these deposits correspond to psammoma bodies. An example of a psammoma body in the unstained

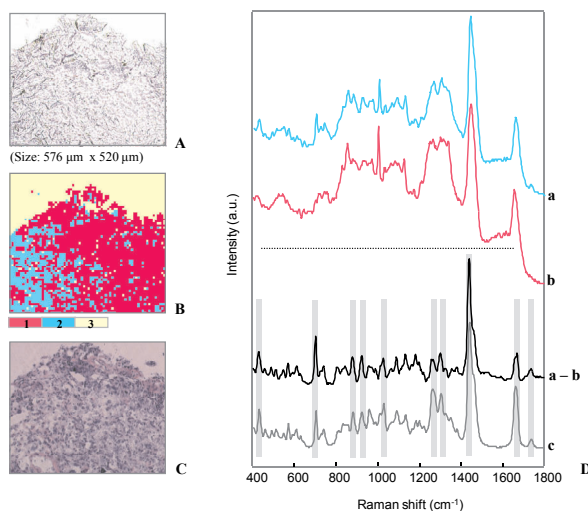


**Figure 2.** Regional heterogeneity in a biochemical composition of meningioma reflected in a KCA pseudocolor map based on the Raman spectra. **A**, Photograph of unstained frozen section of meningioma (microcystic subtype), (original magnification x5). **B**, Pseudocolor Raman map of the tissue section shown in A, based on a three-cluster KCA of the collected spectra (pixel size:  $8 \times 8 \mu\text{m}^2$ ,  $72 \times 65$  pixels). In panel B cluster 1 and 2 corresponds to different areas of meningioma; (Cluster 3 represents the areas where no tissue was present in the section). **C**, Microscopic image of the tissue section of panel A after HE staining. **D**: Cluster averages of Raman spectra collected from the scanned area. **(a)** Average spectrum of the area of meningioma captured by cluster 1 in a Raman map. **(b)** Average spectrum of the area of meningioma captured by cluster 2 in a Raman map. **(a - b)** positive difference spectrum of spectra **a** and **b** (a minus b), enlarged 2 times for clarity. **(c)** Spectrum of pure cholesterol-linoleate (divided by factor 3). Spectral regions of the most prominent resemblance are highlighted by gray bars. (For clarity the spectra have been shifted along the ordinate.)

meningioma tissue section is shown in Figure 3A (scanned area measured  $60\mu\text{m} \times 60\mu\text{m}$ ). The three-cluster Raman map (225 spectra, lateral resolution  $4\mu\text{m}$ ) is shown in panel B. Spectra a and b in panel C are cluster averaged spectra from the deposit (cluster 1 in panel B) and from the surrounding tissue, respectively (cluster 2 in panel B). A positive difference spectrum a minus b (spectrum a - b) almost completely resembles the spectrum of pure calcium hydroxyapatite (spectrum c).

To evaluate the possibility to use Raman spectra to distinguish between tumor tissue and dura, the 115 cluster averaged spectra obtained from the 38 Raman maps were used as input for a hierarchical cluster analysis (see section on materials & methods). Based on the histopathological evaluation, 64 clusters were labeled as “meningioma” and 51 as “dura”. A hierarchical cluster analysis (HCA) of this dataset resulted in the dendrogram of Figure 4 (panel A), which shows that there is a clear distinction between the meningioma spectra and the dura spectra.

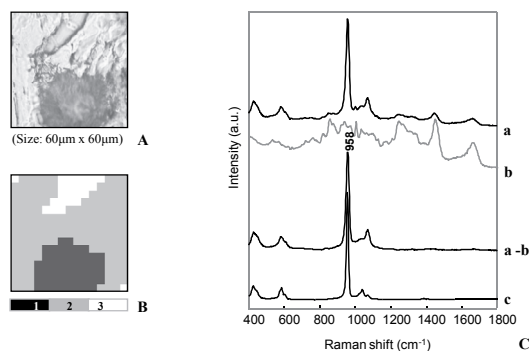


**Figure 3.** **A**, Bright-field image of an area in meningioma (transitional subtype) tissue section containing psammoma body (original magnification x80). **B**, Raman map, based on the KCA with three clusters (pixel size:  $4 \times 4 \mu\text{m}^2$ ,  $15 \times 15$  pixels). **C**, Cluster averages of Raman spectra collected from the scanned area. **(a)** Average spectrum of psammoma body represented by cluster 1 in a Raman map. **(b)** Average spectrum of the tissue area surrounding psammoma body captured by cluster 2 in a Raman map. **(a - b)** Positive difference spectrum of spectra **a** and **b** (a minus b). **(c)** Spectrum of pure calcium hydroxyapatite (divided by factor 20). (For clarity of presentation the spectra have been shifted along the ordinate.)

The accuracy in predicting tissue pathology, i.e., meningioma or dura, of an unknown sample was examined using LDA. PCA was first applied to orthogonalize and reduce the number of parameters needed to represent the variance in this data set. The scores on the first two principal components, together accounting for 80% of the variance in the data set, resulted in the largest separation between meningioma and dura, and were used as input for the LDA model. The model was validated using a leave-one-patient-out cross-validation, yielding a 100% accuracy (as would be expected based on the result of the hierarchical cluster analysis).

The average spectrum of all dura clusters and the average spectrum of all meningioma clusters from the 38 Raman experiments are shown in panel B of Figure 4 (spectra a and b, respectively). A positive difference spectrum “meningioma minus dura” was calculated (spectrum b - a). A comparison with typical lipid spectra (e.g., spectra of pure cholesterol-linoleate and pure linoleic acid, c and d respectively) makes clear that the difference spectrum contains, among other features, a combination of bands that are characteristic for lipids. This concerns the bands at about  $1260 \text{ cm}^{-1}$  (in-plane  $\text{CH}_2$  deformation),  $1300 \text{ cm}^{-1}$  ( $\text{CH}_2$ -twist and wagging),  $1440 \text{ cm}^{-1}$  ( $\text{CH}_2$  bending) and  $1656 \text{ cm}^{-1}$  ( $\text{C}=\text{C}$  stretching). Note also the presence of small peak at  $1734 \text{ cm}^{-1}$  that is due to esters ( $\text{C}=\text{O}$  stretching). This implies that the lipid content of the tumor tissue is significantly higher than that of the dura.

In clinical practice fiber-optic probes would be used that have a sample volume in the order of  $10^{-3}$  to  $10^{-1} \text{ mm}^3$ . It is then unavoidable that spectra will also be obtained of tissue volumes containing a mixture of meningioma and dura. It is important to assess the sensitivity with which tumor tissue can be detected in such a mixed tissue volume. A first attempt to ad-

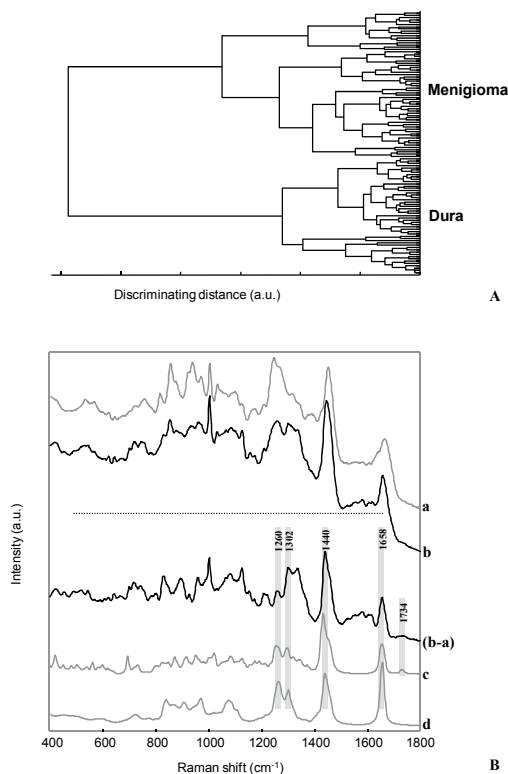


**Figure 4.** **A**, Dendrogram from hierarchical cluster analysis of dura and meningioma spectral cluster averages, from all experiments. Dissimilarity distance is given by arbitrary units (a.u.). **B**, **(a)** Mean dura spectrum, calculated from all dura cluster averages. **(b)** Mean meningioma spectrum, calculated from all meningioma cluster averages. **(b – a)** Positive difference spectrum of spectra **b** and **a** (b minus a). **(c)** Spectrum of pure cholesterol-linoleate. **(d)** Spectrum of pure linoleic acid. Grey bars have been used to highlight areas of significant spectral overlap.

dress this question was made by means of a Partial Least Squares (PLS) calibration method. It was used to estimate the accuracy with which the amount of meningioma in a mixed meningioma-dura spectrum can be determined. Mixed dura-meningioma spectra were constructed from the cluster averaged dura and meningioma spectra of the Raman maps. These served both as input spectra and as test spectra for the PLS model (see Materials & Methods). The quantitative prediction error of this model, expressed as the root mean squared error of prediction (RMSEP), is about 13%.

This PLS model can also be used to predict the amount of meningioma signal in the individual spectra of a map. This is illustrated in Figure 5. Panel A shows the area of an unstained tissue section that was scanned (2300μm x 1400μm, lateral resolution 20μm). Panel B is a gray-scale Raman image, based on the predicted amount of meningioma in each pixel (8050

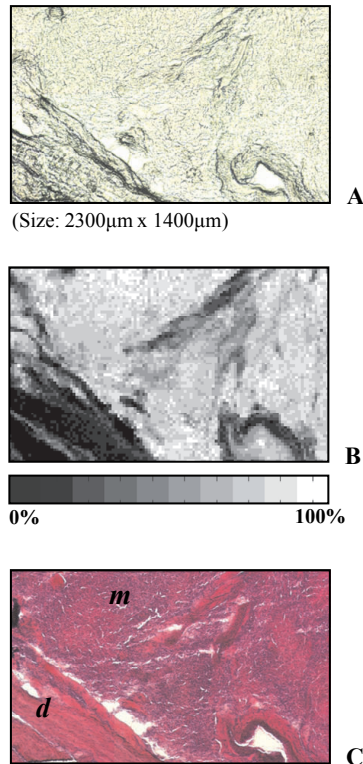


**Figure 5.** **A**, Photomicrograph (original magnification x5) of an unstained tissue section, selected for Raman microspectroscopic mapping and containing meningioma and dura. **B**, Raman image depicting tumor concentration, based on PLS. The PLS model was applied to determine the tumor concentration in each image pixel. A gray scale is used to depict tumor concentration (black, normal dura; white, tumor). **C**, Photomicrograph (original magnification x5) of the same tissue section after HE staining for histological evaluation following Raman measurement (dura designated with *d* and meningioma with *m*).

spectra; black indicates normal dura, white indicates meningioma). This predicted image shows a clear correspondence with the HE-stained section (panel C).

## Discussion

The results of this study show that meningiomas and dura can be distinguished on the basis of their Raman spectra. The tissue classification model that was developed in this *in vitro* study (with still a relatively low number of samples) had a 100%-accuracy. This bodes well for the development of an *in vivo* technique in which a fiber-optic probe would be used to obtain tissue spectra.

To reduce the risk of tumor recurrence it is important to achieve complete tumor resection during surgery. Therefore, a first analysis was made to estimate the minimum fraction of tumor tissue in a measurement volume that can still be detected within the dura. A PLS analysis showed that the relative amount of meningioma in a mixed meningioma-dura sample can be determined with an accuracy of about 13 percent. Assuming a normal distribution of the error, an RMSEP of 13% implies that when the PLS algorithm predicts 13% tumor to be present in the measurement volume, the certainty that there is actually tumor present is 68.3%. When the PLS algorithm predicts 26% (i.e., 2 times RMSEP) the certainty that there is actually tumor present is 95%. The current PLS model is only an approximation. The meningioma and dura cluster averaged spectra that were used as input for the PLS model are not pure meningioma or dura spectra. In many cases a meningioma cluster averaged spectrum will contain some contribution from dura and vice versa. This limits the performance of the PLS model. Therefore, a better identification of pure meningioma and dura spectra will most likely lead to a PLS model with higher accuracy; i.e., a higher sensitivity for the presence of tumor in the measurement volume.

Large differences exist between the Raman spectra of dura and meningioma, indicative of considerable large differences in molecular composition of the two tissues. Raman spectra of dura, which contains large amounts of collagen,<sup>40</sup> are characterized by their very intense collagen signatures, in contrast to meningioma tissues. Conversely, the lipid content of meningioma tissues is significantly higher than that of dura. Various studies have reported on the lipid content of meningiomas.<sup>41,42</sup> It was observed that tumor tissue composition was quite heterogeneous in a number of cases of microcystic and transitional type meningioma, especially with respect to cholesterol and cholesterol ester concentration. This heterogeneity complements literature reports showing the presence of free cholesterol and esterified cholesterol in human meningioma tissues.<sup>41,42</sup> In Raman spectra from parts of meningioma (microcystic and transitional subtype) that contained characteristic psammoma bodies an intense band was observed that is assigned to calcium hydroxyapatite. This is in accordance with literature reports on biochemical composition of psammoma bodies based on their tinctorial properties.<sup>43</sup> The present preliminary results pave the way for the development of an *in vivo* Raman spectroscopic method for the real-time guidance of meningioma resection. The goal will be to enhance the ability to detect residual tumor within the dura during surgery.

Raman spectroscopy is highly suitable for *in vivo* application, as it is non-invasive and can be applied using special fiber-optic probes optimized for the size and location of the actual measurement volume of the tissue.<sup>28-30</sup> The feasibility of *in vivo* Raman spectroscopy has been proven in a number of recent articles.<sup>24,27</sup> Based on the results presented here we are currently taking first steps in development Raman spectroscopic method for real-time guidance of meningioma resection.

It may of course be expected that the difference in experimental conditions between the current experiments and *in vivo* experiments (air-dried vs. hydrated tissue, room temperature vs. body temperature) affect the spectra.<sup>44</sup> However it is unlikely that this will affect the possibility to discriminate between normal tissue and tumor tissue. The laser powers that were applied in the current investigation can also easily be applied *in vivo*. In a previous work we have shown that the temperature increase in brain tissue as a result of irradiation with laser light of 830nm up to 250 mW is in the order of  $\sim 2^{\circ}\text{C}$ .<sup>45</sup> Successful development of Raman spectroscopic method for real-time guidance will decrease the incidence of tumor recurrence, which is attributed to incomplete tumor resection.

## References

1. Louis D. N.; Scheithauer B. W.; Budka H.; von Deimling A.; Kepes J. J. In: *World Health Organization Classification of Tumors*; Kleihues P.; Cavenee W. K.; Eds.; IARC Press: Lyon, 2000; Chapter 11.
2. Demonte F. *Oncology* 1995, 9, 83-96.
3. Kamitani H.; Masuzawa H.; Kanazawa I.; Kubo T. *Surg. Neurol.* 2001, 56, 228 – 235.
4. Mirimanoff R. O.; Dosoretz D.E.; Linggood R. M.; Ojemann R.G.; Martuza R. L. *J. Neurosurg.* 1985, 62, 18-24.
5. Mahmood A.; Qureshi N. H.; Malik G. M. *Acta Neurochir. (Wien)* 1994; 126:53-8.
6. Simpson D. J. *Neurol. Neurosurg. Psychiatry.* 1957, 20, 22-39.
7. Borovich B.; Doron Y. *J. Neurosurg.* 1986, 64, 58-63.
8. Jaaskelainen J. *Surg. Neurol.* 1986, 26, 461-469.
9. Tu A. T. *Basic concept and elementary theory: Raman spectroscopy in biology*. John Wiley & Sons: NewYork; 1982.
10. Puppels G. J.; De Mull F. F.; Otto C.; Greve J.; Arndt-Jovin D. J.; Jovin T. M. *Nature* 1990, 347, 301-303.
11. De Jong B. W. D.; Bakker Schut T. C.; Wolffenbuttel K. P.; Nijman J. M.; Kok D. J.; Puppels G. J. *J. Urol.* 2002, 168, 1771 – 1778.
12. Kneipp J.; Bakker Schut T. C.; Kliffen M.; Menke-Pluijmers M.; Puppels G. J. *Vibrational Spectroscopy* 2003, 32, 67-74.
13. Koljenović S.; Bakker Schut T. C.; van Meerbeeck J. P.; Maat AP, Burgers S. A.; Zondervan P. E.; Kros J. M.; Puppels G. J. *J. Biomed. Opt.* 2004, 6, 1187-1197.
14. Mahadevan-Jansen A.; Mitchell M.F.; Ramanujam N.; Malpica A.; Thomasen S.; Utzinger U.; Richards-Kortum R. *Photochem. Photobiol.* 1998, 68,123-132.
15. Manoharan R.; Schafer K.; Perelman L.; Wu J.; Chen K.; Deinum G.; Fitzmaurice M.; Myles J.; Crowe J.; Dasari R. R.; Feld M. S. *Photochem. Photobiol.* 1998, 67, 15-22.
16. Boustany N. N.; Crawford J. M.; Manoharan R.; Dasari R. R.; Feld M. S. *Lab. Invest.* 1999, 79,1201-1214.
17. Nijssen A.; Bakker Schut T. C.; Heule F.; Caspers P. J.; Hayes D. P.; Neumann M. H.; Puppels G. J. *J. Invest. Dermatol.* 2002, 119, 64- 69.
18. Stone N.; Kendall C.; Shepherd N.; Crow P.; Barr H. *Journal of Raman spectroscopy.* 2002, 33, 564-573.
19. Haka A. S.; Shafer-Peltier K. E; Fitzmaurice M.; Crowe J.; Dasari R. R.; Feld M. S. *Proc Natl Acad Sci U S A.* 2005, 102, 12371-12376.
20. Lau D. P; Huang Z.; Lui H.; Anderson D. W.; Berean K.; Morrison M. D.; Shen L.; Zeng H. *Lasers Surg Med.* 2005, 9999, 1-9.
21. Mizuno A.; Hayashi T.; Tashibu K.; Maraishi S.; Kawauchi K.; Ozaki Y. *Neurosci. Lett.* 1992, 141, 47-52.
22. Mizuno A.; Kitajima H.; Kawauchi K.; Muraishi S.; Ozaki Y. *Journal of Raman spectroscopy.* 1994, 25, 25-29.
23. Wolthuis R.; van Aken M.; Fountas K.; Robinson Jr. J. S.; Bruining H. A.; Puppels G. J. *Anal. Chem.* 2001, 73, 3915-3920.
24. Koljenović S.; Choo-Smith L-P; Bakker Schut T. C.; Kros J. M.; van den Berge H. J.; Puppels G. J. *Lab. Invest.* 2002; 82, 1265-1277.
25. Mahadevan-Jansen A.; Mitchell M. F.; Ramanujam N.; Utzinger U.; Richards-Kortum R. *Photochem. Photobiol.* 1998, 68, 427-431.

26. Buschman R.; Marple E. T.; Wach M.L.; Bennett B.; Bakker Schut T. C.; Bruining H. A.; Bruschke A. V.; van der Laarse A.; Puppels G. J. *Anal. Chem.* 2000, 72, 3771-3775.
27. Bakker Schut T. C.; Witjes M. J. H.; Sterenborg H. J. C.; Speelman O. C.; Roodenburg J. L. N.; Marple E. T.; Bruining H. A.; Puppels G. P. *Anal. Chem.* 2000, 72, 6010-6018.
28. Huang Z.; McWilliams A.; Lui H.; McLean D.; Lam D. I. S.; Zeng H. *Int. J. Cancer.* 2003, 107, 1047-1052.
29. Molckovsky A.; Wong Kee Song L-M.; Shim M. G.; Marcon N. E.; Wilson B. C. *Gastrointest. Endosc.* 2003, 57, 396-402.
30. Puppels G. J.; van Aken M.; Wolthuis R.; Caspers P.J.; Bakker Schut T. C.; Bruining H. A.; Romer T. J.; Buschman H. P. J.; Wach M.; Robinson J. S. In *in vivo tissue characterization by Raman spectroscopy*. Proc SPIE conference proceedings vol. 3257; Mantsch H. H., Jackson M., Katzir A., Eds.; Washington, 1998, 78 – 85.
31. Shim M. G.; Song L. M.; Marcon N. E.; Wilson B. C. *Photochem. Photobiol.* 2000, 72, 146–150.
32. Motz J. T.; Hunter M.; Galindo L. H.; Gradecki J. A.; Kramer J. R.; Dasari R. R.; Feld M. S. *Appl. Opt.* 2004, 20, 542–554.
33. van de Poll S. W. E.; Romer T. J.; Volger O. L.; Delsing D. J. M.; Bakker Schut T. C.; Princen H. M. G.; Jukema J. W.; Havekes L.; van der Laarse A.; Puppels G. J. *Arterioscler. Thromb. Vasc. Biol.* 2001, 21, 1630-1635.
34. Wolthuis R.; Bakker Schut T. C.; Caspers P. J.; Buschman H. P.; Römer T. J.; Bruining H. A.; Puppels G. J. In: *Fluorescent and luminescent probes for biological activity*; Mason W. T., Ed.; Academic Press: London, 1999; Chapter 32.
35. Jolliffe I. T. *Principal component analysis*. Springer-Verlag: New York, 1986.
36. Jain A. K.; Dubes R. C. *Algorithms for clustering data*. Prentice Hall: Englewood Cliffs, 1988.
37. Martens H.; Stark E. J. *Pharm. Biomed. Anal.* 1991, 9, 625-635.
38. Tabachnick B.; Fidell L. *Using Multivariate Statistics*. Harper Collins Publishers: New York, 1989.
39. Haaland D. M.; Thomas E. V. *Anal. Chem.* 1988, 60, 1193-1202.
40. Stevens A.; Lowe J. *Human histology*. Times Mirror International Publishers Limited: London, 1997.
41. Tugnoli V.; Tosi M. R.; Tinti A.; Trincherio A.; Bottura G.; Fini G. *Biopolymers.* 2001, 61, 297-306.
42. Kokoglu E.; Gorseval A.; Sonmez H.; Ozyurt E. *Cancer. Lett.* 1992, 65, 169-171.
43. Bruner J. M.; Tien R. D.; Enterline D. In: *Russell and Rubinstein's Pathology of tumors of the nervous system*; Bigner D. D., McLendon R. E., Bruner J. M., Eds.; Oxford University Press: New York, 1998, 69-139.
44. Mourant J. R.; Gibson R. R.; Johnson T. M.; Carpenter S.; Short K. W.; Yamada Y. R.; Freyer J. P. *Phys Med Biol.* 2003, 48, 243-257.
45. Puppels G. J.; Bakker Schut T. C.; Caspers P. J.; Wolthuis R.; van Aken M.; van der Laarse A.; Bruining H. A.; Buschman H.; Shim M. G.; Wilson B. C. In: *"Handbook for Raman spectroscopy"*; Lewis I. R. and Edwards H. G. M., Eds.; Marcel Dekker, Inc: New York, 2001, 549-574.



# Discriminating Vital Tumor from Necrotic Tissue in Human Glioblastoma Tissue Samples by Raman Spectroscopy

*Laboratory Investigation*  
2002, 82 (10): 1265-1277

4

S. Koljenović  
L.P. Choo Smith  
T.C. Bakker Schut  
J.M. Kros  
H.S. van de Berge  
G.J. Puppels

## Abstract

Vital and necrotic glioblastoma tissues were studied by Raman microspectroscopy to identify possibilities for the development of an *in vivo* Raman method for real-time intra-operative brain biopsy guidance. The histological malignancy grade of gliomas depends on the presence of parameters such as endothelial proliferation and necrosis, which are often not evenly distributed within the tumor. Because tissue samples obtained by stereotactic surgery are relatively small, sampling errors may easily occur by missing these crucial features. Although necrosis is important for grading, specimens containing only necrosis are diagnostically useless. Raman microspectroscopic mapping experiments were performed on unfixed cryosections of glioblastoma, obtained from 20 patients. Following spectral acquisition, a clustering analysis was performed, resulting in groups of similar spectra. Each cluster was assigned a color, and pseudocolor Raman maps of the tissue sections were constructed. Following the Raman experiments, the tissue sections were stained for histopathological analysis, enabling identification of the histological origin of the Raman spectra and assignment of the Raman spectral clusters to either vital or necrotic tissue. A classification model for discrimination between vital and necrotic tumor tissue based on linear discriminant analysis was developed. The classification model was evaluated using independent Raman data obtained from nine other tissue sections and yielded 100% accuracy. Information about the biochemical differences between necrosis and vital tumor was obtained by the analysis of difference spectra. Necrotic tissue was found to consistently contain higher levels of cholesterol (esters). This *in vitro* result indicates that Raman spectra contain the information to distinguish vital glioblastoma from necrosis and makes Raman spectroscopy a powerful candidate for guidance of stereotactic brain biopsy.

## Introduction

The most common group of primary brain tumors are the gliomas, consisting largely of tumors of astrocytic or oligodendroglial lineage. These tumors are graded according to histopathological characteristics, and tumors of the highest malignancy grade are called glioblastomas. Within the glioma group, the glioblastomas occur most frequently.<sup>1</sup> Tumor tissue samples are mainly obtained by stereotactic surgery. This procedure is particularly suitable for taking biopsies from parts of the brain that are not otherwise accessible. An obvious disadvantage of stereotactic surgery is the fact that the specimens are relatively small.<sup>2,4</sup> The designation of a malignancy grade to gliomas occurs according to the presence of histological parameters such as endothelial proliferation and necrosis, which are often not evenly distributed throughout the sample.<sup>1,5,6</sup> Sampling errors obviously will result in the underestimation of the malignancy grade of the gliomas. Further, despite the fact that necrosis is important for grading, a diagnosis cannot be made when only necrotic tissue is present in the sample.<sup>2</sup> In some cases the tumor component consisting of necrosis may comprise more than 80% of the total volume.<sup>1</sup>

Although the stereotactic biopsy procedure is generally supported by computed tomography (CT) or magnetic resonance imaging (MRI) guidance, these techniques only provide limited clues as to the histological composition of the tumor. Hence, there is a need for guidance during the stereotactic biopsy procedure. Such tools will result in higher quality tissue specimens for histopathological evaluation. In recent studies water suppressed <sup>1</sup>H magnetic resonance spectroscopy (MRS) has been put forward as a non invasive way for detecting significant differences between the *in vivo* spectra of tumor, necrosis and healthy brain tissue<sup>7-13</sup> and for targeting during brain biopsy.<sup>14</sup> In the latter study, all biopsy material obtained under MRS-guidance was reported to be useful for diagnosis. MRS adds valuable information to intraoperative MR imaging. However, the cost and size of the instruments may hamper the widespread use of MRS.

In the study reported here, we have investigated the possibility of using Raman spectroscopy to distinguish between vital tumor tissue and necrosis to identify possibilities for the development of an *in vivo* Raman method as the basis for intraoperative brain biopsy guidance. Raman spectroscopy is a nondestructive vibrational spectroscopic technique, based on inelastic scattering of light by the molecules in a sample. A Raman spectrum provides information about the molecular composition, molecular structures and molecular interactions in a tissue.<sup>15</sup> Different types of tissue will vary in their overall molecular composition. Therefore their Raman spectra will also be different, and can be used as tissue-specific spectroscopic fingerprints. In addition, pathological changes in molecular composition or structure are reflected in the spectra, enabling development of diagnostic tools based on Raman spectroscopy. In recent years, significant progress has been reported in the application of Raman spectroscopy for *ex vivo* and *in vivo* tissue characterization.<sup>16-29</sup> So far only few

studies have reported on the use of Raman spectroscopy for brain tissue characterization. Mizuno *et al.* analyzed Raman spectra of different anatomical and functional structures of rat brain.<sup>30</sup> Ong *et al.* showed that Raman spectroscopy can be used to identify the substantia nigra of monkey brain.<sup>31</sup> Recently we showed that Raman spectroscopy can be used to very accurately determine water concentration in brain tissue.<sup>32</sup> In 1994 Mizuno *et al.* were the first to publish spectra of different brain tumors.<sup>33</sup>

Here we used Raman microspectroscopy to obtain spectra of unfixed thin sections of human glioblastoma tissue samples. The thin sections were scanned to create pseudocolor Raman maps, which were compared with the histopathology of the same tissue sections. We were able to identify the histological origin of the spectral features that were collected. A classification model was then developed which distinguishes between vital tumor tissue and necrosis based on the Raman spectra of the tissue under investigation. An independent data set was used to evaluate the model.

## Materials and Methods

### Patient Samples

The study was approved by the Medical Ethics Review Board of the University Hospital Rotterdam “Dijkzigt”. Informed consent was obtained from each patient.

### Sample Handling and Sample Preparation

Tissue specimens originated from resection material or from biopsies obtained during neurosurgical procedures at the Neurosurgery Department of University Hospital Rotterdam “Dijkzigt”. After excision, tissue samples were snap-frozen by immersion in liquid nitrogen and stored at  $-80^{\circ}\text{C}$  until further use. For Raman experiments, these frozen samples were cut into  $25\text{-}\mu\text{m}$ -thick sections using a cryotome and placed onto calcium fluoride ( $\text{CaF}_2$ ) microscope slides and allowed to dry in air. The unfixed tissue sections were used without further treatment. During cryotoming,  $5\text{-}\mu\text{m}$ -thick adjacent sections were also prepared. These thinner sections were stained with hematoxylin and eosin (HE) and histopathologically evaluated to identify regions of vital tissue and regions of necrosis according to the World Health Organization criteria.<sup>1</sup> Bright-field images of the unstained tissue sections revealed some heterogeneity in tissue structure, which could be linked to the structural heterogeneity observed in the adjacent stained sections. This assessment was used to select regions in the tissue sections, mostly containing both vital glioblastoma tissue and necrosis for Raman mapping. Following Raman measurements, the  $25\text{-}\mu\text{m}$  tissue sections were HE stained as well, to provide a direct comparison of the Raman mapping results with the histopathology. In this study, a total of 24 Raman mapping sessions were performed on unstained cryosections of glioblastoma tissue derived from 20 patients.

## Reference Spectra

To obtain reference spectra of cholesterol, cholesterol linoleate, cholesterol oleate, calcium hydroxyapatite and glycogen, commercially available compounds were used (Sigma-Aldrich Chemie, Zwijndrecht, The Netherlands).

## Raman Microspectrometer

Raman spectra of the tissue sections were obtained by a near-infrared multichannel Raman microspectrometer built in-house. Briefly, the setup consists of a microscope (DM-RXE, Leica, Cambridge, UK) coupled to a Raman spectrometer (System 100, Renishaw, Wotton under Edge, UK). Laser light of 847 nm is focused on the sample by an x80 NIR optimized objective (Olympus, Japan). The objective also collects light that is scattered by the sample, which is then analyzed by the spectrometer. Raman signal was collected in the spectral interval from 400 to 1800  $\text{cm}^{-1}$ , with a spectral resolution of 8  $\text{cm}^{-1}$ . This system has recently been described in detail.<sup>56</sup>

Unstained cryosections (25  $\mu\text{m}$ ) of glioblastoma tissue were placed on an xyz- motorized, computer controlled sample stage (Leica DM STC, Cambridge, UK), which enabled automatic scanning of the sample. The laser light was focused below the surface of the tissue at such a depth that the signal intensity was maximized. The area to be scanned and the scanning step size were chosen, therefore dividing up the area of interest into small square areas (here termed Raman pixel). Spectra were obtained consecutively from the tissue in each of these Raman pixels, the size of which varied between 0.25 and 400  $\mu\text{m}^2$ , for different measurements. The x80 microscope objective focused the laser light to a spot of less than 1  $\mu\text{m}^2$ . Therefore, to obtain a spectrum that is representative for the tissue in a Raman pixel, the area of the Raman pixel was scanned during each spectral measurement. Acquisition of Raman spectra and microscopic stage movement was controlled by the WiRE 1.2 software (Renishaw) running under Grams/32 Spectral Notebase Software (Galactic Industries Corp., Salem, USA). Raman mapping software was implemented in Array Basic (the internal software platform of Grams) and controlled the Leica microscope unit and the microscope stage.

Tissue samples were excited with 90 to 110 mW of laser power during Raman experiments. Spectra were usually obtained using 10 s of signal collection time per Raman pixel.

## Data Analysis

The Raman data were analyzed with software developed in-house that operates in the Matlab environment (The MathWorks, Inc., Natick, MA, USA) using the multivariate statistical analysis toolbox PLS-toolbox 2.0.0c (Eigenvector Research, Inc., Manson, WA).

### *Pretreatment of Spectra*

Following acquisition, the spectra were first calibrated using Raman calibration standards as described earlier.<sup>29</sup> The reference spectrum of a tungsten-band lamp of known temperature was used to correct for the wavelength-dependent signal detection efficiency of the Raman setup. Spectral pre treatment also involved the subtraction of interfering background Raman signal originating in the optical elements in the laser light delivery pathway and the CaF<sub>2</sub> slide.

### *Raman Maps*

Raman maps were constructed from the spectral data set using multivariate statistical techniques. To minimize the influence of any slowly varying fluorescence or background scatter in the spectra which is non informative, the first derivative of the spectra was taken (using the Savitzky-Golay method). The resulting spectra were subsequently scaled so that all the derivative spectra of a map had zero mean and unit standard deviation (auto-scaling or standard normal variate scaling).<sup>29</sup>

PCA was used to orthogonalize and reduce the number of parameters needed to represent the variance in the spectral data set.<sup>57</sup> Cluster analysis was then used to find groups of spectra that have resembling spectral characteristics. PCA scores accounting for 99.9% of the variance captured served as input for KCA. KCA was performed because it can easily handle large amounts of data as obtained during Raman mapping experiments.<sup>58</sup> The algorithm was initiated by allowing the user to choose the number of clusters. The criteria used to determine the number of clusters to be included in the analysis were that the final cluster-averaged spectra displayed meaningful spectral differences (i.e., above noise level) and that the clusters could be related to histologically distinct areas in the tissue sections (see section below on pseudocolor Raman maps). The initial values for the centers of these clusters were taken randomly from the spectral data set. All spectra in the data set were then compared to these cluster centers and assigned to the center that they most resemble. After assigning all spectra to one of the clusters, the new cluster center was calculated by taking the mean of all the spectra that were assigned to that cluster. This procedure was repeated until a stable solution was reached. The cluster-membership information was plotted as a pseudocolor map by assigning a color to each different cluster.

### *Raman Maps and Histopathology*

The location of each differently colored area in the pseudocolor Raman maps was compared with the histopathology. Depending on whether different colors corresponded with vital or necrotic regions within HE-stained section, each cluster was labeled “vital” or “necrotic”, irrespective of the Raman spectroscopic results.

### *Raman Difference Spectra*

Information about differences in biochemical composition of the various structures can be extracted from “positive” difference spectra, which are calculated by scaled subtraction of the cluster averages from each other. In short: for two given spectra, N and V, a difference spectrum N-V is calculated, where V is scaled in such a way that the difference spectrum does not show negative Raman features. The resulting difference spectrum gives a good impression of which molecular species are present in a relatively higher amount in spectrum N than in spectrum V.

### *Linear Discriminant Analysis (LDA) Modeling*

Based on the histopathological cluster assignment, a LDA model was built. LDA is a supervised modeling technique that finds the best linear combination of variables to discriminate between the two groups.<sup>59</sup> For this purpose, a database consisting of cluster-averaged spectra was created. Before averaging the spectra were first pretreated as described above (Savitzky-Golay differentiation method and auto-scaling). Then PCA was performed on this data set to obtain a representation of the spectra in a reduced number of orthogonal variables. To prevent overfitting in the LDA model, the number of PCs used in the model should be at least two times smaller than the number of spectra in the smallest model group. Therefore only those PCs that show high significance in discriminating necrosis from vital glioma, were individually selected by employing two-sided *t* test.

The internal consistency of the LDA model data set was evaluated with leave-one-out testing. In this test, the classification of each single cluster average is predicted using an LDA model that is built on all model cluster averages minus the cluster average to be predicted.<sup>60</sup> The prediction accuracy of the LDA model was tested by predicting whether cluster averages from independent samples (i.e., not used for the model database) originated from vital or necrotic tumor parts.

## **Results**

Twenty-four Raman mapping experiments were performed on unstained, unfixed cryosections of 20 glioblastoma tissue samples taken from 20 patients. The maps varied in size from 200 pixels (in a few cases, in which small structures within a section were mapped at high resolution) to 13,000 pixels (for larger areas in tissue sections, containing both vital and necrotic tissue). Regions within the unstained tissue sections containing vital tumor tissue and necrotic tissue were identified by histopathological evaluation of an HE-stained adjacent tissue section, and selected for Raman scanning. Bright-field microscopic images of such regions in unstained sections are shown in Figures 1A and 1B. Following Raman spectral acquisition, the data were analyzed by principal component analysis (PCA) and

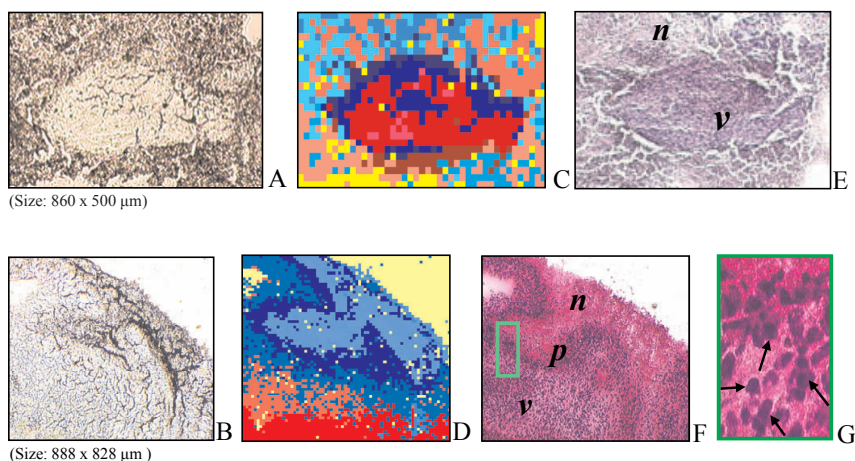


**Figure 1.** **A** and **B**: Photomicrographs (original magnification, x5) of unstained (25  $\mu\text{m}$  thick) human glioblastoma cryosections used in Raman mapping experiments. **C** and **D**: Pseudocolor Raman maps based on the K-means cluster analysis (KCA) of Raman spectra of the tissue sections shown in **A** and **B**. Red: areas of vital tumor tissue, blue: areas of necrosis (see text), yellow: areas in the scan where no tissue was present (edges, freezing artifacts). **E** and **F**: Photomicrographs (original magnification, x5) of the same tissue sections, after HE staining for histological evaluation following Raman measurements (vital tissue designated with **v** and necrotic with **n**). Typical necrosis surrounded by pseudopalisading tumor cells is present in **F** (marked with **p**). **G**: x40 magnification of detail marked with a green frame in **F**; in between the pseudopalisading cells disintegrating tumor cells are visible (arrows).

K-means cluster analysis (KCA). Each cluster (consisting of similar spectra) was assigned a color. Pseudocolor Raman maps were then created in which the color of each pixel is determined by the cluster membership of the spectrum obtained from that pixel. Representative examples of Raman pseudocolor maps are shown in Figures 1C and 1D. Since in KCA the user determines the number of clusters, a protocol was adopted in which for each tissue section several KCA were carried out with increasing number of clusters, as long as this resulted in clusters containing biochemical information (see Materials and Methods). This ensured that the resulting clusters captured all essential signal variance. In this way KCA of the spectra obtained from the first 11 glioblastoma samples resulted in a total of 72 clusters (the number of clusters per sample ranging from 4 to 11). After the acquisition of the Raman spectra, the tissue sections were HE stained (Figures 1E and 1F). This enabled a histological evaluation of the different clusters in the Raman maps, which showed that Raman clusters correspond to either necrotic areas (the weaker stained areas, marked “n” in Figures 1E and 1F) or vital tumor areas (the more intensely stained areas, marked “v”). A large number of clusters imply that significant biochemical variation is present within necrotic tissue areas and within vital tissue. An clear illustration of this is given by Figures 1D and 1F, which show a large necrotic region surrounded by an area of closely packed cells referred to as pseudopalisading (marked “p”). In between the palisading cells, numerous disintegrating

(necrotic) cells are also present, as shown in Figure 1G (arrows). In the pseudocolor maps 1C and 1D, shades of red were used to locate areas (and variance in biochemical composition) of vital tumor tissue. Likewise, shades of blue were used for necrosis. Figure 2 shows representative spectra of different areas of vital tumor tissue (spectra A, B and C), which serve to illustrate the spectral variance encountered in vital tumor tissue. The difference spectrum 2D (2A minus 2C) shows clear overlap with Raman spectra of pure glycogen (2E and open bars) and fatty acids (2F and gray bars). Similarly, representative spectra (spectra A, B and C) of necrotic areas are shown in Figure 3. The difference spectrum (3A minus 3C) is shown in Figure 3D and spectral regions of most prominent signal contributions from cholesterol (3E and open bars) and calcium hydroxyapatite (3F and gray bars) are highlighted. Based on the histopathological evaluation, a total of 36 clusters were labeled as “necrotic” and 36 as “vital”. For each cluster a cluster-averaged spectrum was calculated and used to develop a linear discriminant analysis (LDA) model for discrimination between necrosis and vital tumor tissue (see Materials and Methods). PCA was applied to obtain a reduced number of orthogonal variables for this LDA model data set.

The significance of each principal component (PC) in discriminating between the two tissue classes (vital versus necrotic glioblastoma tissue) was calculated using a two-sided t-test. These values are listed in Table 1. As can be seen, the two PCs that exhibit the highest significance are PCs 2 and 22. The scores of the cluster-averaged spectra on these two PCs

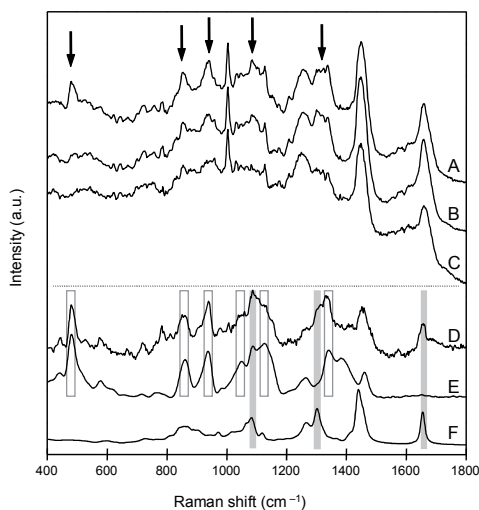


**Figure 2. A to C:** Representative cluster-averaged Raman spectra collected from vital glioblastoma. These spectra are representative of the signal variance encountered within vital tumor areas of the tissue section shown in Figure 1. Arrows indicate spectral regions with clear signal variance, (a. u.= arbitrary units). **D:** Difference spectrum 2A minus 2C. **E:** Raman spectrum of pure glycogen. **F:** Raman spectrum of fatty acid (oleic acid). Open bars (glycogen) and gray bars (fatty acid) have been used to highlight areas of significant spectral overlap between these compounds and the difference spectrum 2D.

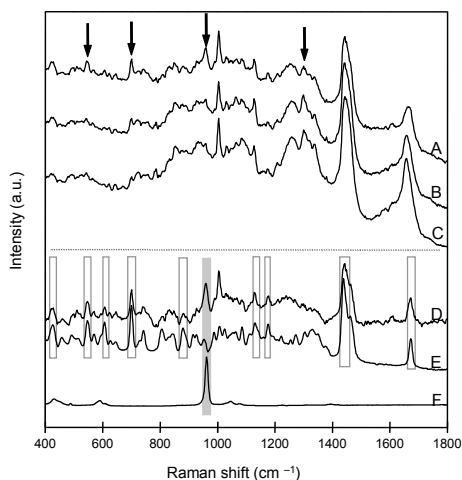


**Figure 3.** **A to C:** Raman spectra obtained from different necrotic parts within the tissue section shown in Figure 1. Spectral regions with clear signal variance are marked with arrows, (a.u.= arbitrary units). **D:** Difference spectrum A minus C. **E:** Raman spectrum of pure cholesterol. **F:** Raman spectrum of calcium hydroxyapatite. The regions of most striking resemblance between difference spectrum (D) and spectra of pure cholesterol (E, open bars) and calcium hydroxyapatite (F, gray bars) are highlighted.

**Table 1.** Significance of the First 22 Principal Components for Discrimination between Vital and Necrotic Glioblastoma Tissue as Determined by a Two-Sided *t*-Test.

PC number	Significance
1	0.79
2	1.00
3	0.78
4	0.62
5	0.55
6	0.62
7	0.82
8	0.55
9	0.69
10	0.72
11	0.50
12	0.52
13	0.79
14	0.67
15	0.65
16	0.62
17	0.53
18	0.58
19	0.87
20	0.52
21	0.62
22	0.91

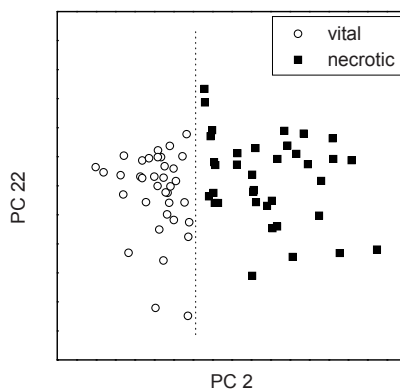


**Figure 4.** Score plot of the cluster-averaged spectra on the two most significant principal components (PCs), PC 2 and 22. The figure clearly shows that the two groups of tissue spectra (vital vs necrotic glioblastoma) can be separated using only PC 2, and that PC 22 does not add significant discriminatory information.

are shown in Figure 4. The figure clearly shows that the two groups of tissue spectra can be separated using only PC 2, and that PC 22 does not add significant discriminatory information.

To minimize the risk of overfitting the data on which the LDA model was developed, only the scores on PC 2 were used as input for the model. This PC represents 17.44% of the total signal variance present in the data set. A leave-one-out cross-validation of this LDA model resulted in an accuracy of 100%.

The LDA model was tested, using an independent data set collected from the next 13 Raman mapping experiments (on tissue sections of 9 patients, not included in the model training set). KCA was performed in the same way as before for the model data set, resulting in a total of 70 clusters. Pseudocolor maps were again compared with histopathology. This resulted in 42 clusters being labeled “vital” and 28 “necrotic”. Cluster-averaged spectra were calculated for all clusters and the LDA model was then used to predict whether these spectra were obtained of vital or necrotic tissue and the results were compared to histopathological classification. A 100% correspondence was found.

To visualize the distribution of vital and necrotic tissue as predicted by the LDA model, Raman-prediction maps were generated by applying the LDA model to each individual spectrum (pixel) of the map. Examples of prediction maps are shown in Figures 5C and 5D. A comparison with the histopathological evaluation of the HE-stained sections (5E, 5F) serves to illustrate the accuracy of the LDA model.

Raman spectra of necrotic and viable glioblastoma (which are averaged over all necrotic clusters and all vital clusters respectively in the LDA model set), are shown in Figure 6 (spectra A and B). A difference spectrum (necrosis minus vital tumor) is displayed in 6C. It closely resembles spectra of pure cholesterol and cholesterol esters such as cholesterol

**Figure 5, following page. A and B:** Photomicrographs (original magnification, x5) of unstained (25  $\mu\text{m}$  thick) human glioblastoma cryosections before Raman spectroscopic mapping. **C and D:** Linear discriminant analysis (LDA) model prediction maps. The spectra obtained from each pixel were used as input for the vital vs. necrosis prediction model. Red: vital, blue: necrosis. **E and F:** Photomicrographs (original magnification, x5) of the same frozen sections after HE staining for histological evaluation following Raman measurement (vital designated with **v** and necrotic with **n**). E1 to E3: x40 magnification of details from 5E (frame colors are corresponding), illustrating the changes of tissue structure from vital tumor (E1) to complete necrosis (E3).

oleate and cholesterol linoleate (spectra D, E, and F respectively). The presence of esters in the necrotic glioblastoma tissue can be deduced from the characteristic band at  $1739\text{ cm}^{-1}$ , barely visible in Figure 6A, but clearly present in the difference spectrum (Figure 6C). Other readily interpretable differences are visible near  $1300\text{ cm}^{-1}$  (assigned to  $\text{CH}_2$  twist and wagging vibrations),  $1131\text{ cm}^{-1}$  (C-C stretching),  $1086\text{ cm}^{-1}$  (C-C stretching and  $\text{PO}_2^-$  symmetric stretching) and  $1063\text{ cm}^{-1}$  (C-O stretching and C-O-C symmetric stretching).<sup>15,33</sup> These bands are assigned to fatty acids and phospholipids. The difference spectrum also shows small features at  $1523$  and  $1159\text{ cm}^{-1}$ , which resemble carotenoids and an intense band at  $958\text{ cm}^{-1}$  probably due to calcifications.<sup>33</sup>

Crystal-like inclusions were frequently observed in necrotic regions during standard microscopic examination of unstained tissue. An example of such an inclusion is shown in Figure 7. The strong spectral overlap between spectrum (Figure 7C) of the inclusion and pure cholesterol spectrum (see Figure 3E) shows that the crystal consists mainly of cholesterol. The presence (and amount) of crystals within necrotic parts of the tumor correlated with the extent of tumor necrosis as it was histopathologically assessed. Furthermore, in necrotic tumor regions in frozen sections from 5 patients, calcification deposits were observed. An example of such a calcification deposit is shown in photomicrograph 8A. The KCA Raman map is shown in Figure 8B. Spectra a and b in Figure 8C show cluster-averaged spectra from the surrounding necrotic tissue ("a") and from the periphery ("b") of the deposit, respectively (see Figure 8B). Spectrum c (cluster average), which was obtained from the center of the inclusion ("c"), shows a very high signal contribution of calcium hydroxyapatite (see Figure 3F).

In six tissue sections from four patients, the Raman spectra obtained from vital glioblastoma indicated the presence of regions with very high glycogen concentrations. A representative spectrum is shown in Figure 9A (see a spectrum of pure glycogen in Figure 2E). A bright-field image and the KCA Raman map are displayed in 9B and 9C, respectively.

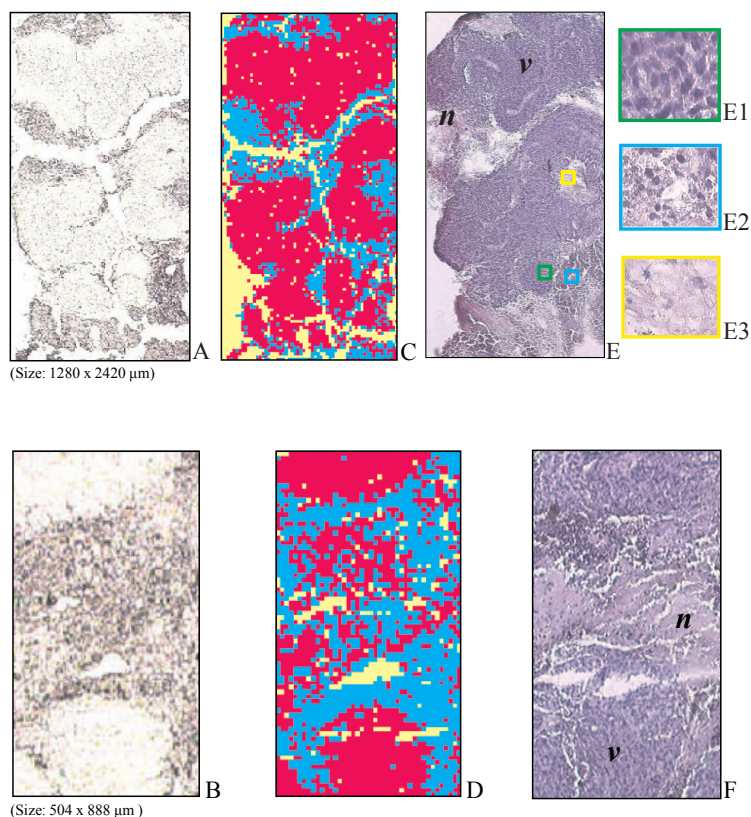


**Figure 5.**

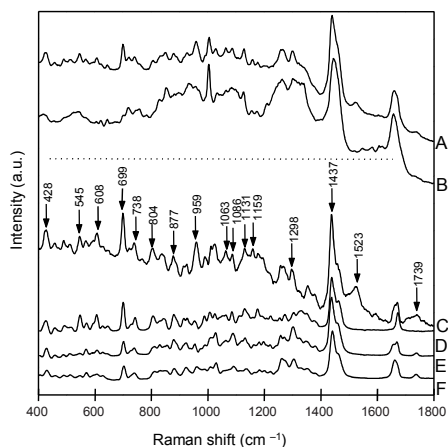


**Figure 6.** Averaged Raman spectra of LDA model set, collected from necrotic (A) and vital glioblastoma parts (B). The difference spectrum (necrotic minus vital) shown in C (intensity multiplied by a factor 2) is compared with the Raman spectra of cholesterol (D), cholesterol oleate (E) and cholesterol linoleate (F). (a.u.= arbitrary units.)

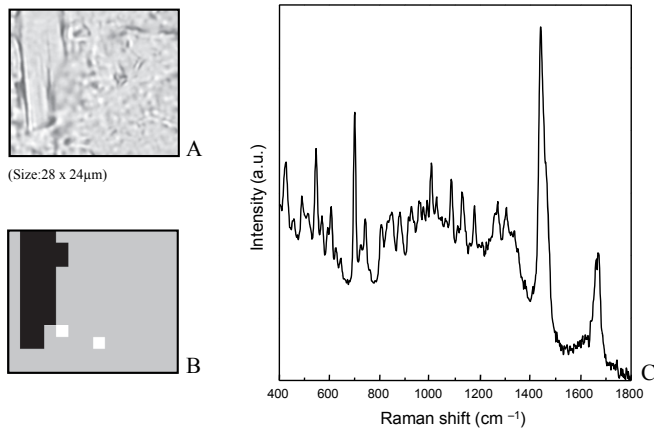


**Figure 7. A:** Photomicrograph of unstained frozen section showing a necrotic area of glioblastoma with a microscopic crystal-like inclusion (original magnification, x80). **B:** Raman map (upon KCA) of the histological detail displayed in A (scanning step size 2 μm). **C:** Raman spectrum (average) of the crystal-like inclusion (predominantly cholesterol, see Figure 3E).

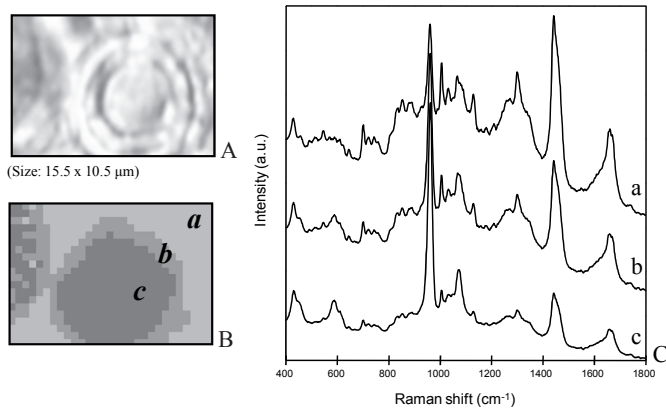


**Figure 8. A:** Bright-field image of calcification deposit in a necrotic glioblastoma region (original magnification, x80). **B:** Raman map, based on the KCA with 3 clusters (scanning step size 0.5 μm). **C:** Raman spectra (averages) of (a) surrounding necrotic tissue, (b) periphery of calcification, and (c) center of calcification (predominantly calcium hydroxyapatite, see Figure 3F).

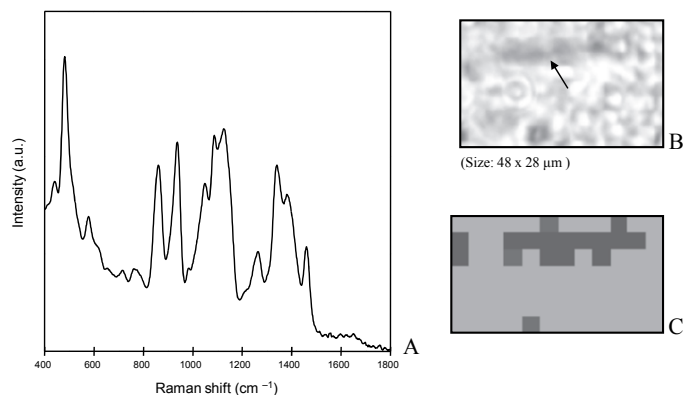


**Figure 9. A:** Raman spectrum (average) collected from area shown in B (arrow). This spectrum shows a strong overlap with Raman spectrum of pure glycogen (see Figure 2E). **B:** Photomicrograph of unstained cryosection showing a histological detail within a vital glioblastoma region (original magnification, x80). **C:** Corresponding KCA Raman map (scanning step size 2 μm).

## Discussion

The results of this study show that the biochemical information represented in Raman spectra enables distinguishing necrotic tissue from viable glioma tissue. The LDA prediction model that was developed for this purpose, in this *in vitro* study with still a relatively low number of samples, had a 100% accuracy. This paves the way for the development of an *in vivo* Raman spectroscopic method for improving intraoperative, real-time brain biopsy guidance. This is important because it will enable the collection of more representative tissue material at stereotactic biopsy than is presently possible thereby improving the classification and grading of glioma.<sup>2,5,34-36</sup> Specimens entirely consisting of necrotic tumor tissue are diagnostically useless. However, in the context of a neoplastic glial proliferation, necrosis is a significant histological feature for classification and grading. Consequently, biopsy target selection by Raman spectroscopy may substantially influence histopathological diagnosis, which is essential for treatment selection and prognosis of gliomas. Although complications following a stereotactic brain biopsy procedure are infrequent, the procedure is not entirely without risk (e.g., hemorrhage or direct trauma) for the patient.<sup>37</sup> Raman guided biopsy will decrease the number of cases in which a second stereotactic biopsy procedure is needed when no representative tumor tissue is obtained the first time.

The utility of intraoperative MRS for targeting during brain biopsy has been reported recently.<sup>14</sup> Raman spectroscopy, like MRS, provides biochemical information about different tissues, but may be more suitable for routine use because it is faster, less complicated and relatively low cost. Thus, the combination of Raman spectroscopy with stereotactic biopsy in addition to existing preoperative imaging techniques (CT\MRI) is particularly attractive.

By correlating Raman spectral maps with histopathology of the same tissue sections, we were able to identify the morphological origin that gave rise to the specific spectral features found in this study. Different parts of the tumor had characteristic Raman spectra, enabling the discrimination of vital and necrotic tumor. One of the most pronounced differences separating the spectra of necrotic glioblastoma regions from viable tumor is the increased signal contribution of cholesterol and cholesterol esters in necrotic tissue (Figure 5). Increased levels of cholesterol esters (particularly cholesterol oleate and cholesterol linoleate), in glioma tissue have been reported before.<sup>38-40</sup> In these studies necrotic and vital tumor regions were not separately investigated, and therefore, no specific information regarding the biochemical composition of these distinct tumor regions was obtained. Previous results from studies on brain tumors using proton MRS also provided evidence of mobile lipid resonances<sup>41-43</sup> (resonances arising from fatty acyl chains of lipids), possibly caused by cell proliferation arrest and necrosis. These findings were confirmed by other MRS studies in which the morphological and biochemical features were compared.<sup>44-46</sup> Furthermore, a study of phenotypic changes occurring in rat cell cultures that were conditionally transformed by an activated H-*ras* oncogene, suggested that cellular growth inhibition is accompanied with massive accumulation of neutral lipids, mostly cholesterol esters and triglycerides.<sup>47</sup> The biochemical differences between necrotic and vital glioblastoma as revealed by Raman spectroscopy are in accordance with these results and add information as to the histological origin of these differences. In spectra derived from necrotic parts of glioblastoma, relative higher carotenoid signal contributions were also observed, consistent with previous Raman studies, in which carotenoids were observed in high grade gliomas, but not in normal brain tissue.<sup>33</sup> The current results indicate that carotenoids are mainly present in the necrotic regions of the tumor. Furthermore, an intense band that was attributed to calcification was observed in Raman spectra from necrotic parts of glioblastoma and seems useful in the identification of necrosis within glioblastoma. High levels of glycogen in glioma were reported in a number of studies.<sup>48-50</sup> The presence of polysaccharides in human glioma tissue was also described by a previous Raman spectroscopic study.<sup>33</sup> Raman spectroscopy can be applied *in vivo* using special fiber-optic probes optimized for the size and location of the actual measurement volume of the tissue.<sup>51-54</sup> Based on the results presented here and these technological advances, we believe that Raman spectroscopy holds promise for real-time guidance of brain biopsy, for which thin fiber-optic catheters would need to be built into the biopsy needle.<sup>55</sup> The same approach may potentially be of use to distinguish between areas of radiation necrosis and tumor in patients undergoing radiation therapy. Other applications for Raman guided biopsy procedures that can be envisioned include guided biopsy during endoscopy of patients with Barrett's esophagus to better target potential areas of dysplasia,<sup>16</sup> as well as guided fine needle aspiration of suspected breast malignancies.

## References

1. Kleihues P (2000). Pathology and genetics of tumours of the nervous system. In: Kleihues P and Cavenee WK, editors. World Health Organization Classification of Tumorous. Lyon: IARCPress.
2. Glantz MJ, Burger P, Herndon J, Friedman A, Cairncross J, Vick N, and Schold S C (1991). Influence of the type of surgery on the histologic diagnosis in patients with anaplastic gliomas. *Neurology* 41:1741-1744.
3. Kros JM (1997). Laboratory diagnosis of brain tumors. In Vecht ChJ, editor. Handbook of Clinical Neurology (Neuro-Oncology, part I), 23:217-233.
4. Sawin PD, Hitchon PW, Follet KA, and Torner JC (1998). Computed imaging-assisted stereotactic brain biopsy: A risk analysis of 225 consecutive cases. *Surg Neurol* 49:640-649.
5. Bullard DE, Osborne D, Burger PC, and Nashold BS (1986). Further experience utilizing the Gildenberg technique for computed tomography-guided stereotactic biopsies. *Neurosurg* 19:386-391.
6. Hildebrand J, Dewitte O, Dietrich PY, and de Tribolet N (1997). Management of malignant brain tumors. *Eur Neurol* 38:238-253.
7. Dowling C, Bollen AW, Noworolski SM, McDermott MW, Barbaro NM, Day MR, Henry RG, Chang SM, Dillon WP, Nelson SJ, and Vigneron DB (2001). Preoperative proton MR spectroscopic imaging of brain tumors: correlation with histopathologic analysis of resection specimens. *Am J Neuroradiol* 22: 604-612.
8. Fountas KN, Kapsalaki EZ, Gotsis SD, Kapsalakis JZ, Smisson HF, Johnston KW, Robinson JS, and Papadakis N (2000). In vivo Proton Magnetic Resonance Spectroscopy of brain tumor. *Stereotact Funct Neurosurg* 74:83-94.
9. Hall WA, Lui H, Truwit CL, and Martin AJ (1999). Comparison of stereotactic brain biopsy to interventional Magnetic-Resonance-Imaging-guided brain biopsy. *Stereotact Funct Neurosurg* 73:148-153.
10. Kurhanewicz J, Vigneron DB, and Nelson SJ (2000). Three-dimensional Magnetic Resonance Spectroscopic Imaging of brain and prostate cancer. *Neoplasia* 2:166-189.
11. Nelson SJ, Vigneron DB, and Dillon WP (1999). Serial evaluation of patients with brain tumors using volume MRI and 3D  $^1\text{H}$  MRSI. *NMR Biomed* 12:123-138. Nygren C, von Holst H, Månsson J-E, and Fredman P (1997). Increased levels of cholesterol esters in glioma tissue and surrounding areas of human brain. *Br J Neurosurg* 11:216-220.
12. Pirzkall A, McKnight TR, Graves EE, Carol MP, Sneed PK, Wara WW, Nelson SJ, Verhey LJ, Larson DA (2001). MR-spectroscopy guided target delineation for high-grade gliomas. *Int J Radiat Oncol Biol Phys.* 50: 915-928.
13. Vigneron D, Bollen A, McDermott M, Wald I, Day M, Moyher-Noworolski S, Henry R, Chang S, Berger M, Dillon W, and Nelson S. Three-dimensional magnetic resonance spectroscopic imaging of histologically confirmed brain tumors. *Magn Reson Imaging* 2001; 19:89-101.
14. Hall WA, Martin AJ, Lui H, and Truwit CL (2001). Improving diagnostic yield in brain biopsy: coupling spectroscopic targeting with real-time needle placement. *Journal of Magnetic Resonance imaging* 13:12-15.
15. Tu AT (1982). Basic concept and elementary theory: Raman spectroscopy in biology. New York: John Wiley & Sons.
16. Bakker Schut TC, Witjes M, Sterenborg M, Speelman O, Roodenburg J, Marple E, Bruining H, and Puppels GJ (2000). In vivo detection of dysplastic tissue by Raman spectroscopy. *Anal Chem* 72:6010-6018.

17. Boustany NN, Crawford JM, Manoharan R, Dasari RR, and Feld MS (1999). Analysis of nucleotides and aromatic amino acids in normal and neoplastic colon mucosa by ultraviolet resonance Raman spectroscopy. *Lab Invest* 79:1201-1214.
18. Buschman R, Marple ET, Wach ML, Bennett B, Bakker Schut TC, Bruining HA, Bruschke AV, van der Laarse A, and Puppels GP (2000). In vivo determination of the molecular composition of artery wall by intravascular Raman spectroscopy. *Anal Chem* 72:3771-3775.
19. Frank CJ, McCreery RL, and Redd DC (1995). Raman spectroscopy of normal and diseased human breast tissues. *Anal Chem* 67:777-83.
20. Hanlon EB, Manorahan R, Koo TW, Shafer KE, Motz JT, Fitzmaurice M, Kramer LR, Itzakan I, Dasari RR, and Feld MS (2000). Prospects for in vivo Raman spectroscopy. *Phys Med Biol* 45:R1-R59.
21. Mahadevan-Jansen A, Mitchell MF, Ramanujam N, Malpica A, Thomasen S, Utzinger U, and Richards-Kortum R (1998a). Near-infrared Raman spectroscopy for in vitro detection of cervical precancers. *Photochem Photobiol* 68:123-132.
22. Mahadevan-Jansen A, Mitchell MF, Ramanujam N, Malpica A, Utzinger U, and Richards-Kortum R (1998b). Development of a fiber optic probe to measure NIR Raman spectra of cervical tissue in vivo. *Photochem Photobiol* 68:427-431.
23. Mahadevan-Jansen A and Richards-Kortum R (1996). Raman spectroscopy for the detection of cancers and precancers. *J Biomed Opt* 1:31-70.
24. Manoharan R, Wang Y, Dasari RR, Singer SS, Rava RP, and Feld MS (1994). Ultraviolet resonance Raman spectroscopy for detection of colon cancer. *Lasers Life Sci* 6:1-11.
25. Manoharan R, Wang Y, and Feld MS (1996). Histochemical analysis of biological tissues using Raman spectroscopy. *Spectrochimica Acta Part A* 52:215-249.
26. Manoharan R, Schafer K, Perelman L, Wu J, Chen K, Deinum G, Fitzmaurice M, Myles J, Crowe J, Dasari RR, and Feld MS (1998). Raman spectroscopy and fluorescence photon migration for breast cancer diagnosis imaging. *Photochem Photobiol* 67:15-22.
27. Shim MG, Song LM, Marcon NE, and Wilson BC (2000). In vivo near-infrared Raman spectroscopy: demonstration of feasibility during clinical gastrointestinal endoscopy. *Photochem Photobiol* 72:3771-3775.
28. Stone N, Stavroulaki P, Kendall C, Birchall M, and Barr H (2000). Raman spectroscopy for early detection of laryngeal malignancy: preliminary results. *Laryngoscope* 110:1756-1763.
29. Wolthuis R, Bakker Schut TC, Caspers PJ, Buschman HP, Römer TJ, Bruining HA, and Puppels GJ. Raman spectroscopy methods for in vitro and in vivo tissue characterization. In: Mason WT, editor. *Fluorescent and luminescent probes for biological activity*. San Diego: Academic Press 1999; pp 433-455.
30. Mizuno A, Hayashi T, Tashibu K, Maraishi S, Kawauchi K and, Ozaki Y (1992). Near-infrared FT-Raman spectra of the rat brain tissues. *Neuroscience letters* 141:47-52.
31. Ong CW, Shen ZX, He Y, Lee T, and Tang SH (1998). Raman microspectroscopy of the brain tissues in the substantia nigra and MPTP-induced Parkinson's disease. *J Raman Spectrosc* 30:91-96.
32. Wolthuis R, van Aken M, Fountas K, Robinson JS, Bruining HA, and GJ Puppels (2001). Determination of water concentration in brain tissue by Raman spectroscopy. *Anal Chem* 73:3915-3920.
33. Mizuno A, Kitajima H, Kawauchi K, Muraishi S, and Ozaki Y (1994). Near-Infrared Transform Raman spectroscopic study of human brain tissues and tumors. *J Raman Spect* 25:25-29.
34. Kleihues P, Volk B, Anagnostopoulos J, and Kiessling M (1984). Morphologic evaluation of stereotactic brain tumor biopsies. *Acta Neurochirurgica* 33:171-181.
35. Paulus W and Peiffer J (1989). Intratumoral histologic heterogeneity of gliomas. *Cancer* 64:442-447.

36. Scerrati M and Rossi GF (1984). The reliability of stereotactic biopsy. *Acta Neurochirurgica* 33:201-205.
37. Field M, Witham TF, Flickinger JC, Kondziolka D, and Lunsford LD (2001). Comprehensive assessment of hemorrhage risks and outcomes after stereotactic brain biopsy. *J Neurosurg* 94:545-51.
38. Campanella R (1992). Membrane lipids modifications in human gliomas of different degree of malignancy. *J Neurosurg Sci* 36:11-25.
39. Gopal K, Grassi E, Paoletti P, and Usardi M (1963). Lipid composition of human intracranial tumors: a biochemical study. *Acta Neurochir (Wien)* 11:333.
40. Nygren C, von Holst H, Månsson J-E, and Fredman P (1997). Increased levels of cholesterol esters in glioma tissue and surrounding areas of human brain. *Br J Neurosurg* 11:216-220.
41. Barba I, Cabañas ME, and Arús C (1999). The relationship between Nuclear Magnetic Resonance-visible lipids, lipid droplets, and cell proliferation in cultured C6 cells. *Cancer Res* 59:1861-1868.
42. Nagedank WG, Sauter R, Brown TR, Evelhoch JL, Falini A, Gotsis ED, Heerschap A, Kamada K, Lee BC, Mingeot MM, Moser E, Padavic-Shaller KA, Sanders JA, Spraggins TA, Stillman AE, Terwey B, Vogl TJ, Wicklow K, and Zimmerman RA (1996). Proton magnetic resonance spectroscopy in patients with glial tumors: a multicenter study. *J Neurosurg* 84:449-458.
43. Rémy C, Fouilhé, Barba I, Sam-Laï E, Lahrech H, Cucurella M-G, Izquierdo M, Moreno A, Ziegler A, Massarelli R, Décorps M, and Arús C (1997). Evidence that mobile lipids detected in rat brain glioma by <sup>1</sup>H nuclear magnetic resonance correspond to lipid droplets. *Cancer Res* 57:404-414.
44. Kuesel AC, Briere KM, Halliday W, Sutherland GR, Donnelly SM, and Smith IC (1996). Mobile lipid accumulation in necrotic tissue of high grade astrocytomas. *Anticancer Res* 16:1845-1849.
45. Kuesel AC, Donnelly SM, Halliday W, Sutherland GR, and Smith IC (1994). Mobile lipids and metabolic heterogeneity of brain tumors as detectable by ex vivo <sup>1</sup>H MR spectroscopy (1994). *NMR Biomed* 7:172-180.
46. Kuesel AC, Sutherland GR, Halliday W, and Smith IC (1994). <sup>1</sup>H MRS of high grade astrocytomas: mobile lipid accumulation in necrotic tissue. *NMR Biomed* 7:149-155.
47. Hirakawa T, Maruyama K, Kohl NE, Kodama T, and Ruley EH (1991). Massive accumulation of neutral lipids in cell conditionally transformed by an activated H-ras oncogene. *Oncogene* 6:289-295.
48. Galarraga J, Loreck DJ, Graham JF, DeLaPaz RL, Smith BH, Hallgren D, and Cummins CJ (1986). Glucose metabolism in human gliomas: correspondence of in situ and in vitro metabolic rates and altered energy metabolism. *Metab Brain Dis* 1:279-291.
49. Keller K, Lange K, and Noske W (1981). D-Glucose transport in cultured cells of neural origin: the membrane as possible control point of glucose utilization. *J Neurochem* 36:1012-1017.
50. Ross BD, Higgins RJ, Boggan JE, Willis JA, Knittel B, and Unger SW (1988). Carbohydrate metabolism of the rat C6 glioma. An in vivo <sup>13</sup>C and in vitro <sup>1</sup>H magnetic resonance spectroscopy study. *NMR Biomed* 1:20-26.
51. Puppels GJ (1999). Confocal Raman spectroscopy. In: Mason WT, editor. *Fluorescent and luminescent probes for biological activity*. London: Academic press, 377-406.
52. Puppels GJ, Bakker Schut TC, Caspers PJ, Wolthuis R, van Aken M, van der Laarse, Bruining HA, Buschman HPJ, Shim MG, and Wilson MC (2001). In vivo Raman spectroscopy. In: Lewis IR and Edwards HGM, editors. *New York: Marcel Dekker*, 549-574.
53. Puppels GJ, van Aken T, Wolthuis R, Caspers PJ, Bakker Schut TC, and Bruining HA (1998). Infrared spectroscopy: New tool in medicine. In: Mantasch HH, Jackson M, and Katzir A, editors. *SPIE conference proceedings*, vol. 3257. Washington, 78-83.

54. Shim MG, Wilson BC, Marple E, and Wach M (1999). Study of fiber-optic probes for in vivo medical Raman spectroscopy. *Appl Spectrosc* 53:619-627.
55. Bohorfoush AG (1996). Tissue spectroscopy for gastrointestinal diseases. *Endoscopy* 28:372-380.
56. van de Poll SWE, Romer TJ, Volger OL, Delsing DJM, Bakker Schut TC, Princen HMG, Jukema JW, Havekes L, van der Laarse A, and Puppels GJ (2001). Raman spectroscopic evaluation of the effects of diet and lipid-lowering therapy on atherosclerotic plaque development in mice. *Arterioscler Thromb Vasc Biol* 21:1630-1635.
57. Jain AK and Dubes RC (1988). Algorithms for clustering data. Prentice Hall: Engelwood Cliffs.
58. Jolliffe IT (1986). Principal component analysis. New York: Springer-Verlag.
59. Tabachnick B and Fidell L (1989). Using Multivariate Statistics, 3th ed. New York: Harper Collins Publishers.
60. Stone M, 1974. Cross-validatory choice and assessment of statistical assessment of statistical predictions (with discussion). *J Royal Stat Soc B* 36:111-147.

# Tissue Characterization Using High Wavenumber Raman Spectroscopy

*Journal of Biomedical Optics*  
2005, 10 (3): 031116, 1-11

5

S. Koljenović  
T.C. Bakker Schut  
R. Wolthuis  
B. de Jong  
L. Santos  
P.J. Caspers  
J.M. Kros  
G.J. Puppels

## Abstract

Raman spectroscopy is a powerful diagnostic tool, enabling tissue identification and classification. Mostly, the so-called fingerprint ( $\sim 400\text{-}1800\text{ cm}^{-1}$ ) spectral region is used. *In vivo* application often requires small flexible fiber-optic probes, and is hindered by the intense Raman signal that is generated in the fused silica core of the fiber. This necessitates filtering of laser light, which is guided to the tissue, and of the scattered light collected from the tissue, leading to complex and expensive designs. Fused silica has no Raman signal in the high wavenumber region ( $2400\text{-}3800\text{ cm}^{-1}$ ). This enables the use of a single unfiltered fiber to guide laser light to the tissue and to collect scattered light in this spectral region. We show, by means of a comparison of *in vitro* Raman microspectroscopic maps of thin tissue sections (brain tumors, bladder), measured both in the high wavenumber region and in the fingerprint region, that essentially the same diagnostic information is obtained in the two wavenumber regions.

This suggests that for many clinical applications the technological hurdle of designing and constructing suitable fiber-optic probes may be eliminated by using the high wavenumber region and a simple piece of standard optical fiber.

## Introduction

Raman spectroscopy is a nondestructive vibrational spectroscopic technique, based on inelastic scattering of light by the molecules in a sample. A Raman spectrum contains detailed information about the molecular composition, molecular structures, and molecular interactions in a tissue.<sup>1</sup> Because different types of tissue differ in their overall molecular composition, their Raman spectra will also be different, and can be used as tissue-specific spectroscopic fingerprints. Pathological changes in a tissue are also accompanied by changes in molecular composition, and are reflected in the tissue spectrum, which enables development of diagnostic tools based on Raman spectroscopy.

An increasing number of Raman studies is providing evidence for the possibility to characterize and identify a large variety of normal tissues, pre-malignant tissues and tumors.<sup>2-10</sup> *In vivo* application of Raman spectroscopy in most cases requires the use of a flexible light guiding device of small diameter, such that it can for instance be introduced in the working channel of an endoscope or inside a biopsy needle or biopsy forceps. The fiber-optic probe must guide light to the tissue under investigation, collect light that is scattered by the tissue, and transport this collected light from the tissue to a spectrum analysis device. Successful steps towards *in vivo* application of the technique, by means of fiber-optic probes have been reported, among others by Mahadevan-Jansen *et al.* who collected *in vivo* spectra from human cervical tissue for the clinical diagnosis of cervical precancers,<sup>8</sup> by Buschman *et al.* who obtained *in vivo* intravascular Raman spectra from arteries,<sup>9</sup> and by Bakker Schut *et al.* who reported on the *in vivo* detection of epithelial dysplasia in rat palate tissue.<sup>10</sup> More recently, the potential of near-infrared Raman spectroscopy using optical fiber probes for diagnosis of lung cancer<sup>11</sup> and for differentiation of colonic polyps during gastrointestinal endoscopy<sup>12</sup> has been demonstrated. Several different miniaturized fiber-optic probes have been designed and realized<sup>13-15</sup> some of which indeed enabled high quality *in vivo* Raman spectra to be obtained.

In all these studies, the spectral region between 400 and 2000  $\text{cm}^{-1}$ , commonly referred to as the “fingerprint region”, was employed. This is a logical choice because this spectral region is very rich in information. Many different molecular vibrations lead to Raman scattering in this part of the spectrum. In many cases bands can be assigned to specific molecular vibrations and or molecular species, much aiding the interpretation of the spectra in terms of biochemical composition of the tissue.

However, the actual implementation of conventional fingerprint Raman spectroscopy for clinical purposes is hampered by the fact that in the 400-2000  $\text{cm}^{-1}$  spectral region, the materials of the optical fiber itself generate Raman signal, resulting in a strong background signal. Unless measures are taken to suppress this fiber Raman signal, it will be more intense than the tissue Raman signal by at least 1 or 2 orders of magnitude. Moreover, bending of the fiber leads to variations in the amount of signal obtained from the core, cladding and

coating materials, which makes it difficult to correct the tissue spectra for this background signal, thereby further complicating signal analysis. For this reason it is necessary to use optical filters at or near the distal end of the fiber-optic probe to suppress these background signal contributions. Examples are the Visionex-probes used by Buschman<sup>9</sup> and Bakker Schut<sup>10</sup> and the probe recently described by Motz *et al.*<sup>13</sup> In these probes one fiber guides laser light to the tissue. This fiber contains a narrow band pass filter at or near the distal end of the fiber which only transmits the laser light but blocks Raman scattered light that has been generated in the fiber. This implies of course that this fiber cannot be used to collect Raman scattered light from the tissue. Therefore the probes comprise multiple signal collection fibers. To avoid generation of Raman scattered light in these fibers, the light, which is collected, is first filtered by a high pass filter, which blocks the laser wavelength.

The combination of requirements for optical filtering leads to complex designs of fiber-optic probes for conventional fingerprint Raman spectroscopy. The complexity makes it difficult to miniaturize fiber-optic probes, which is necessary for instance for intravascular use<sup>9,13</sup> or for intra-cerebral use (i.e., stereotactic brain biopsy) and to ensure reproducible performance.<sup>16</sup> Besides, it is difficult to keep probes flexible, which is of great importance for use in the auxiliary channel of an endoscope.<sup>12</sup> The complexity is also an obstacle to the production of such probes at a price that they can be used as disposables in hospitals. Moreover, signal intensity in the 400-2000  $\text{cm}^{-1}$  is relatively low, which may necessitate long signal integration time making it impractical for clinical use.

It is clear that there is a need for simple and small fiber-optic probes for measuring tissue Raman spectra that circumvent the problems mentioned above.

The solution we are exploring is to use the HWVN region of the Raman spectrum ( $\sim 2400\text{--}3800 \text{ cm}^{-1}$ ). In this spectral region most of the spectral features obtained from tissue are strongly overlapping CH-stretching vibrations in the region  $2800 - 3050 \text{ cm}^{-1}$ ,<sup>1</sup> OH-stretching vibrations (primarily due to water), which appear in the spectral interval  $3100\text{--}3500 \text{ cm}^{-1}$ ,<sup>1</sup> smaller signal contributions of SH-stretching vibrations  $2500 - 2600 \text{ cm}^{-1}$ ,<sup>17</sup> and NH-stretching vibrations between  $3100$  and  $3500 \text{ cm}^{-1}$ .<sup>1</sup> At first glance the information content appears to be in sharp contrast with the information that can be obtained in the fingerprint wavenumber region ( $400\text{--}2000 \text{ cm}^{-1}$ ). Therefore it needs to be established that clinically relevant information can be derived from the high wavenumber (e.g., to distinguish between normal tissue and tumor).

For *in vivo* applications, the use of the HWVN region has a very important practical advantage over the fingerprint region. No Raman signal is generated in fused silica in this wavenumber region. This implies that it should be possible to turn a single unfiltered optical fiber with a fused silica core into an *in vivo* Raman fiber-optic probe, which guides laser light to the tissue and also collects the light that is scattered by the tissue. Added benefits are that the Raman signal in the HWVN region is generally much more intense than the fingerprint

Raman signal and that because of the large Stokes-shift a very simple filter, such as a color glass filter can be used for laser suppression in the signal detection path.

Few studies have reported on the use of HWVN Raman spectroscopy for tissue characterization. Recently, this spectral region was used to determine the water concentration in brain tissue<sup>18</sup> and in skin.<sup>19</sup> Very detailed information about the composition and compositional heterogeneity of atherosclerotic plaque has been obtained recording and analyzing Raman spectral maps of thin tissue cross sections using only the 2400-3800  $\text{cm}^{-1}$  region of its Raman spectrum.<sup>20</sup> Here, we report the results of a number of Raman microspectroscopic mapping experiments on thin tissue sections of brain tumors and bladder tissue to show that in many cases HWVN Raman spectroscopy enables the same level of discrimination between different types of tissue, and provides the same clinically relevant information as Raman spectroscopy in the fingerprint region. In addition, the technical feasibility of obtaining tissue Raman spectra by a single fiber probe is illustrated by measurements on porcine brain tissue, using a simple Raman setup constructed in house.

## Materials and Methods

### Human Tissue Samples

Approval for this study was obtained from the Medical Ethics Review Board of the Erasmus-university Medical Center Rotterdam. The tissue specimens used were from resection material obtained during surgical procedures at the Departments of Neurosurgery, General Surgery, and Urology of the Erasmus MC Rotterdam. An informed consent form was signed preoperatively by each patient after receiving an explanation of study protocol. Tissue samples that were used included two brain malignancies (one glioblastoma, one meningioma) and normal bladder tissue (acquired from two patients, with bladder cancer). After excision, human tissue samples were snap frozen by immersion in liquid nitrogen and stored at  $-80^{\circ}\text{C}$ . For Raman microscopic mapping experiments, these frozen samples were cut into 25  $\mu\text{m}$  thick sections with a microtome at  $-20^{\circ}\text{C}$  and placed onto calcium fluoride ( $\text{CaF}_2$ ) microscope slides. Unfixed tissue sections were dried in ambient air and used without further treatment. In order to confirm whether tissue was normal or tumor and to identify different structures within the tissue specimens, 5- $\mu\text{m}$ -thick adjacent sections were also obtained and stained with hematoxylin and eosin (HE) for histopathological evaluation. Light-microscopic images of the unstained tissue sections revealed heterogeneity in tissue structure, which could be linked to the structural heterogeneity observed in the stained adjacent sections. This assessment was used to select tissue regions for Raman mapping. To provide a direct comparison of the Raman mapping results with histology, the 25- $\mu\text{m}$ -thick tissue sections were HE stained as well, after the Raman mapping measurements were completed.

## Porcine Brain Tissue

Using a single fiber-optic probe *ex vivo* HWVN Raman spectra of larger tissue specimens were obtained. For these experiments brain tissue was used, which was obtained from a 4 months old pig, which was sacrificed after another unrelated terminal medical experiment. The brain was cut at the transversal plane in several 10 - 15 mm thick slices, which were placed in a physiological NaCl solution (i.e., 0.9%). Raman measurements were performed directly, without further pretreatment of the sample.

## Instrumentation

### Raman Microspectroscopic Mapping

Raman spectra of unstained tissue sections were collected using 719 nm and 847 nm laser light from an argon-ion pumped Titanium: Sapphire laser system (Spectra Physics, Mountain View, CA). The Raman microspectrometer that was used in these experiments has been described in detail by van de Poll *et al.*<sup>21</sup>

Briefly, the setup consists of a microscope (DM-RXE, Leica, Cambridge, UK) coupled to a Raman spectrometer (System 100, Renishaw, Wotton under Edge, UK). Laser light was focused on the sample by a 80x NIR optimized microscope objective (Olympus MIR-plan 80x/0.75, Japan) with a working distance of approximately 1.6 mm. Scattered light was collected by the same objective, filtered by a chevron type laser suppression filter and then focused onto the core of an optical fiber, which guides the Raman scattered light into a modified Renishaw system 100 spectrometer. Raman signal was collected in the spectral interval from 400 to 1800  $\text{cm}^{-1}$  and from 2400 to 3800  $\text{cm}^{-1}$ , with a spectral resolution of 8  $\text{cm}^{-1}$  for both wavenumber regions. Unstained cryo-sections (25  $\mu\text{m}$ ) of tissue were placed under the microscope objective on an motorized, computer controlled XYZ-sample stage (Leica DM STC, Cambridge, UK), which enabled automatic scanning of the sample. The laser light was focused below the surface of the tissue at such a depth that the signal intensity was maximized. For each mapping experiment the tissue area to be scanned and the scanning step size were chosen, thereby dividing up the area of interest into small square areas (hereafter termed Raman pixel). Spectra were obtained consecutively from each of these Raman pixels, the size of which varied between 25 (5x5)  $\mu\text{m}^2$  and 900 (30x30)  $\mu\text{m}^2$ , for different measurements. Since the laser spot size is much smaller than the area of the Raman pixels, each pixel was scanned during signal collection, in order to obtain a spectrum that is representative for the tissue in the Raman pixel. The laser power on the tissue samples was about 50 mW in all experiments. Spectra were acquired using 10 seconds of signal collection time per Raman pixel.

Acquisition of Raman spectra and microscopic stage movement was controlled by the WiRE 1.2 software (Renishaw) running under Grams/32 Spectral Notebook Software (Galactic Industries Corp., Salem, NH, USA). Raman mapping software was implemented in Array Basic

(the internal software platform of Grams) and controlled the Leica microscope unit and the microscope stage.

### Raman Fiber-Optic Probe Measurements

*Ex vivo* Raman spectra were obtained by a Raman setup utilizing a single optical fiber to illuminate the tissue and to collect the scattered light from the tissue. For purposes of illustration a Raman spectrum measurement of porcine brain is shown in this manuscript. It was collected using 719 nm laser light of 40mW from an argon-ion pumped Titanium: Sapphire laser (Spectra-Physics, 3900 S) and a signal collection time of 10s. The laser light was coupled into a common optical fiber (with a core diameter of 200 microns and core and cladding consisting of fused silica, 2 m in length, (AS200/220IRAN, FiberTech, Berlin, Germany) at the proximal end. Laser light was guided to the tissue at the distal end of the fiber. Here also scattered light was collected and guided back to the proximal end of the fiber. The wavelength shifted light emerging from the fiber was then reflected off of a dichroic filter (which transmitted the laser wavelength), and guided into a multichannel spectrometer where the HWVN Raman spectrum of the tissue was recorded. The setup has been recently described by Santos *et al.*<sup>22</sup>

### Data Analysis

All Raman data were processed with software developed in-house that operates in the Matlab environment (The MathWorks, Inc., Natick, MA, USA) using the multivariate statistical analysis toolbox PLS-toolbox 2.0.0c (Eigenvector Research, Inc., Manson, WA).

#### *Pretreatment of Spectra*

Following acquisition, all spectra (in vitro and ex vivo) were first calibrated using Raman calibration standards as described earlier.<sup>23</sup> Briefly, two Raman calibration standards with accurately known peak frequencies (4-acetamidophenol (3102.4, 3326.6  $\text{cm}^{-1}$ ), and cyclohexane (2666.4, 2852.9, 29383.3  $\text{cm}^{-1}$ )) and the emission lines of a neon and a neon-argon lamp were used for wavenumber calibration of the spectra. The emission spectrum of a calibrated tungsten band lamp was used to correct recorded Raman spectra for the wavelength-dependent signal detection efficiency of the setup.<sup>23</sup> Spikes due to cosmic ray events were removed from the spectra, and the background signal, from optical elements in the laser light delivery pathway was subtracted from the tissue Raman spectra.

Because almost all spectral signatures from lipids and proteins appear in the 2700 –3100  $\text{cm}^{-1}$  interval, this range was chosen for analysis of the Raman spectra.

#### *Raman Maps*

Raman pseudocolor maps were constructed for each of the tissue sections, based on the spectral data set that was obtained and using multivariate statistical techniques.

To minimize the influence of any slowly varying fluorescence or background scatter in the spectra, which is noninformative, the first derivative of the spectra was taken (using the Savitzky-Golay method). The resulting spectra were subsequently scaled so that all the derivative spectra of a map had zero mean and unit standard deviation (auto-scaling or standard normal variate scaling).<sup>23</sup>

To orthogonalize and reduce the number of parameters needed to represent the signal variance in the spectral data set and to find groups of spectra that have resembling spectral characteristics, Principal component analysis (PCA)<sup>24</sup> and K-means cluster analysis (KCA)<sup>25</sup> were performed, respectively. The PCA scores, accounting for 99,9% of the variance captured, served as input for KCA. KCA was used because it can easily handle the large amounts of data as obtained during Raman mapping experiments. The algorithm was initiated by allowing the user to choose the number of clusters. The criteria used to determine the number of clusters to be included in the analysis were that the final cluster-averaged spectra displayed meaningful spectral differences (i.e., above noise level) and that the clusters could be related to histologically distinct areas at gross microscopic overview of the tissue sections. A Raman spectrum presents the overall molecular composition of the measurement volume in the tissue, because all molecules in the measurement volume contribute to the Raman signal. Spectra that are highly similar, and therefore were obtained of tissue areas of very similar molecular composition, end up in the same clusters. The cluster-membership information was plotted as a pseudocolor map by assigning a color to each different cluster. Depending on the size of the selected area and mapping resolution, the number of pixels per Raman map varied from 1978 to 7744 pixels.

### *Reference Spectra*

Reference Raman spectra were obtained of the following commercially available compounds: glycogen (type II, G-8751, Sigma-Aldrich Chemie, Zwijndrecht, The Netherlands), DNA (D-1501, Sigma, St Louis MO), cholesterol palmitate (150680, ICN Biochemicals Inc., Ohio), cholesterol linoleate (C-0289, Sigma-Aldrich Chemie, Zwijndrecht, The Netherlands), collagen (predominantly type I, 160083, ICN Biochemicals Inc., Ohio), actin, (A-3653, Sigma-Aldrich Chemie, Zwijndrecht, The Netherlands), and triolein (T-7140, Sigma, St Louis MO). These compounds were used without further purification. DNA was dissolved in demineralized water (20mg/ml).

### *Spectral Modeling*

A least-squares fitting procedure was performed to obtain information about the differences in chemical composition between various histological structures. The *in vitro* HWVN Raman spectra of individual histological structures were fitted with spectra obtained from surrounding tissue plus spectra of one or more pure compounds (i.e., glycogen, cholesterol palmitate, DNA, cholesterol linoleate, collagen, actin, and triolein). This (nonrestricted)

fitting procedure resulted in positive or negative fit contributions of the reference spectra that point out higher or lower concentrations of the corresponding compounds in tissue structures that were compared. Relative scattering cross-sections were not determined and therefore all fit contributions are presented as arbitrary units and not as weight percentages.

The presence of noise in the spectra obtained from tissue may influence the fit results. To estimate the uncertainty in the fit results due to noise, artificial (normal distributed) noise was added to the tissue spectra that were fitted. In this way the signal-to-noise ratio of the tissue spectra was artificially decreased by a factor 2. A new set of fit coefficients was calculated according to the last squares fitting procedure described above. This was repeated 100 times for each of the tissue spectra and the standard deviation obtained for each of the fit coefficients served as an estimate for the uncertainty in the fit results.

## Results

### *HWVN Raman Spectra of Pure Compounds*

HWVN Raman spectra from commercially available pure compounds (see Materials and Methods), were obtained. Spectra are presented in Figure 1.

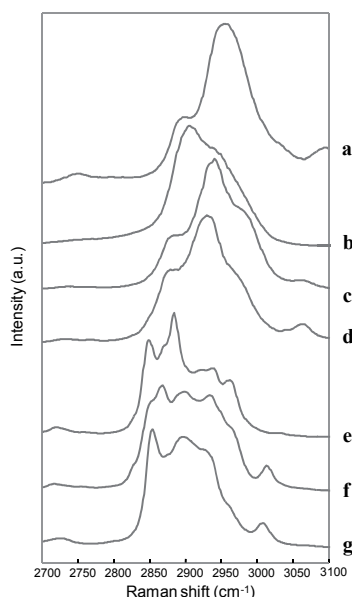


**Figure 1.** HWVN Raman spectra of pure chemical compounds. (a) DNA. (b) Glycogen. (c) Collagen. (d) Actin. (e) Cholesterol palmitate. (f) Cholesterol linoleate. (g) Triolein.

## Raman mapping experiments

### *Glioblastoma*

Glioblastoma is the most malignant brain tumor. The diagnosis is based upon histopathological evaluation of tumor tissue samples, usually obtained by stereotactic surgery. It is essential that representative tissue is sampled, but this is made difficult by the facts that tumor tissue is highly heterogeneous, while stereotactic biopsy samples are relatively small.<sup>26</sup> For example, an important histological parameter for establishing a diagnosis of glioblastoma is the presence of tumor necrosis.<sup>26</sup> When no necrotic tissue is sampled, it leads to underestimation of the tumor grade. On the other hand, histological diagnosis cannot be made when only necrotic tissue is present in the tissue sample.<sup>26</sup> An *in vitro* study has been published describing the potential of Raman spectroscopy for brain biopsy guidance. A classification model, based

**Figure 2, following page.** Comparison of results from Raman experiments on glioblastoma in the fingerprint and HWVN spectral regions. Note: images shown in panels A and B are taken from Koljenović *et al.* (see Ref. 5). Panel **A**: Bright field photomicrograph of the unstained glioblastoma tissue section used for Raman microspectroscopic mapping (original magnification, x5). Panel **B**: Raman map of the tissue section shown in panel A based on measurements in the fingerprint region (400-1900  $\text{cm}^{-1}$ ) and classification of each pixel as necrotic or vital on the basis of a linear discriminant analysis model (see Refe. 5). (pixel size 20 x 20  $\mu\text{m}^2$ , 64 x 121 pixels). Panel **C**: Raman map of the tissue section shown in panel A, based on measurements in the high wavenumber region (2700-3100  $\text{cm}^{-1}$ ) and a K-means cluster analysis of the results (see text). (pixel size 21 x 21  $\mu\text{m}^2$ , 62 x 116 pixels). Note the great correspondence with panel B. Red (cluster 1) indicates vital tumor and blue (cluster 2) indicates necrosis. Note: yellow (cluster 3) represents the areas in the scan where no tissue was present (edges, freezing artifacts). Panel **D**: Result of a least-squares fit analysis of the HWVN vital and necrotic tissue spectra. The average spectrum of vital tumor was fitted with the average spectrum of necrosis and the spectra of pure DNA (see Figure 1) and of pure cholesterol palmitate (see Figure 1). (**a**) Cluster average of vital tumor. (**b**, **c** and **d**) Fit-spectra. (necrosis, DNA and cholesterol palmitate, respectively), which are shown after multiplication by the fit-coefficients that resulted from the least-squares fit. A positive or negative spectrum signifies more or less of that compound is present in vital tumor than in necrosis. (**e**) Fit-residual. (For clarity the spectra have been shifted along the ordinate.) Panels **E** and **F**: Fingerprint and HWVN Raman images demonstrating chemical heterogeneity within vital glioblastoma. These images are based on a KCA performed on the spectra from a small area selected from the larger Raman maps (lower 1/3 of Raman map in panels B and C). Note the division of the “vital cluster” (cluster 1 of panels B and C) in two subclusters (clusters 1 and 2). Cluster 3 is “necrotic cluster”. Panel **G**: Analysis of spectra obtained in the fingerprint region. The average spectrum of the “vital subcluster 1” was fitted with the spectrum of “vital subcluster 2” and the spectrum of pure glycogen. (**a**) Average spectrum of the “vital subcluster 1”. (**b**) Average spectrum of “vital subcluster 2”. (**c**) Spectrum of pure glycogen. (**d**) Fit-residual. (The spectra have been shifted along the ordinate for clarity.) Panel **H**: Analysis of spectra obtained in the HWVN region. (**a** and **b**) Averages of two “vital subclusters”, clusters 1 and 2 of panel F. (**a – b**) Positive difference spectrum of spectra **a** and **b** (a minus b), magnified by a factor of 5 for clarity. (**d**) Spectrum of pure glycogen. (**e**) Fit-residual (resulting from fit of spectrum **a** by spectra **b** and **d**). (For clarity, the spectra have been shifted along the ordinate.)

on spectra obtained in the fingerprint region, for discrimination between vital and necrotic tumor tissue yielded 100% accuracy.<sup>5</sup> In the fingerprint region it was shown that some of the most pronounced differences between vital and necrotic glioblastoma tissue were increased signal contributions of cholesterol and cholesterol esters in necrotic parts and increased levels of glycogen in vital tumor. In the present study these results served as guidance for the analysis of the HWVN spectra of glioblastoma vital and necrotic tissue. Below we show that HWVN spectra can also be used to discriminate between vital and necrotic tumor.

Panel A of figure 2 shows a bright field microscopic image of an unstained thin section of glioblastoma tissue, containing areas of necrosis and areas of vital tumor tissue. Panel B is a Raman map of the tissue section shown in panel A (7744 spectra, lateral resolution 20 $\mu$ m). It was taken from our previous study on human glioblastoma tissue.<sup>5</sup> Red corresponds to vital tumor and blue corresponds to tumor necrosis (yellow represents the areas where no

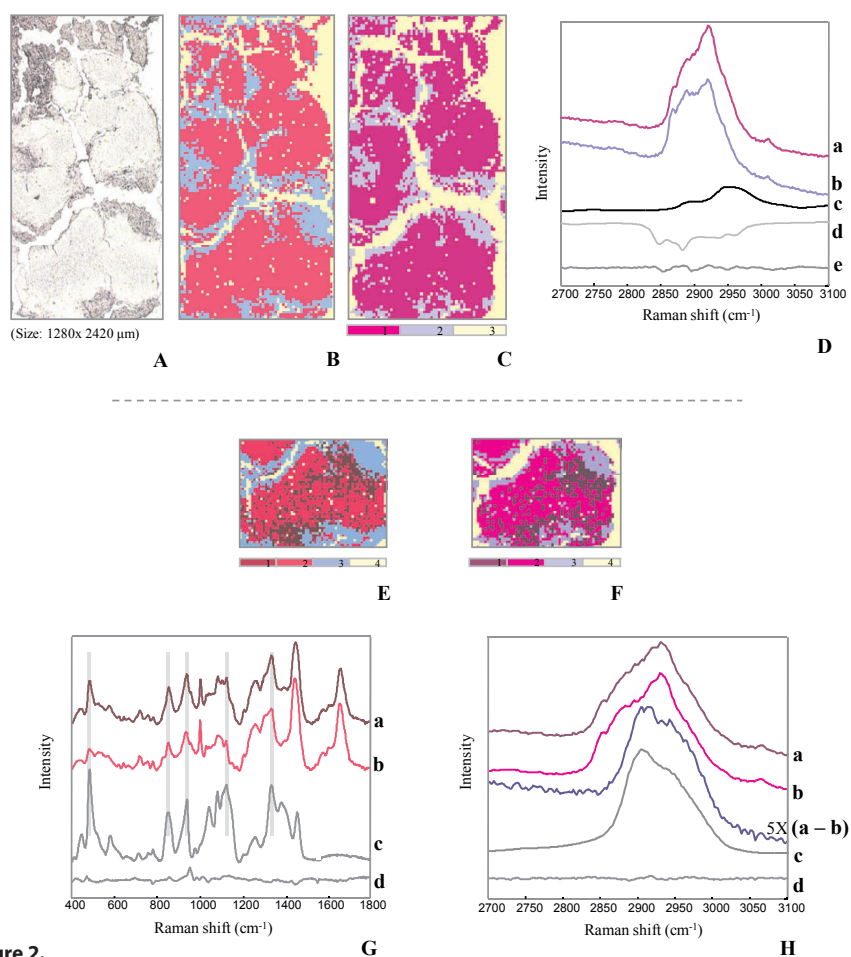


**Figure 2.**

tissue is present). The map is based on a linear discriminant model developed on the basis of an extensive database of Raman spectra of vital glioblastoma tissue and of necrotic tissue, obtained in the 400-1800  $\text{cm}^{-1}$  spectral region.<sup>5</sup> Panel C shows a Raman map of the same tissue section, but in this case based on a 3-cluster KCA of Raman spectra obtained in the 2700-3100  $\text{cm}^{-1}$  spectral region (7192 spectra, lateral resolution 21  $\mu\text{m}$ ). It is clear that a strong correlation exists between the necrotic and vital tissue areas identified in panel B and the result of the cluster analysis of the spectra obtained in the HWVN region. In HWVN Raman map (panel C) cluster 1 corresponds with vital tumor and cluster 2 with necrosis.

There are clearly significant differences between the cluster-averaged HWVN Raman spectra (Figure 2, panel D). These spectral differences, pointing out a difference in chemical composition of vital and necrotic tumor tissue, were analyzed by a least-squares fit procedure. The average spectrum of the "vital cluster" [spectrum (a)] was fitted with a set of spectra consisting of the average of the "necrotic cluster" [spectrum (b)], and of the reference spectra obtained from DNA [see Figure 1, spectrum (a)] and cholesterol palmitate [see Figure 1, spectrum (e)]. In panel D, the fit-spectra of pure compounds (i.e., DNA and cholesterol palmitate) are shown after multiplication by the fit-coefficients that resulted from the least-squares fit [spectra (c) and (d)]. Therefore a positive or negative spectrum signifies that more or less of that compound is present in viable tumor than in necrotic tissue. The choice for these fit spectra was based on a first assessment of the shape of the difference spectrum between vital and necrotic tissue (not shown), on our earlier finding of higher cholesterol and cholesterol ester content of necrotic tissue<sup>5</sup> and on the disintegration of nuclei in necrotic tissue which can be expected to lead to lower DNA content. The small fit-residual (e) suggests that this choice of fit spectra was justified. The fit results show that vital glioblastoma tissue has relatively stronger signal contributions from DNA but weaker signal from cholesterol esters (apparently cholesterol palmitate) when compared with necrotic tissue, in accordance with expectations.

Panels E and F show the result of a four-cluster KCA based on fingerprint spectra and HWVN Raman spectra respectively, for the bottom part of the tissue section shown in panels A to C. The result is a subdivision of the vital tumor tissue into 2 clusters, which is a sign of heterogeneity in terms of molecular composition within the vital tumor, and which is very similar in both panels. Panel G shows the average spectra of clusters 1 [spectrum (a)] and 2 [spectrum (b)] of panel E and the spectrum of glycogen [spectrum (c)]. Comparison of these spectra makes clear that glycogen signal contributions (highlighted with gray bars) are much more prominent in spectrum (a). A multiple least-squares fit of spectrum (a) with spectra (b) and (c) resulted in the small fit-residual shown by line (d). This makes clear that indeed the difference in glycogen content between the two vital tumor areas is the most prominent difference in molecular composition, although the presence of small spectral features in the fit-residual does also point to other minor differences.

Panel H suggests that the biochemical ground for the KCA result based on HWVN spectra is the same. Average spectra of two "vital clusters" from panel F are shown; spectrum (a) is the

average spectrum of cluster 1, spectrum (b) the average spectrum of cluster 2. Spectrum (c) is their difference spectrum, shown 5 times enlarged, and calculated in such a way that only positive difference features are present. A comparison of this rather featureless spectrum with the spectrum of glycogen [spectrum (d)] shows great similarity. Spectrum (e) is the residual of a multiple least-squares fit of spectrum (a) with spectrum (b) and the glycogen spectrum. The fact that it is virtually a straight line suggests that also in the HWVN spectra it is the difference in glycogen signal intensity which separates the two vital tumor areas, although its spectral features are much less characteristic than in the fingerprint region.

The influence of noise, present in the tissue spectra, on the fit results was investigated for all of the fits presented above. Shot noise was artificially added to the average spectra of both the "vital cluster" and "necrotic cluster" [spectra (a) and (b) in panel D] and the averages of both the "vital clusters" from panels E and F [spectra (a) and (b) in panels G and H]. A new set of fit-coefficients was calculated (see Materials and Methods), which showed that spectral noise had very little influence on the fit results, indicating that it is of no consequence to the conclusions drawn on the basis of the fits (for the fit result presented in panel D calculated errors were:  $\sim 1\%$  for the average of "necrotic cluster",  $\sim 5\%$  for DNA %, and  $\sim 6\%$  for cholesterol palmitate; for both the fits shown in panels G and H errors were:  $\sim 1\%$  for the average of "vital cluster" 2 and  $\sim 8\%$  for glycogen).

### *Meningioma*

Meningiomas are the most common benign tumors of central nervous system. They are rounded and usually attached to the dura. Although predominantly benign, these brain tumors often recur even after apparently complete resection.<sup>27</sup> Unfortunately, there are no per-operative tools to make sure whether or not all tumor tissue has been removed. The real extent of failure is therefore unknown until the tumor has grown significantly. *In vivo* HWVN Raman spectroscopic identification of tumor cells attached to dura may be able to facilitate total tumor resection, resulting in decreased meningioma recurrence rates.

Figure 3 shows the results of a Raman mapping experiment on a thin section of human meningioma, microcystic type, attached to dura. Raman spectra were obtained in both the fingerprint region (6200 spectra) and the HWVN region (6477 spectra), using a  $30\text{ }\mu\text{m}$  lateral resolution. The area within the unstained tissue section that was selected for Raman mapping is shown in the bright field image in panel A. The fingerprint Raman image (panel B) and the HWVN Raman image (panel C), based on a four-clusters KCA are shown. The HWVN Raman image is virtually identical to the fingerprint Raman image, which indicates that the same clinical information can be obtained in both wavenumber regions. Comparison of these pseudocolor maps with the image of the tissue section after HE staining (panel D) enabled identification of cluster 1 as dura (labeled "d" in panel D) and clusters 2 and 3 as meningioma (labeled "m" in panel D). Cluster 4 indicates the areas where no tissue is present.

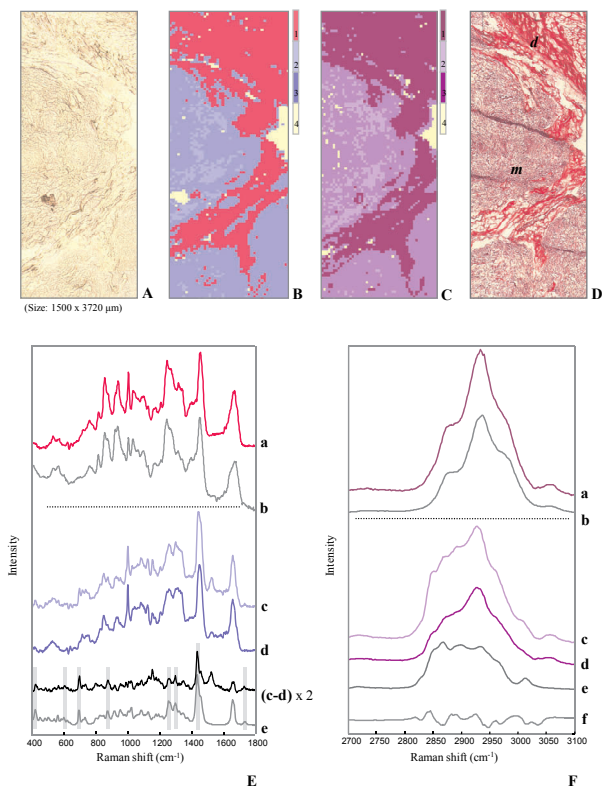


**Figure 3.** Fingerprint and HWVN Raman microspectroscopic mapping experiments on unstained frozen tissue section containing dura and meningioma. Panel **A**: Photograph of unstained frozen section of tumor attached to dura (original magnification, x5). Panel **B**: Pseudocolor Raman map of the tissue section shown in panel A, based on measurements in the fingerprint region (400-1800  $\text{cm}^{-1}$ ) and a K-means cluster analysis of the collected spectra (pixel size: 30 x 30  $\mu\text{m}^2$ , 50 x 124 pixels). Panel **C**: Pseudocolor Raman map of the tissue section shown in panel A, based on measurements in the HWVN region (2700-3100  $\text{cm}^{-1}$ ) and a K-means cluster analysis of the collected spectra (pixel size: 30 x 30  $\mu\text{m}^2$ , 51 x 127 pixels). It can be observed that the HWVN map closely resembles the fingerprint map. Panel **D**: Microscopic image of the tissue section of panel A after HE staining. Dura is indicated with "d", meningioma with "m". As follows from a comparison of both Raman images with the image of the HE-stained tissue section, cluster 1 corresponds to dura and clusters 2 and 3 correspond to meningioma. (Cluster 4 represents the areas where no tissue was present in the section.) Panel **E**: Analysis of spectra obtained in the fingerprint region. (a) Average spectrum of dura. (b) Spectrum of pure collagen. (For clarity of presentation collagen spectrum was divided by factor 6.) (c) and (d) Averages from two meningioma clusters (clusters 2 and 3 in panel C). (c - d): Positive difference spectrum of spectra c and d (c minus d), enlarged 2 times for clarity. (e) Spectrum of pure cholesterol linoleate (divided by factor 3). Spectral regions of the most prominent resemblance are highlighted by gray bars. (For clarity, the spectra have been shifted along the ordinate.) Panel **F**: Analysis of spectra obtained in the HWVN region. (a) Cluster-averaged spectrum of the dura (cluster 1 in panel C). (b) Spectrum of pure collagen. (c) Average spectrum of cluster 2 (represents the smaller part of meningioma in panel C), which was fitted with the average spectrum of cluster 3 (larger part of meningioma in panel C) and with the spectrum of pure cholesterol linoleate (see Figure 1, spectrum f). (d) and (e): Fit-spectra (spectra of cluster 3 and of cholesterol linoleate, respectively) are shown after multiplication by the fit-coefficients that resulted from the least-squares fit. (f) Fit-residual. (The spectra have been shifted along the ordinate, for clarity.)

The fingerprint cluster-averaged spectrum of dura [spectrum (a)] is shown in panel E. The dura is a tough fibrocollagenous layer mainly composed of fibroblasts and large amounts of collagen fibers.<sup>28</sup> This explains the strong similarity of the dura spectrum with the spectrum of pure collagen [spectrum (b)]. The averages of the meningioma clusters, clusters 2 and 3 [spectra (c) and (d) respectively], are also shown. Their difference spectrum [spectrum (c-d), 2 times enlarged] shows significant correspondence with the spectrum of pure cholesterol linoleate (e). This suggests that cholesterol (-esters) signal contributions (highlighted with gray bars) are much more prominent in average spectrum of the tumor area represented by cluster 2 than in that represented by cluster 3.

The same information can be obtained from the HWVN spectra. In panel F, cluster-averaged spectrum of dura (a) almost completely resembles the spectrum of collagen (b). The averaged spectrum of cluster 2 [spectrum (c), meningioma] was fitted with the average of cluster 3 [spectrum (d), meningioma] plus the spectrum of pure cholesterol linoleate [spectrum (e)]. The fit-spectra d and e are shown after multiplication by the fit-coefficients that resulted from the least-squares fit. The fit-residual is shown by spectrum (f). The fit-residual is far from perfect, which indicates that there are other significant differences in molecular composition between different tumor regions than just differences in cholesterol ester content. Nevertheless, the fact that the spectrum of cholesterol linoleate significantly contributes to the fit, confirms the information obtained from fingerprint Raman spectra, that esterified cholesterol is one of the compounds that distinguishes different regions of meningioma. (Least squares fits including spectra of other compounds, such as free cholesterol and/or fatty acids did not improve the fit). There is not much literature addressing the issue of the biochemical heterogeneity of microcystic meningiomas. Histologically this type of meningioma is characterized (among other features) by cells with foamy cytoplasm,<sup>29</sup> which may well contain lipids, including the cholesterol esters identified by Raman.

The lipid components of these vacuoles are represented by the cholesterol signal obtained by Raman spectra. From a practical point of view it is important that the clinical information, which is obtained in the HWVN region, matches the information, which is obtained in the fingerprint region. However, in this case, the actual biochemical basis for this clinical information is apparently not exactly the same in the two wavenumber regions.

### *Bladder tissue*

The result of a HWVN Raman mapping experiment carried out on a thin section of normal bladder tissue is displayed in Figure 4. Panel A shows the unstained cryo-section. Also on this tissue, a Raman mapping experiment was carried out using the fingerprint spectral region and the resulting Raman image (2405 spectra, lateral resolution 5  $\mu\text{m}$ ) is shown in panel B. Panel C shows the HWVN Raman map (1978 spectra, lateral resolution 7  $\mu\text{m}$ ). Again, the HWVN Raman image closely resembles the fingerprint Raman image. The Raman maps can be compared in the detail with the image of the same section after HE staining in

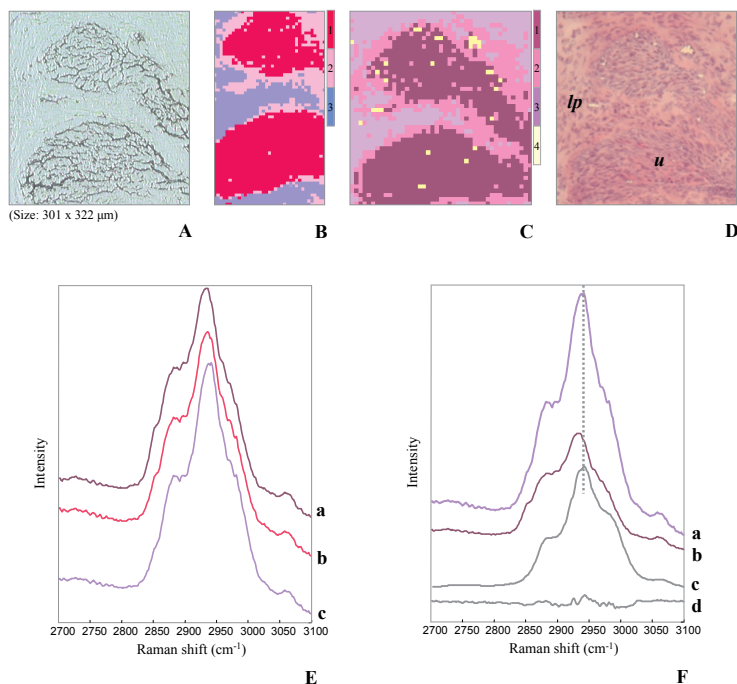


**Figure 4.** Fingerprint and HWVN Raman microspectroscopic mapping experiment on normal bladder tissue. Panel **A**: Photograph of an unstained bladder tissue section containing urothelium and underlying lamina propria (original magnification,  $\times 10$ ). Panel **B**: Pseudocolor Raman map of the bladder tissue section shown in panel A, based on measurements in the fingerprint region ( $400\text{--}1900\text{ cm}^{-1}$ ) and a K-means cluster analysis of the collected spectra (pixel size:  $5 \times 5\text{ }\mu\text{m}^2$ ,  $37 \times 65$  pixels). Panel **C**: Pseudocolor Raman map of the bladder tissue section shown in panel A, based on measurements in the HWVN region ( $2700\text{--}3100\text{ cm}^{-1}$ ) and a K-means cluster analysis of the collected spectra (pixel size:  $7 \times 7\text{ }\mu\text{m}^2$ ,  $43 \times 46$  pixels). Panel **D**: Photomicrograph of the tissue section of panel A after HE staining. Panel **E**: Cluster-averaged HWVN Raman spectra calculated for the clusters obtained in panel C. (a) Urothelium. (b) Area between urothelium and lamina propria. (c) Lamina propria. Panel **F**: The result of a least-squares fitting procedure. The cluster-averaged spectrum collected from lamina propria was fitted with the cluster-averaged spectrum of urothelium (see original spectrum a in panel E) plus a spectrum of pure collagen (see Figure 1, spectrum c). (a) Average spectrum of lamina propria. (b) and (c): Fit-spectra (cluster-averaged spectrum of urothelium and spectrum of pure collagen, respectively) shown after multiplication by their respective fit-coefficients. (d) Fit-residual. (For clarity, the spectra have been shifted along the ordinate.)

panel D (“u” indicates urothelium, “lp” indicates lamina propria). The urothelium (cluster 1) is clearly distinguishable from its supportive fibrocollagenous tissue (i.e., lamina propria, cluster 3), which is mainly composed of collagen.<sup>28</sup> The tissue area between urothelium and lamina propria is represented by cluster 2.

In panel E the average HWVN spectra of all tissue clusters are displayed. In the same way as described above for the other tissues, the characteristic HWVN spectral differences between the bladder urothelium and underlying lamina propria were analyzed by a least-squares

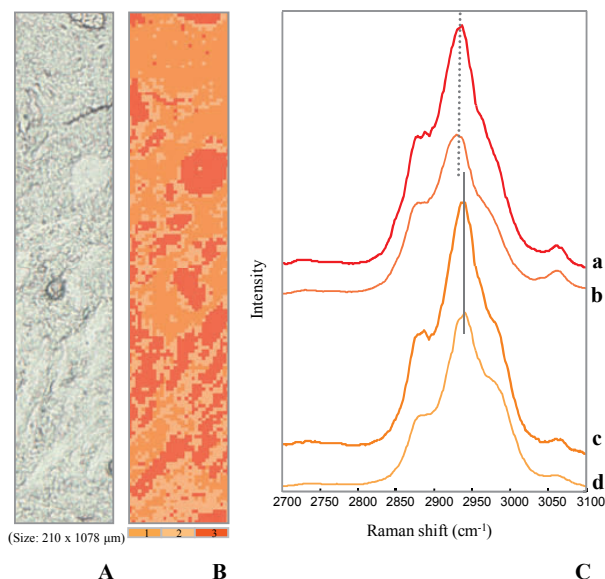


**Figure 5.** HWVN Raman mapping experiment on normal bladder tissue. Panel **A**: Photomicrograph of an unstained bladder tissue section containing fibrocollagenous stroma and smooth muscle tissue (original magnification, x10). Panel **B**: Pseudocolor Raman map of the bladder tissue section shown in panel A, based on measurements in the HWVN region (2700–3100  $\text{cm}^{-1}$ ) and a K-means cluster analysis of the collected spectra (pixel size:  $7 \times 7 \mu\text{m}^2$ ,  $30 \times 154$  pixels). There is a clear co-localization of tissue structures visible in panel A and structures visible in the Raman map. The routine histological evaluation of adjacent HE-stained tissue section (not shown) revealed that cluster 1 of the Raman map represents fibrocollagenous tissue and that cluster 3 represents smooth muscle. The tissue area in between fibrocollagenous stroma and smooth muscle is captured by cluster 2. Panel **C**: (a) Cluster-averaged spectrum of smooth muscle. (b) Spectrum of pure actin. (c) Cluster-averaged spectrum of fibrocollagenous stroma. (d) Spectrum of pure collagen. The spectra have been shifted along the ordinate for clarity.)

fitting procedure. Panel F shows the fit-residual (d) that remained after fitting the cluster-averaged spectrum obtained from lamina propria [cluster 3, spectrum (a)], with the average spectrum of urothelium cluster [spectrum (b) in panel E] and the spectrum obtained of pure collagen [see Figure 1, spectrum (c)]. The fit-spectra (b) and (c) are shown after multiplication by the fit-coefficients that resulted from the least-squares fit. Although the fit-residual reveals some spectral features, there is still a strong indication that the lamina propria, in comparison with the bladder epithelium, has stronger signal contributions of collagen. Estimation of the influence of noise on the fit results (see Materials and Methods) showed that also in this case it is negligible (noise-related uncertainty was  $\sim 1.3\%$  for both the fit-coefficients of urothelium and of collagen).

Figure 5 shows the result of HWVN Raman mapping experiment performed on unstained cryo-section (panel A) of normal bladder tissue containing the submucosal region of fibrocol-

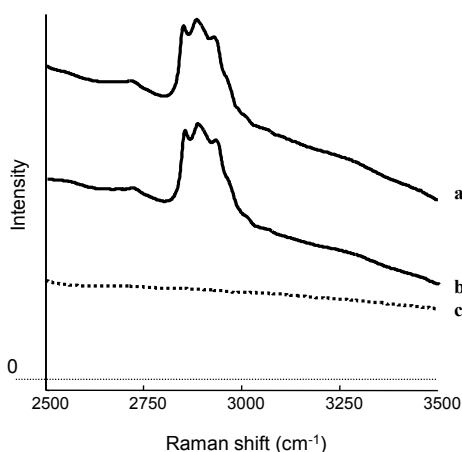


**Figure 6.** Example of a HWVN Raman measurement of porcine brain tissue using a single fiber Raman probe. (a) Raw *ex-vivo* HWVN Raman spectrum of white matter from porcine cerebellum tissue. (b) Same spectrum after correction for the instrument background. (c) Instrument background signal.

lagenous tissue with bundles of smooth muscle, as was revealed by the adjacent HE-stained section. A total of 4620 Raman spectra were obtained with a lateral resolution of  $7\mu\text{m}$  and a three-cluster KCA was performed. In the resulting Raman pseudocolor map (panel B), which corresponds closely to the photograph of the unstained section, fibrocollagenous tissue is presented by cluster 1 and smooth muscle by cluster 3. The tissue area in between fibrocollagenous stroma and smooth muscle bundles is captured by cluster 2. The cluster average spectrum of this area can be almost completely reconstructed from the averages of clusters 1 and 3, using a least-squares fitting procedure (result not shown). This implies that in the terms of its chemical content, cluster 2 represents a transitional area between smooth muscle and its surrounding connective tissue. The HWVN cluster-average spectrum of smooth muscle [panel C, spectrum (a)], which is rich in myosin and actin,<sup>28</sup> was compared with the HWVN spectrum of pure actin [panel C, spectrum (b)]. It illustrates that the average of smooth muscle is dominated by the signal contributions of actin as emphasized with round dot line. Actin and myosin are major intracellular contractile proteins in the muscle cells,<sup>28</sup> and their Raman spectra were found to be similar.<sup>30</sup> On the other hand, the HWVN cluster average from fibrocollagenous tissue [panel C, spectrum (c)], which is rich in collagen,<sup>28</sup> was compared with the HWVN spectrum of pure collagen [panel C, spectrum (d)]. Collagen appears to be the main contributor in the spectrum of fibrocollagenous tissue as highlighted by solid line.

#### *Ex vivo Raman Spectroscopy on Domestic Porcine Brain*

Using a single fiber-optic probe a HWVN Raman spectrum of white matter from normal porcine brain was collected *ex vivo*. Figure 6 shows the raw HWVN-spectrum (spectrum a,

including instrument background signal) and for comparison the same spectrum after correction for the background signal originating from instrument optics and the CCD-camera offset [spectrum (b)]. The background signal from the instrument is also shown [line (c)]. It can be observed that in the HWVN spectral region the instrument background signal is small compared to the tissue signal.

## Discussion

The fingerprint region of the Raman spectrum has been used extensively for tissue characterization and tissue classification. This paper demonstrates the possibility to distinguish between different histological structures in a variety of tissues (glioblastoma, meningioma and normal bladder tissue) based on Raman spectra obtained in the HWVN region.

This is an important finding since it means that clinically relevant information can be found in the HWVN region, which makes *in vivo* application of Raman spectroscopy by means of small and flexible fiber-optic probes much easier. In this wavenumber region the strong background signal from optical fibers, which is present in the fingerprint region is avoided.

The HWVN Raman pseudocolor maps presented here showed a high correspondence with spectral images recorded in fingerprint region on same unstained tissue sections. Therefore it appears that, just like fingerprint Raman spectra, HWVN Raman spectra contain sufficient information for tissue classification.

HWVN Raman spectra enable the discrimination of necrotic tissue from vital glioblastoma, because of the higher signal contributions of cholesterol esters in necrotic tumor tissue. The differences in the signal contributions of glycogen in the HWVN spectra from different regions of vital tumor illustrate the biochemical heterogeneity within the vital tumor. These findings are supported by our earlier study on glioblastoma tissue using fingerprint spectral region.<sup>5</sup> The spectra also point to a relatively higher DNA content in vital glioblastoma. This is to be expected because of the disintegration of cell nuclei during necrosis. Large spectral differences exist between the HWVN Raman spectra of dura and meningioma, because of the high collagen content of dura. One of the most pronounced differences separating the HWVN spectra of different parts of the meningioma (microcystic type) is the signal contribution of cholesterol esters. This is in accordance with the information obtained from the fingerprint Raman spectra. The biochemical heterogeneity of the microcystic subtype of meningioma as revealed by Raman spectroscopy reflects the tumor areas in which the cells with the vacuolated cytoplasm, containing lipids including cholesterol, dominate.<sup>29</sup>

In normal bladder tissue sections HWVN Raman spectra also enable a clear distinction between bladder epithelium and underlying lamina propria, with again the strong signal contribution of collagen being a distinguishing hallmark of the lamina propria. The bundles

of smooth muscle within the bladder wall were separated from their surrounding fibrocollagenous tissue by the stronger signal contribution of actin and the lower contribution of collagen. These results are in agreement with previous Raman spectroscopic studies of bladder wall in the fingerprint region of the Raman spectrum.<sup>6</sup>

Earlier studies, using a fiber-optic probe for measurements in the fingerprint region have already shown that real-time interpretation of *in vivo* spectra is possible.<sup>16</sup> This means that the feasibility of overcoming the technological hurdles that stand in the way of clinical implementation has been shown, which bodes well for the development of Raman guided clinical procedures and interventions, such as Raman guided biopsy and surgery.

## References

1. Tu A. T., Basic concept and elementary theory: Raman spectroscopy in biology, John Wiley & Sons, New York 1982.
2. Frank C. J., D. C. B. Redd, T. S. Gansler and R. L. McCreery, "Characterization of human breast biopsy specimens with Near-IR Raman spectroscopy", *Anal. Chem.* 1994; 66, 319 – 326.
3. Mahadevan-Jansen A., M. F. Mitchell, N. Ramanujam, A. Malpica, S. Thomasen, U. Utzinger and R. Richards-Kortum, "Near-infrared Raman spectroscopy for in vitro detection of cervical precancers", *Photochem. Photobiol.* 1998; 68, 123-132.
4. Hanlon E. B., R. Manorahan, T. W. Koo, K. E. Shafer, J. T. Motz, M. Fitzmaurice, L. R. Kramer, I. Itzakan, R. R. Dasari, and M. S. Feld, "Prospects for in vivo Raman spectroscopy", *Phys. Med. Biol.* 2000; 45, R1-R59.
5. Koljenović S., L-P. Choo-Smith, T. C. Bakker Schut, J. M. Kros, H. J. van den Berge and G. J. Puppels, "Discriminating vital tumor from necrotic tissue in human glioblastoma tissue samples by Raman spectroscopy", *Lab. Invest.* 2002; 82, 1265-1277.
6. de Jong B. W. D., T. C. Bakker Schut, K. P. Wolffenbuttel, J. M. Nijman, D. J. Kok and G. J. Puppels, "Identification of bladder wall layers by Raman spectroscopy", *J. Urol.* 2002; 168, 1771 – 1778.
7. Kneipp J., T. C. Bakker Schut, M. Kliffen, M. Menke-Pluijmers and G. J. Puppels, "Characterization of breast duct epithelia: a Raman spectroscopic study", *Vibrational Spectroscopy* 2003; 32, 67-74.
8. Mahadevan-Jansen A., M. F. Mitchell, N. Ramanujam, U. Utzinger and R. Richards -Kortum, "Development of a fiber optic probe to measure NIR Raman spectra of cervical tissue in vivo", *Photochem. Photobiol.* 1998; 68, 427 – 431.
9. Buschman R., E. T. Marple, M. L. Wach, B. Bennett, T. C. Bakker Schut, H. A. Bruining, A. V. Bruschke, A. van der Laarse and G. J. Puppels, "In vivo determination of the molecular composition of artery wall by intravascular Raman spectroscopy", *Anal. Chem.* 2000; 72: 3771-3775.
10. Bakker Schut T. C., M. Witjes, M. Sterenborg, O. Speelman, J. Roodenburg, E. Marple, H. A. Bruining and G. J. Puppels, "In vivo detection of dysplastic tissue by Raman spectroscopy", *Anal. Chem.* 2002; 72, 6010-6018.
11. Huang Z., A. McWilliams, H. Lui, D. McLean, D. I. S. Lam, and H. Zeng, "Near-infrared Raman spectroscopy for optical diagnosis of lung cancer", *Int. J. Cancer.* 2003; 107, 1047 – 1052.
12. Molckovsky A., L-M. Wong Kee Song, M. G. Shim, N. E. Marcon and B. C. Wilson, "Dignostic potential of near-infrared Raman spectroscopy in the colon: differentiating adenomatous from hyperplastic polyps", *Gastrointestinal Endoscopy*, 2003; 57, 396-402.
13. Motz J. T., M. Hunter, L. H. Galindo, J. A. Gradecki, J. R. Kramer, R. R. Dasari and M. S. Feld, "Optical fiber probe for biomedical Raman spectroscopy", *Appl. Opt.* 2004; 20, 542-554.
14. M. G. Shim, L. M. Song, N. E. Marcon and B. C. Wilson, "In vivo near-infrared Raman spectroscopy", *Photochem. Photobiol.* 2000; 72, 146-150.
15. Puppels G. J., M. van Aken, R. Wolthuis, P. J. Caspers, T. C. Bakker Schut, H. A. Bruining, T. J. Romer, H. P. J. Buschman, M. Wach and J. S. Robinson, "In vivo tissue characterization by Raman spectroscopy", *Proc. SPIE Biomed. Soc.* 1998; 3257, 78-85.
16. Boere I. A., T. C. Bakker Schut, J. van den Boogert, R. W. F. de Bruin and G. J. Puppels, *Vibrational Spectroscopy* 2003; 32, 47-55.
17. Thomas G. J., Jr., "New structural insights from Raman spectroscopy of proteins and their assemblies", *Biopol.* 2002; 67, 214-225.

18. Wolthuis R., M. van Aken, K. Fountas, J. S. Robinson Jr., H. A. Bruining and G. J. Puppels. "Determination of water concentration in brain tissue by Raman spectroscopy", *Anal. Chem.* 2001; 73, 3915-3920.
19. Caspers P. J., G. W. Lucassen, E. A. Carter, H. A. Bruining and G. J. Puppels, "In vivo confocal Raman microspectroscopy of skin: noninvasive determination of molecular concentration profiles", *J. Invest. Dermatol.* 2001; 116, 434-442.
20. van de Poll S. W. E., A. Moelker, R. Wolthuis, T. C. Bakker Schut, S. Koljenović, A. van der Laarse and G. J. Puppels, "Chemical characterization of atherosclerotic plaque by high-wavenumber Raman spectroscopy", (unpublished results).
21. van de Poll S. W. E., T. J. Romer, O. L. Volger, D. J. M. Delsing, T. C. Bakker Schut, H. M. G. Princen, J. W. Jukema, L. Havekes, A. van der Laarse and G. J. Puppels, "Raman spectroscopic evaluation of the effects of diet and lipid-lowering therapy on atherosclerotic plaque development in mice", *Arterioscler. Thromb. Vasc. Biol.* 2001; 21, 1630-1635.
22. Santos L. F., R. Wolthuis, S. Koljenović, R. M. Almeida and G. J. Puppels, "High wavenumber fiber-optic probes for in vivo Raman spectroscopy", *Anal. Chem.* 2005; 77, 6747-6752.
23. Wolthuis R., T. C. Bakker Schut, P. J. Caspers, H. P. Buschman, T. J. Römer, H. A. Bruining and G. J. Puppels, "Raman spectroscopic methods for in vitro and in vivo tissue characterization", Chap. 32 in *Fluorescent and luminescent probes for biological activity*, W.T. Mason, Editor, pp. 433-455, Academic Press, San Diego 1999.
24. Jolliffe I. T., *Principal component analysis*, Springer-Verlag, New York 1986.
25. Jain A. K. and R. C. Dubes, *Algorithms for clustering data*. Prentice Hall: Engelwood Cliffs 1988.
26. Glantz M. J., P. Burger, J. Herndon, A. Friedman, J. Cairncross, N. Vick and S. C. Schold, "Influence of the type of surgery on the histologic diagnosis in patients with anaplastic gliomas", *Neurology* 1991; 41, 1741 - 1744.
27. Kamitani H., H. Masuzawa, I. Kanazawa and T. Kubo, "Recurrence of convexity meningiomas: tumor cells in the arachnoid membrane", *Surg. Neurol.* 2001; 56, 228 - 235.
28. Stevens A. and J. Lowe, *Human histology*, Times Mirror International Publishers Limited, London 1997.
29. Bruner J. M., R. D. Tien, and D. S. Enterline, "Tumors of the meninges and related tissues", Chap. 11 in *Russell and Rubinstein's Pathology of tumors of the nervous system*, D. D. Bigner, R. E. McLendon and J. M. Bruner, Eds., pp. 69-139, Oxford University Press, New York 1998.
30. Carew E. B., H. E. Stanley, J. C. Seidel and J. Gergely, "Studies of myosin and its' proteolytic fragments by laser Raman spectroscopy", *Biophys. J.* 1983; 44, 219-224.

# Fiber-Optic Probes for *In Vivo* Raman Spectroscopy in the High Wavenumber Region

*Analytical Chemistry*  
2005, 77 (20): 6747-6752

6

L.F. Santos  
R. Wolthuis  
S. Koljenović  
R.M. Almeida  
G.J. Puppels

## Abstract

*In vivo* Raman spectroscopy using fiber-optic probes is hindered by the intense background signal, which is generated in the fused-silica fibers, in the fingerprint region of the Raman spectrum ( $\sim 0\text{--}2000\text{ cm}^{-1}$ ). Optical filtering is necessary to obtain tissue spectra of sufficient quality. The complexity of fiber-optic probes for fingerprint Raman spectroscopy, in combination with size constraints and flexibility requirements for *in vivo* use have been a major obstacle in the development of *in vivo* diagnostic tools based on Raman spectroscopy. A setup for remote Raman spectroscopic tissue characterisation in the high wavenumber region ( $\sim 2400\text{--}3800\text{ cm}^{-1}$ ) is presented. It makes use of a single, unfiltered, optical fiber for guiding laser light to the sample and for collecting scattered light and guiding it back to a spectrometer. Such a simple configuration is possible because the fused-silica core and cladding of the fiber present almost no Raman background signal at these wavenumbers. Several commercially available optical fibers were tested with respect to Raman signal background, to determine their suitability for *in vivo* Raman spectroscopy measurements in the high wavenumber region. Different fiber core, cladding, and coating materials were tested. Silica core-silica clad fibers with an acrylate coating and a black nylon jacket, proved to be one of the best candidates. *In vitro* measurements on brain tissue of a 6-month-old pig were obtained with a remote high wavenumber Raman setup. They illustrate the low background signal generated in the setup and the signal quality obtained with a collection time of 1 s.

## Introduction

Techniques that provide information about tissue structure or tissue composition are of great importance for the development of clinical diagnostic tools. Vibrational spectroscopy can provide detailed information about molecular composition and molecular structure of tissues. Diseases are accompanied by changes in molecular composition and structure and, therefore, by changes in their vibrational spectra. The aqueous nature of tissues precludes the use of infrared spectroscopy for most *in vivo* measurements, while Raman spectroscopy is suitable for measurements on aqueous and water-containing samples. Furthermore, since Raman spectroscopy does not require sample preparation and is nondestructive, it is in principle ideally suited for *in vivo* measurements and valuable information can be obtained in a matter of seconds.<sup>1</sup> Therefore, Raman spectroscopy meets important prerequisites for the development of tools for *in vivo* real-time tissue analysis<sup>2</sup>, during clinical procedures such as endoscopy, biopsy and surgery.

Such applications will often require the use of small and flexible fiber-optic probes. Unfortunately, when laser light is guided through a fused-silica fiber, Raman signal is generated in the fused-silica along the entire length of the fiber, which results in an intense background signal. This effect is aggravated when measurements are carried out in reflective or scattering materials, such as tissues, because a significant part of the incident laser light is reflected back into the fiber, thus generating more Raman signal and increasing the background level.

A wide range of fiber-optic probe designs for Raman spectroscopy has been realized in attempts to circumvent the problem of the fused-silica background. This has led to probe designs, with separate excitation and collection paths in order to minimize background. Several of these probe designs, such as 1-fiber-in-1-fiber-out or the n-fibers-around-1 configurations have been reviewed in detail by Lewis and Griffiths<sup>3</sup> and by Utzinger.<sup>4</sup> Although these multifiber designs improve the signal-to-background ratio, they have, according to Chong *et al.*,<sup>5</sup> lower signal collection efficiency than a bidirectional single fiber probe. Nevertheless, suppression of background signal in multifiber probes, by introduction of a band-pass filter at the tip of the illumination fiber, which only transmits laser light and blocks Raman signal that has been generated in the fiber, and a high-pass filter at the tip of the signal collection fibers, which block laser light, has led to probes that are suitable for (*in vivo*) tissue measurements.<sup>6-10</sup>

Although there are sometimes compelling advantages in separating source and detector fibers, such as greater flexibility in adapting location and size of the actual measurement volume to a particular application, the need for optical filtering has made the design and fabrication of small and flexible Raman probes for *in vivo* applications quite complex and expensive and leads to probes that are bulkier and less desirable for many applications. As far as we know, small and flexible fiber-optic Raman probes are not commercially available.

Therefore, it would be very desirable to avoid generation of probe signal background altogether. In that case, laser light delivery to the sample and collection of Raman scattered light from the sample could be accomplished with a single optical waveguide, which would lead to simple, inexpensive (and therefore disposable) probes, which would moreover be highly efficient, since the excitation and collection light cones totally overlap. One possibility was raised by Pelletier<sup>11</sup> with metallized capillary waveguide containing either argon gas or vacuum.

Another possibility is to use silica fibers in a wavenumber range where the background signal is almost absent, such as the 2400-3800  $\text{cm}^{-1}$  spectral region, hereafter referred to as the high wavenumber (HWVN) region. Although the information content of this spectral region is certainly not as high as that of the fingerprint region ( $\sim 0\text{-}2000\text{ cm}^{-1}$ ), it appears to contain sufficient information regarding molecular composition and structure for the identification and characterization of tissues, as recently demonstrated by Van de Poll *et al.*,<sup>12</sup> who used the signal from the CH-stretching vibrations within the HWVN region for a detailed Raman mapping analysis of atherosclerotic plaque in coronary arteries, and by Koljenović *et al.*,<sup>13</sup> who showed the potential of using the HWVN region in oncological applications of Raman spectroscopy. Earlier studies had already shown that this spectral region is suited for determination of water concentration in tissues, such as brain tissue<sup>14</sup> and skin.<sup>15</sup>

Although no silica Raman signal is expected in the HWVN region, a judicious choice of the optical fibers used is needed, since many cladding and coating materials present strong Raman peaks in the HWVN region.

The purpose of this study was to test several commercial types of optical fibers for *in vivo* Raman spectroscopy measurements, in the high wavenumber region, and to determine the best characteristics they should present, especially regarding the background level and the absence of Raman bands in the 2400-3800  $\text{cm}^{-1}$  spectral region. Preliminary results on brain tissue of a 6-month-old pig exemplify the performance of the remote high wavenumber Raman setup.

## Experimental Section

### Instrumentation

#### *Fiber-Optic Probe Raman Measurements*

A tuneable titanium sapphire laser (Spectra-Physics, 3900 S), working at  $\sim 720\text{ nm}$ , was pumped by an  $\text{Ar}^+$  laser (Coherent Innova 300). Laser light passed through a short-pass filter and was focused in the core of the optical fiber being tested, with a fused-silica lens (Opto-Sigma, 10-mm focal length). The fiber guided the laser light to the sample at the distal end of the fiber. The output power at the distal end of the fibers was  $\sim 120\text{ mW}$ . Backscattered

laser light and Raman-scattered light from the sample were collected by the same fiber, guided back to the proximal end of the fiber, and collimated again by the 10-mm fused-silica lens. The collimated light passed through a custom-made chevron-type dielectric filter system,<sup>16</sup> for suppression of the intensity of backscattered laser light. The Raman signal was then focused (Edmund Optics, near-infrared achromatic lens, 35-mm focal length) into a 1-mm-diameter detection fiber (Fiberguide Industries), which in turn was connected to a round-to-slit adapter consisting of a bundle of 64 fibers with a core diameter of 100  $\mu\text{m}$  and an outer diameter of 125  $\mu\text{m}$  (i.e., including cladding and coating), and with the 64 fibers arranged in a linear array at the spectrometer entrance. From the linear array of fibers, the signal was launched into a modified multichannel dispersive spectrometer (System 100, Renishaw Ltd., Wotton-under-Edge, U.K.), which projected a Raman spectrum on the CCD detector (fitted with an EEV front illuminated CCD chip, 576 x 384 pixels) for each of the 64 fibers. The spectral resolution was 12  $\text{cm}^{-1}$ . Figure 1 shows a schematic diagram of the experimental setup.

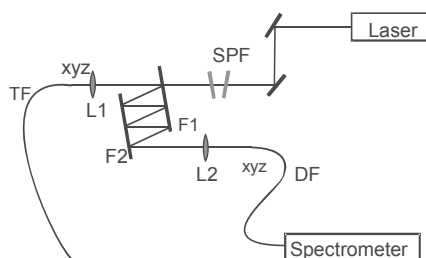


**Figure 1.** Schematic diagram of the experimental setup. Laser light of  $\sim 720$  nm passes through a short-pass filter (SPF) and is focused in the testing fiber (TF) by a fused-silica lens (L1). Backscattered radiation is filtered by a chevron-type high-pass filter (F1/F2) and focused (L2) into the detection fiber (DF). For details, see text.

### *Raman Microspectroscopic Measurements*

The transverse section of each optical fiber was analysed in the HWVN region, to obtain the Raman spectra of the different optical fibers constituents. The Raman system used<sup>17</sup> consist of a Leica DM-RE microscope (Leica, Cambridge, U.K.) coupled to a Renishaw System 100 spectrometer and with excitation from an  $\text{Ar}^+$  laser (Coherent Innova 300) and a tuneable titanium sapphire laser (Spectra-Physics, 3900 S), working at 718 nm. An 80x objective (Olympus - 0.75 NA) was used and the signal was collected in 16 scans of 2 s each.

## Fiber Specifications

Several commercial multimode step-index optical fibers were tested (Table 1), to study the effects of parameters such as core material, cladding material, and coating material on the fiber background signal measured in the setup of Figure 1.

The fibers were connected (SMA 905) at the proximal end, and not connected on the distal end, which was in contact with the tissues. Both ends were mechanically polished using a 1- $\mu\text{m}$   $\text{Al}_2\text{O}_3$  polishing paper.

Each fiber was tested by means of Raman measurements in the HWVN region, with the fiber tip in air and in cyclohexane (Aldrich, ACS reagent grade) in order to compare the fiber background signal and the Raman signal intensity from the sample.

Table 1. Specification of the Tested Optic-Fiber Probes (According to the Manufacturers)

Fiber	Company and Model	Core ( $\varnothing$ $\mu\text{m}$ )	Cladding ( $\varnothing$ $\mu\text{m}$ )	Coating ( $\varnothing$ $\mu\text{m}$ )	Jacket ( $\varnothing$ $\mu\text{m}$ )
F1	Fiberguide Industries (USA) SFS200/210/233RTF (High OH)	Si (200)	Silicone (210)		Polyamide
F2	INO (CAN) Z100FJ	ZBLAN (135)	ZBLAN (200)	FEP Teflon	Acrylate
F3	INO (CAN) Z100FV	ZBLAN	ZBLAN (125)		Acrylate
F4	INO (CAN) Z120AI	ZBLAN (150)	ZBLAN (250)	FEP Teflon	Acrylate
F5	Thor Labs (USA) UHNA3	$\text{SiO}_2 + \text{GeO}_2$	$\text{SiO}_2$ (125)		Acrylate (250)
F6	Polymicro Technologies (USA) JNFP300330370500	Si (300)	Doped Si (330)	Polyamide (370)	Black Nylon (500)
F7	Polymicro Technologies (USA) FIP200220240 (Ultra low OH)	Si (200)	Doped Si (220)		Polyamide (240)
F8	Polymicro Technologies (USA) JTF1LH200230500 (low OH)	Si (200)	Doped Si (230)	Acrylate (360)	Tefzel
F9	Thor Labs (USA) FT-200-EMT (low OH from 3M)	Si (200)	TECS (225)		Tefzel (500)
F10	CeramOptec (USA) WFG200/220 T	Si (200)	F-Doped Si (220)	Silicone (320)	Tefzel (650)
F11	Fiberguide Industries (USA) AFH200/220 N	Si (200)	Doped Si (220)	Silicone (320)	Nylon (390)
F12	Oxford Electronics (UK) HPSIR200P	Si (200)	Doped Si (225)		Acrylate (360)
F13	Oxford Electronics (UK) HPSIR200P-AI	Si (200)	Doped Si (225)		Aluminum (360)
F14	Fibertech (GER) AS200/220/IRAN (Low OH)	Si (200)	F-Doped Si (220)	Acrylate (350)	Nylon (500)
F15	Polymicro Technologies (USA) FLUA200220240 (low OH)	Si (200)	Teflon (220)		Acrylate (240)

## Tissue Analysis

Brain tissue and dura (i.e., brain covering) were obtained post-mortem from a 6-month-old pig, which had been sacrificed in another unrelated terminal experiment. The porcine brains were sliced in sections, 5–10 mm thick, which enabled visual identification of white and gray matter. Small pieces (~ 10x10 mm) of dura were also prepared. Tissue specimens were placed in a physiological NaCl solution (0.9%) and used in Raman probe experiments without any further treatment.

Raman spectra of dura, white matter, and gray matter were measured in the 2400–3800  $\text{cm}^{-1}$  spectral region, using sampling times of 1, 10 and 60 s, with the distal end of the fiber in contact with the tissue.

## Data Processing

Raman spectra were acquired using a GRAMS (Thermo Galatic) software interface and were processed by automated routines developed in-house, using Matlab 6.5 software (Mathworks, Natick, USA). Data pretreatment consisted of cosmic ray removal, wavenumber calibration, instrument response correction and subsequent linearization of the wavenumber axis, including interpolation of signal intensities. Wavenumber calibration was performed using the Raman spectrum of cyclohexane and the emission lines of a neon lamp and a neon-argon lamp. The detection efficiency of the setup was corrected using a white light spectrum of a calibrated tungsten-halogen lamp (Philips) with known filament temperature (NIST-traceable) scattered by a certified reflectance standard (Labsphere®).<sup>1,18</sup> Further details of data processing have been described elsewhere.<sup>19</sup>

Spectra of the setup without the fiber were used to subtract the optical components background from the fiber, to analyse just the fiber background signal.

For tissue measurements, spectra obtained with the optical fiber in air (i.e., without a sample at the distal end of the fiber) were used to subtract out the system signal background including residual Raman and luminescence signals from the fiber.

## Results and Discussion

### *Fiber Assessment (Choice of Fiber Material)*

Commercially available optical fibers with different core, cladding, and coating materials were analysed, to find the best-suited combination of materials for a HWVN Raman fiber-optic probe. Table 1 presents the specifications (as supplied by the fiber manufacturers) of the fibers that were tested in this study.

Fibers with fused-silica (with high and low water content), germanium-doped silica, and fluoride core materials were investigated. The fiber with a high-OH fused-silica core (F1) showed strong features in the spectral region of the OH-stretching vibrations, which in-

interfered with signal detection, while fluoride core (F2, F3 and F4) and silica-germania core (F5) fibers showed high background levels that covered the important CH-stretching region ( $\sim 2700\text{--}3100\text{ cm}^{-1}$ ), where the major HWVN signal contributions of proteins and lipids are found. This high background is probably due to fluorescence effects caused by impurities.

The lowest background signal was obtained from fibers with a low-OH fused-silica core. Among these fibers, different cladding compositions, ranging from fused doped-silica to silicone, TECS and Teflon, were analysed in order to determine the best-suited core/cladding composition. Moreover, although the compositions of core and cladding are primarily responsible for the performance of an optical fiber, different coating materials can influence the overall behaviour of the fiber. Therefore, different coating materials, such as polyamide, nylon, acrylate, TECS, Tefzel, and metallic coating, such as aluminium, were also analysed. The relative intensities of the background signals obtained from the different fibers are shown in Figure 2. All spectra were recorded in the same conditions (laser power at the entrance of the fibers of 150 mW and optical fibers in air), and spectra of the setup without the fiber were used to subtract the optical components background from the fiber.

Polyamide-coated fibers (F1, F6 and F7) presented an extremely high background level compared with the other fibers (left panel), independently of the core/cladding “pair”, that makes them inadequate for this application. Some fibers (such as F8, F9, F10 and F11) showed a clear Raman background signal in the  $2700\text{--}3100\text{ cm}^{-1}$  spectral interval, while others showed no signal at all (right panel).

Raman spectra obtained with a Raman microspectrometer, of cladding and coating materials that presented characteristic features in the HWVN, are shown in Figure 3. The silicone Raman spectrum is in agreement with the literature<sup>20</sup>.

Tefzel (F8 and F9)-coated fibers showed some weak features in the CH-stretching region, while silicone peaks at  $2905$  and  $2964\text{ cm}^{-1}$  are present even when silicone is used as coating, as seen in panel b of Figure for the F10 and F11 fibers. No particular Raman features were observed for acrylate and metal-coated fibers, although acrylate also has characteristic peaks in the HWVN region as seen in Figure 3.

Therefore, coating materials that exhibit fluorescence such as polyamide or a strong Raman signal such as silicone, in the  $2400\text{--}3800\text{ cm}^{-1}$  interval, should be avoided. In the ideal case, no light should reach the coating. However, fiber loss mechanisms can cause light to be lost from the core and enter the cladding and coating of the fibers and vice versa, enabling scattered light generated in the cladding and coating materials to re-enter into the core.

Other factors should also be considered, because acrylate Raman peaks (Figure 3) were not observed in the background Raman signal obtained from acrylate-coated fibers (Figure 2, right panel).

This is probably due to different refractive index relations. In fact, fibers with coatings with higher refractive index than the cladding, such as acrylate-coated fibers, favour the exit of any Raman signal from the coating reducing their possible re-entrance in the optical path.

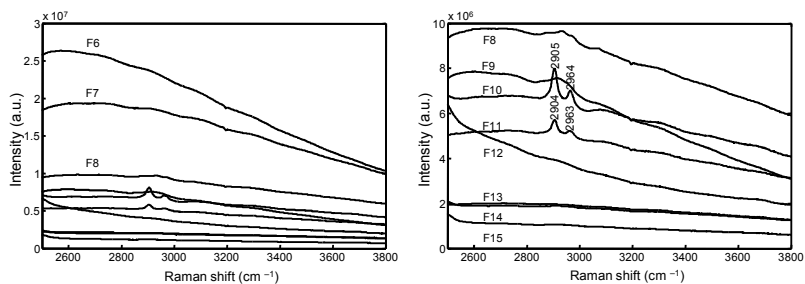


**Figure 2.** Raman spectra of different types of commercial optical fibers (see Table 1 for details). All spectra were recorded in the same conditions, and similar correction procedures were adapted (see text). Left panel: Results for the tested fibers. Right panel: Same as left panel but without the polyamide coated fibers F6 and F7. Note that the intensity scale of the right panel is different from that of the left panel.

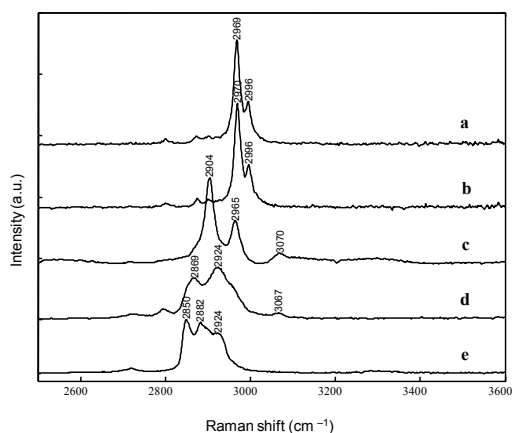


**Figure 3.** Raman spectra of cladding and coating materials, obtained with a Raman microscope with 718 nm radiation: (a) TECS cladding (F9); (b) Tefzel coating (F8); (c) silicone coating (F10); (d) acrylate coating (F5); (e) black Nylon coating (F14).

For this reason it is important to consider core, cladding, and coating materials to find a suitable type of fiber for single-fiber HWVN Raman spectroscopy.

The best results were obtained with fiber cladding and coating materials that have no signal in the 2400–3800  $\text{cm}^{-1}$  wavenumber interval, such as fused-silica or Teflon cladding (F12, F13, F14 and F15) and an acrylate coating (F12, F13 and F15) or a metal coating (F14).

As can be seen in Figure 2 (right panel), the F12 fiber presented a somewhat higher background level than the other acrylate fibers; therefore, differences in Raman background performance between fibers obtained from different suppliers should be tested for. The F14 optical fiber, which has a fused-silica core, a fused-silica cladding, an acrylate coating, and a black nylon jacketing presented the highest Raman signal of cyclohexane of all fibers, as well as one of the lowest background levels, and was therefore chosen for further testing.

The decrease in fiber core diameter, the increase in the NA of the optical fiber, or both result in the reduction of the depth from which the Raman signal is collected<sup>21</sup> and thereby enhance the depth resolution, which can result in higher selectivity in tissue analysis. However, the depth from where the Raman signal is collected also depends on tissue absorbance, being lower for highly absorbing tissues.<sup>21</sup>

### Tissue Analysis

Tissue measurements were conducted *ex vivo* with the single-fiber HWVN Raman setup shown in figure 1, employing the acrylate-coated, fused-silica core, fused-silica cladding fiber F14 (Table 1). A laser power of ~120 mW was used and no signs of tissue degradation were observed.

Although some background signal remained, characteristic features of the analysed tissues were observed and good quality spectra could be obtained, even for measuring times of 1 s. Figure 4 compares the measured spectra (A) of cerebellum white matter with the corrected spectra (B) after subtracting the background signal from the setup (C).

In figure 5 the background subtracted Raman spectra of porcine brain tissues are shown (white matter; gray matter and dura) obtained with a signal integration time of 60 (left panel) and 1 s (right panel).

HWVN Raman spectra showed high signal contributions of lipids in the white matter: increase of the 2851 cm<sup>-1</sup> (CH<sub>2</sub> symmetric stretching) and the 2885 cm<sup>-1</sup> (CH<sub>2</sub> asymmetric stretching) bands and high signal contributions of proteins in gray matter; increase of the 2934 cm<sup>-1</sup> band (CH<sub>3</sub> symmetric stretching) and the ~2960 cm<sup>-1</sup> shoulder (CH<sub>3</sub> asymmetric stretching). These results are in agreement with previous studies on brain tissue<sup>22-24</sup>. Raman spectrum of dura presented a major peak at 2943 cm<sup>-1</sup> and two shoulders at 2886 and 2982 cm<sup>-1</sup>, which is most probably due to the signal contributions of collagen. This is expected since the dura contains large amounts of collagen fibers.<sup>25</sup> Similar results were obtained by recording and analysing Raman microspectroscopic maps in HWVN and fingerprint regions of thin human tissue sections of dura.<sup>13</sup>

Although a better signal to noise is achieved with longer measuring times, the 1-s spectra (Figure 5, right panel) present sufficient information to easily distinguish between the different tissues. We are currently extending this study, investigating the possibility to distinguish between a large number of brain structures *in situ*. It should be noted that the current setup has not yet been fully optimized for signal detection efficiency. An improvement by roughly 1 order of magnitude is therefore feasible.

These results show the possible use of single, unfiltered, optical probes and, subsequently, the use of Raman spectroscopy with simple and inexpensive probes, for *in vivo* tissue measurements, in the high wavenumber region. The high flexibility of these probes should facilitate the development of Raman-guided clinical procedures and interventions such as biopsy and surgery.

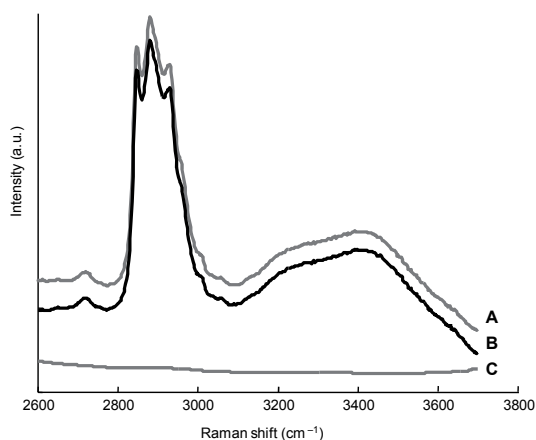


**Figure 4.** Raman spectra of white matter (cerebellum, porcine brain), with 10-s signal collection time: (A) raw spectrum; (B) corrected spectrum; (C) probe background.

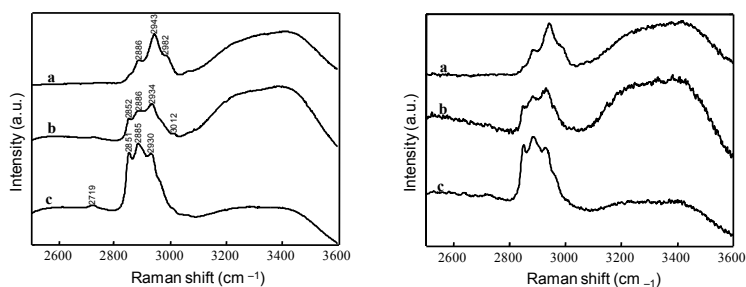


**Figure 5.** Single-fiber HWVN Raman spectra of porcine brain tissue. Left panel: Measurements of (a) dura, (b) gray matter, (c) white matter obtained with a signal collection time of 60 s. Right panel: Measurements of (a) dura, (b) gray matter, (c) white matter obtained with a signal collection time of 1 s.

## Conclusions

Commercial optical fibers were tested for Raman spectroscopy measurements in the 2400–3800  $\text{cm}^{-1}$  spectral region. The lowest background contributions of the tested optical fibers were obtained when fused-silica core/cladding was used, but the type of coating material is also essential for the best performance. Coating materials such as polyamide, Tefzel and silicone should be avoided. Coating materials such as acrylate present low background, but the best results were obtained with an acrylate coating plus a black nylon jacketing. This is probably due to the different refractive indexes of the materials involved. Metal-

coated fibers also presented low background levels and are suitable for use in single-fiber HWVN Raman measurements.

We have also shown that Raman spectra of dura, white matter, and gray matter of porcine brain tissues could be easily differentiated in a matter of seconds.

## References

1. Bakker Schut, T.C.; Witjes, M.J.H.; Sterenborg, H.J.C.M.; Speelman, O.C.; Roodenburg, J.N.L.; Marple, E.T.; Bruining, H.A.; Puppels, G.J. *Anal. Chem.* 2000, 72(24), 6010-6018.
2. Hanlon, E.B.; Manoharan, R.; Koo, T.-W.; Shafer, K.E.; Motz, J.T.; Fitzmaurice, M.; Kramer, J.R.; Itzkan, I.; Dasari, R.R.; Feld, M.S. *Phys. Med. Biol.* 2000, 45, 1-59.
3. Lewis, I.R.; Griffiths, P.R. *Appl. Spectrosc.* 1996, 50(10), 12A-30A.
4. Utzinger, U. *J. Biomed. Opt.* 2003, 8(1), 121-147.
5. Chong, C.K.; Shen, C.; Fong, Y.; Zhu, J.X.; Yan, F.X.; Brush, S.; Mann, C.K.; Vickers, T.J. *Vib. Spectrosc.* 1992, 3, 35-45.
6. Carrabba, M.M.; Rauh, R.D. EIC Laboratories, Norwood, MA. U.S. Patent 5,112,127, 1992.
7. Owen, H. Kaiser Optical Systems, Ann Arbor, MI. U.S. Patent 5,377,004, 1994.
8. Mahadevan-Jansen, A.; Richards-Kortum, R. *J. Biomed. Opt.* 1996, 1, 31-70.
9. Shim, M.G.; Wilson, B.C.; Marple, E. Wach, M.; *Appl. Spectrosc.* 1999, 53(6), 619-627.
10. Motz, J.T.; Hunter, M.; Galindo, L.H.; Gardecki, J.A.; Kramer, J.R.; Dasari, R.R.; Feld, M.S. *Appl. Opt.* 2004, 43(3), 542-554.
11. Pelletier, M.; 30<sup>th</sup> Annual Meeting of the Federation of Analytical Chemistry & Spectroscopy Societies, Ft. Lauderdale, FA, Oct 19-23, 2003, 163-164.
12. van de Poll, S.W.E.; Moelker, A.; Wolthuis, R.; Koljenović, S.; Pattynama, P.M.T.; Van der Laarse, A.; Puppels, G.J. (unpublished results).
13. Koljenović, S.; Bakker Schut, T.C.; Wolthuis, R.; De Jong, B.; Santos, L.F.; Caspers, P.J.; Kros, M.; Puppels, G.J. *J. Biomed. Opt.* 2005, 10, 031116.
14. Wolthuis, R.; Van Aken, M.; Fountas, K.; Robinson Jr., J.S.; Bruining, H.A.; Puppels, G.J. *Anal. Chem.* 2001, 73, 3915-3920.
15. Caspers, P.J.; Lucassen, G.W.; Carter, E.A.; Bruining, H.A.; Puppels, G.J. *J. Investigative Dermatology* 2001, 116(3), 434-442.
16. Puppels, G.J.; Huizinga, A.; Krabbe, H.W.; De Boer, H.A.; Gijsbergs, G.; De Mul, F.F.M. *Rev. Sci. Instrum.* 1990, 61(12), 3709-3712.
17. van de Poll, S.W.E.; Romer, T.J.; Volger, O.L.; Delsing, D.J.M.; Bakker Schut, T.C.; Princen, H.M.G.; Havekes, L.M.; Jukema, J.W.; Van der Laarse, A.; Puppels, G.J. *Arterioscler. Thromb. Vasc. Biol.*, 2001, 21, 1630-1635.
18. Wolthuis, R.; Bakker Schut, T.C.; Caspers, P.J.; Buschman, H.P.J.; Romer, T.J.; Bruining, H.A.; Puppels, G.J. in *Fluorescent and Luminescent Probes for Biological Activity*; Mason W.T., Ed.; Academic Press: London, 1999; pp 433-455.
19. Bakker Schut, T.C.; Wolthuis, R.; Caspers, P.J.; Puppels, G.J. *J. of Raman Spectrosc.* 2002, 33, 580-585.
20. Smit, E.E.; Erckens, R.J.; Hendrikse, F.; Motamedi, M.; Wicksted, J.P.; March, W.F.J. *Cataract. Refract. Surg.* 1999, 25, 1498-1504.
21. Zhu, Z.Y.; Yappert, M.C. *Appl. Spectrosc.* 1992, 46(6), 912-918.
22. Mizuno, A.; Hayashi, T.; Tashibu, K.; Maraishi, S.; Kawauchi, K.; Ozaki, Y.; *Neuroscience Lett.* 1992, 141, 47-52.
23. Mizuno, A.; Kitajima, H.; Kawauchi, K.; Muraishi, S.; Ozaki, Y. *J. Raman Spectrosc.* 1994, 25, 25-29.
24. Ong, C.W.; Shen, Z.X.; He, Y.; Lee, T.; Tang, S.H. *J. of Raman Spectrosc.* 1999, 30, 91-96.
25. Stevens, A.; Lowe, J. *Human Histology*; Times Mirror International Publishers Limited: London, 1997.



# Raman Spectroscopic Characterization of Porcine Brain Tissue Using a Single Fiber-Optic Probe

*Analytical Chemistry*  
2007, 79 (2): 557-564



S. Koljenović  
T.C. Schut  
R. Wolthuis  
A.J. Vincent  
G. Hendriks-Hagevi  
L. Santos  
J.M. Kros  
G.J. Puppels

## Abstract

Accurate targeting of diseased and healthy tissue has significantly been improved by MRI/CT based navigation systems. Recently, intraoperative MRI navigation systems have proven to be powerful tools for the guidance of the neurosurgical operations. However, the widespread use of such systems is held back by the by costs, time consumption during operation, and the need for MR compatible surgical devices. Raman spectroscopy is a nondestructive optical technique that enables real-time tissue identification and classification and has proved to be a powerful diagnostic tool in a large number of studies. In the present report, we have investigated the possibility of distinguishing different brain structures by using a single fiber-optic probe to collect Raman scattered light in the high wavenumber region of the spectrum. For the Raman measurements, 7 pig brains were sliced in the coronal plain and Raman spectra were obtained of 11-19 anatomical structures. Adjacent brain structures could be distinguished based on their Raman spectra, reflecting the differences in their biochemical composition and illustrating the potential Raman spectroscopy holds as a guidance tool during neurosurgical procedures.

## Introduction

Sparing healthy tissue while optimizing treatment of lesions is an important goal of most surgical procedures and of brain surgery in particular, including both therapeutic (e.g., resection of brain tumors) and diagnostic (e.g., brain biopsy) neurosurgical actions.

Intraoperative MR imaging technology has been put forward as a powerful tool for imaging during neurosurgical procedures.<sup>1-9</sup> The development of image-guided neurosurgery has improved the safety of neurosurgical procedures over the past decade. Navigational devices have improved localization of lesions and thereby help to minimize damage to healthy tissue during neurosurgical operations.

However, efficient use of an intraoperative MRI unit is held up by the need for MR-compatible instruments and radiofrequency-shielded operating rooms. In addition, the cost and size of intraoperative MRI systems hamper their widespread use.<sup>9</sup>

Moreover, most available systems for image-guided surgery are based on a three-dimensional brain model calculated from CT and/ or MR images acquired before the operation. These systems, however, cannot provide information about the dynamic changes (i.e., brain shift) that occur during the surgical procedures.<sup>1-13</sup> Brain shifts are caused by many interacting factors such as brain edema, tissue removal and loss of cerebrospinal fluid.<sup>12</sup> This impairs precise targeting of lesions and increases the risk of damaging of eloquent areas that may impair their functions and lead to movement and speech disturbances. Moreover, inaccurate targeting of a tumor may lead to underestimation of the tumor grade when histopathological diagnosis is made on nonrepresentative tumor tissue sampled during stereotactic brain biopsy. Hence, there is a need for a tool for real-time guidance of neurosurgical procedures, which should enable the neurosurgeon to precisely target lesions, sample tumor tissue for histopathological diagnosis, and remove tumor, by providing direct information about biochemical composition of tissue.

In the study reported here, we have investigated the possibility of using a simple fiber-optic probe to distinguish between different brain structures, in order to create a basis for the development of an *in vivo* Raman method for real-time brain surgery guidance.

Raman spectroscopy is a nondestructive vibrational spectroscopic technique that provides detailed information about the molecular composition, molecular structure and molecular interactions in cells and tissues. A large number of *ex vivo* studies have reported on the possibility to discriminate between healthy and diseased tissues such as skin, colon, larynx, cervix, lung and breast.<sup>14-16</sup> Nevertheless, only a few studies have reported on the characterization of brain tissue using Raman spectroscopy. Mizuno *et al.* published Raman spectra of different anatomical and functional structures of rat brain in 1992 and of different brain tumors in 1994.<sup>17,18</sup> In 2001, Wolthuis *et al.* demonstrated that Raman spectroscopy can be powerful tool for accurate determination of water concentration in brain tissue.<sup>19</sup> Accurate discrimination between vital and necrotic brain tumor tissue based on the Raman spectra

was accomplished in an *in vitro* study by Koljenović *et al.*<sup>20</sup> More recently, we published promising *in vitro* results on detection of meningioma in dura mater.<sup>21</sup> Krafft *et al.* obtained Raman spectra of different human brain lipids.<sup>22</sup> The potential of the technique for *in vivo* application by means of fiber-optic probes has also been demonstrated.<sup>23-27</sup> Subsequently, several groups have reported on the design and realization of miniaturized fiber-optic probes, some of which indeed enabled collection of high quality *in vivo* Raman spectra.<sup>28-30</sup> In all these studies, the spectral region between 400 and 2000  $\text{cm}^{-1}$  (the “fingerprint region”) was used because it is very rich in spectroscopic information. However, the actual *in vivo* implementation of fingerprint Raman spectroscopy for clinical purposes is hampered by the fact that, in the 400-2000  $\text{cm}^{-1}$  spectral region, intense Raman scattering is generated in the optical fiber itself. This results in a strong background signal, which in turn has led to complex and expensive probe designs. The technological hurdle of designing and constructing suitable fiber optic probes can be eliminated by using the high wavenumber (HWVN) region (2000-4000  $\text{cm}^{-1}$ ).<sup>31</sup> Because in this spectral region no Raman signal is generated in the fiber itself, a simple standard optical fiber can be used to guide laser light to the tissue and to collect scattered light. In previous studies, we have shown that HWVN Raman spectroscopy can be used to determine water concentration in brain tissue and in skin and to obtain information on the compositional heterogeneity of atherosclerotic plaques.<sup>19,32,33</sup> Moreover, we have recently demonstrated that the spectra obtained in the HWVN region contain essentially the same diagnostic information as those obtained from the fingerprint region of the Raman spectrum.<sup>34</sup>

Here we show that *ex vivo* HWVN Raman spectra obtained by a single fiber probe contain the information needed for discrimination between various brain structures, showing the feasibility of the development of an *in vivo* Raman method for real-time brain surgery guidance. We used a single fiber-optic probe to collect Raman spectra of morphologically different structures (i.e., gray matter, white matter, various nuclei) in unfixed cross sections of porcine brain. Cluster analysis was performed to investigate whether the neighboring structures could be distinguished based on their Raman spectra. Biochemical differences between brain structures were analyzed by a least-squares fitting procedure in which a database of pure compound spectra was used.

## Materials and Methods

### Sample Handling and Sample Preparation

For these experiments, seven brains were harvested from Landrace pigs that were sacrificed during an unrelated medical experiment. The age of all pigs was ~ 6 months and the weight ~ 40 kg. After harvesting, the brains were directly dissected in the coronal (i.e., transversal) plane in 8 – 15-mm-thick slices, which were kept at -80°C until further use. For Raman

experiments, these frozen samples were thawed at room temperature, kept wet in a physiological NaCl solution (i.e., 0.9%), and measured without further treatment. During all Raman experiments, environmental conditions (i.e., temperature and humidity) were kept constant.

### Raman *Ex Vivo* Experiments

Raman spectra were obtained by a setup utilizing a single optical fiber to illuminate the tissue and to collect the scattered light from the tissue. A report describing the setup in detail has recently been published.<sup>31</sup> Briefly, 719-nm laser light from an argon-ion pumped titanium: sapphire laser (Spectra-Physics, 3900 S) was coupled into the proximal end of optical fiber with a core diameter of 300  $\mu\text{m}$  (core and cladding consisting of fused silica, 2 m in length) (AS300/330IRAN, FiberTech, Berlin, Germany). At the distal end of the fiber, laser light was guided to the tissue and scattered light from the tissue was collected and guided back to the proximal end of the fiber. The light emerging from the fiber was then guided into a spectrometer where the HWVN Raman spectrum of the tissue was recorded. Raman scattered light was detected in the 2400–3800  $\text{cm}^{-1}$  spectral interval with a spectral resolution of 8  $\text{cm}^{-1}$ . A modified dispersive imaging spectrometer was used to record the spectra (Renishaw system 100, Wotton-under-Edge, Gloucestershire, U.K.), equipped with a thermoelectrically cooled deep-depletion CCD (charge-coupled device) camera.

Different anatomical brain structures were selected by macroscopic examination of the surface of the tissue slices. Depending on the quality of sample preparation, 11–19 diverse structures were identified in each of the 7 brains. For each structure, HWVN Raman spectra were collected at 6–12 points (3 spectra per point) depending on the size of the structure measured. All spectra were collected with the probe touching the sample during 10 s of signal collection time per spectrum. Tissue samples were illuminated with  $\sim 80$  mW of laser power during the Raman measurements.

### Reference Spectra

Reference Raman spectra were obtained of the following commercially available compounds: cholesterol (150680, ICN Biochemicals Inc., Ohio, USA), galactocerebroside (C-4905, Sigma-Aldrich Chemie, Zwijndrecht, The Netherlands), phosphatidylcholine (D-8180, Sigma-Aldrich Chemie, Zwijndrecht, The Netherlands), sphingomyelin (S-7004, Sigma-Aldrich Chemie, Zwijndrecht, The Netherlands), Bovine Serum Albumin (referred as BSA, A-9647 Sigma-Aldrich Chemie, Zwijndrecht, The Netherlands) and DNA (D-1501, Sigma, St Louis MO, USA). These compounds were used without further purification. Bovine serum albumin (BSA) and DNA were dissolved in demineralized water (400mg/ml and 20mg/ml respectively). The Raman spectra of dissolved compounds were corrected for the contribution of the water.

## Spectral Analysis

Software developed in-house, which runs in a Matlab environment (The MathWorks, Inc., Natick, MA, USA) and makes use of the multivariate statistical analysis toolbox PLS-toolbox 2.0.0c (Eigenvector Research, Inc., Manson, WA, USA), was used for all data processing.

### *Pretreatment of Spectra*

Following acquisition, spectra were first calibrated using Raman calibration standards as described earlier.<sup>35</sup> Briefly, two Raman calibration standards with accurately known peak frequencies, 4-acetamidophenol (3102.4, 3326.6  $\text{cm}^{-1}$ ) and cyclohexane (2666.4, 2852.9, 29383.3  $\text{cm}^{-1}$ ) along with the emission lines of a neon and a neon-argon lamp were used for wavenumber calibration of the spectra. To correct recorded Raman spectra for the wavelength-dependent signal detection efficiency of the setup, the emission spectrum of a calibrated tungsten band lamp was used.<sup>35</sup> Cosmic rays were removed from the spectra, and the background signal from optical elements in the laser light delivery pathway was subtracted from the tissue Raman spectra.

To minimize the influence of any slowly varying fluorescence, optics background signal, and water signal in the spectra, the spectra were scaled using an extended multivariate scatter correction procedure, using the spectra of the optics background and of water as interferences, and a third order polynomial background.<sup>36</sup>

### *Hierarchical Cluster Analysis*

The feasibility for discriminating between (spectra of) adjacent brain structures was investigated using hierarchical cluster analysis (HCA). Per brain, 6-12 spectra were measured for each structure. Principal component analysis (PCA) was performed on this data set to obtain a representation of the spectra in a reduced number of orthogonal variables. The PCA scores accounting for more than 99.0% of the variance captured were used as new variables.

From this new data set, the PCA scores of two or more adjacent structures served as input for a HCA using Ward's clustering algorithm and the Euclidean distance measure. This procedure was repeated for all sets of neighboring structures that we wanted to discriminate.

### *Spectral Modeling*

A least-squares fitting procedure was performed to obtain information about the differences in chemical composition between various brain structures. The averaged *ex vivo* HWVN Raman spectrum of a structure was fitted with that of the adjoining structure and a set of pure compound spectra (e.g., cholesterol, galactocerebroside, phosphatidylcholine, sphingomyelin, BSA and DNA). This fitting procedure resulted in positive or negative fit contributions of the reference spectra, pointing out higher or lower concentrations of the corresponding compounds in tissue structures that were compared. Relative scattering cross sections were not determined, and therefore, all fit contributions are presented as arbitrary units and not as weight percentages.

Seven compounds, known to be present in the brain in a measurable quantity, were selected as a first reference set.<sup>37</sup> In order to minimize error due to nonorthogonality of the reference spectra, spectra that could be fitted for more than 95% by the other reference spectra were excluded from the reference set, resulting in a reduced reference data set of six spectra including lipids (cholesterol, galactocerebroside, DL-alpha-phosphatidylcholine disteroyl and sphingomyelin), DNA, and BSA. The latter compound was chosen to represent the protein content of brain in general. To estimate the uncertainty in the fit results due to noise, artificial (normally distributed) noise was added to the tissue spectra that were fitted. In this way, the signal-to-noise ratio of the tissue spectra was artificially decreased by a factor of 2. A new set of fit-coefficients was calculated according to the least-squares fitting procedure described above. This was repeated 100 times for each of the tissue spectra, and the standard deviation obtained for each of the fit-coefficients served as an estimate for the uncertainty in the fit results.

The relative uncertainty of the fit itself was expressed as the part of the spectrum that could not be explained by the reference spectra, i.e., as the quotient of the absolute spectral content of the residual and the spectral content of the spectrum that is fitted (which is 1 due to normalization).

## Results

In the region between 2400 and 3800  $\text{cm}^{-1}$ , also called the high wavenumber region, most of the spectral features obtained from tissue are strongly overlapping CH-stretching vibrations in the region 2800 – 3050  $\text{cm}^{-1}$ .<sup>38</sup> OH-stretching vibrations (primarily due to water), which appear in the spectral interval 3100-3500  $\text{cm}^{-1}$ , smaller signal contributions of SH-stretching

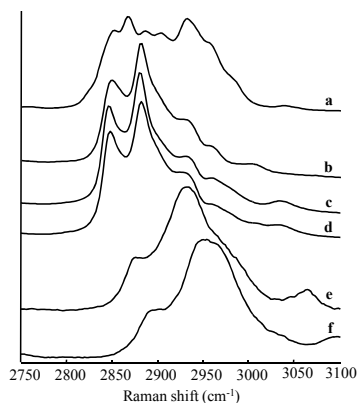


**Figure 1.** HWVN Raman spectra of pure chemical compounds: (a) cholesterol; (b) galactocerebroside; (c) DL-alpha-phosphatidylcholine disteroyl; (d) sphingomyelin; (e) bovine serum albumin (BSA); (f) DNA.

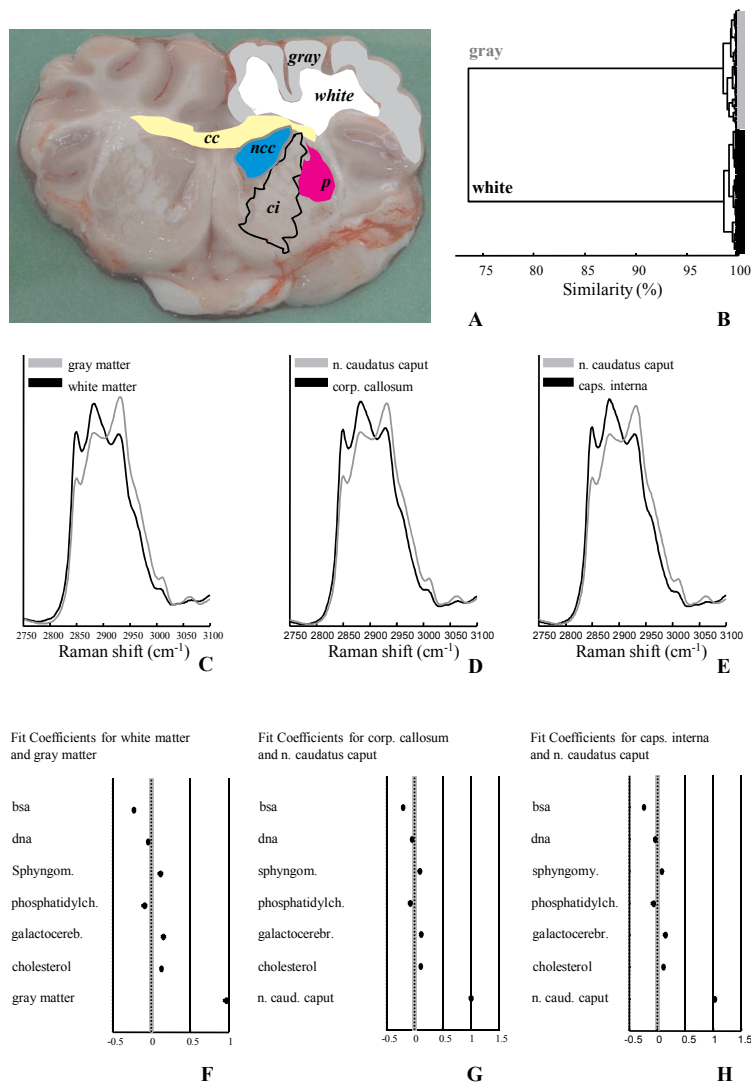


**Figure 2.** Discriminating between adjacent structures of a frontal brain cross-section of the domestic pig brain based on HCA of HWVN Raman spectra and analysis of the spectral differences between adjacent structures by least-squares fitting procedure. **A:** Photograph of the coronal cross-section from the frontal part of the domestic pig brain with gray matter ("gray"), white matter ("white"), corpus callosum ("cc"), nucleus caudatus caput ("ncc"), putamen ("p"), and capsula interna ("ci") highlighted. **B:** Dendrogram from a HCA of gray and white matter spectral averages, from all pig brains. **C:** HWVN averaged Raman spectra of gray matter and white matter. **D:** HWVN averaged Raman spectra of nucleus caudatus caput and corpus callosum. **E:** HWVN averaged Raman spectra nucleus caudatus caput and capsula interna. **F:** Fit-coefficients resulting from the fit of the average spectrum of gray matter with the averaged spectrum of white matter plus the reference spectra obtained from cholesterol, galactocerebroside, phosphatidylcholine, sphingomyelin, BSA, and DNA. Gray bars represent uncertainty interval of fit-coefficients. Fit-coefficients

show that, compared to the gray matter, the white matter has relatively stronger signal contributions of sphingomyelin, cholesterol, and galactocerebroside but weaker signal contributions from protein (BSA), phosphatidylcholine, and DNA. **G:** Fit-coefficients resulting from the fit of the average spectrum of corpus callosum with the averaged spectrum of nucleus caudatus caput plus the same set of reference spectra (see legend of panel F). Gray bars represent uncertainty interval of fit-coefficients. The fit-coefficients indicate that the corpus callosum has stronger signal contributions from lipids (i.e., sphingomyelin, cholesterol, and galactocerebroside) in comparison with the nucleus caudatus caput, which is characterized by stronger protein, phosphatidylcholine, and DNA signal contributions. **H:** Fit-coefficients resulting from the fit of the average spectrum of capsula interna and with the averaged spectrum of nucleus caudatus caput plus the same set of reference spectra (see legend of panel F). Gray bars represent uncertainty interval of fit-coefficients. The fit-coefficients indicate that the capsula interna compared to the nucleus caudatus caput has stronger signal contributions from lipids. Nucleus caudatus caput is characterized by stronger protein, phosphatidylcholine and DNA signal contributions.

vibrations  $2500 - 2600 \text{ cm}^{-1}$ , and NH-stretching vibrations between  $3100$  and  $3500 \text{ cm}^{-1}$ .<sup>38,39</sup> Because almost all spectral signatures from lipids and proteins appear in the  $2750 - 3100 \text{ cm}^{-1}$  interval, this range was chosen for analysis of the Raman spectra.

Raman spectra from commercially available pure compounds are shown in Figure 1. Note that, although quite similar in appearance, the spectra of galactocerebroside (b), phosphatidylcholine (c), and sphingomyelin (d) are linearly independent (see Materials and Methods). The adjoining brain structures that could easily be identified by visual inspection of cross sections were separated for 100% by HCA based on the averaged Raman spectra obtained from all seven pig brains used in these experiments. In all cases, white matter (cerebrum and cerebellum) and other structures consisting of myelinated fibers such as corpus callosum, capsula interna, crus cerebri, fimbria hippocampi, and tractus opticus, were clearly distinguished from cortical gray matter and from basal nuclei and subcortical gray areas (e.g., nucleus caudatus, putamen, thalamic nuclei, substantia nigra, corpus geniculatum laterale, and hippocampus). Although histomorphologically similar, the structures such as white matter of cerebrum and white matter of cerebellum were distinguished from each other in all brains investigated by HCA. Similarly, the averaged spectra of fimbria hippocampi and of tractus opticus formed separate clusters for all cases. Moreover, a number of adjoining nuclei could also be 100% separated from each other for all brains by HCA (e.g., thalamic nuclei and nucleus caudatus caput).

Examples of the results of Raman experiments on the cross sections from the frontal part of brain for all seven pigs are shown in Figure 2. Panel A shows the cut surface of a cross section. From the cortex towards the basis of the brain, a number of structures is highlighted including gray matter (labeled “gray”), white matter (labeled “white”), corpus callosum (labeled “cc”), nucleus caudatus caput (labeled “ncc”), capsula interna (labeled “ci”), and putamen (labeled “p”). HCA performed on averaged spectra of gray and white matter for all pig brains resulted in a clear separation of gray and white matter, as shown in (B). Panels C - E show the averaged Raman spectra of adjoining brain structures: white and gray matter (C), corpus callosum and nucleus caudatus caput (D), and capsula interna and nucleus caudatus caput

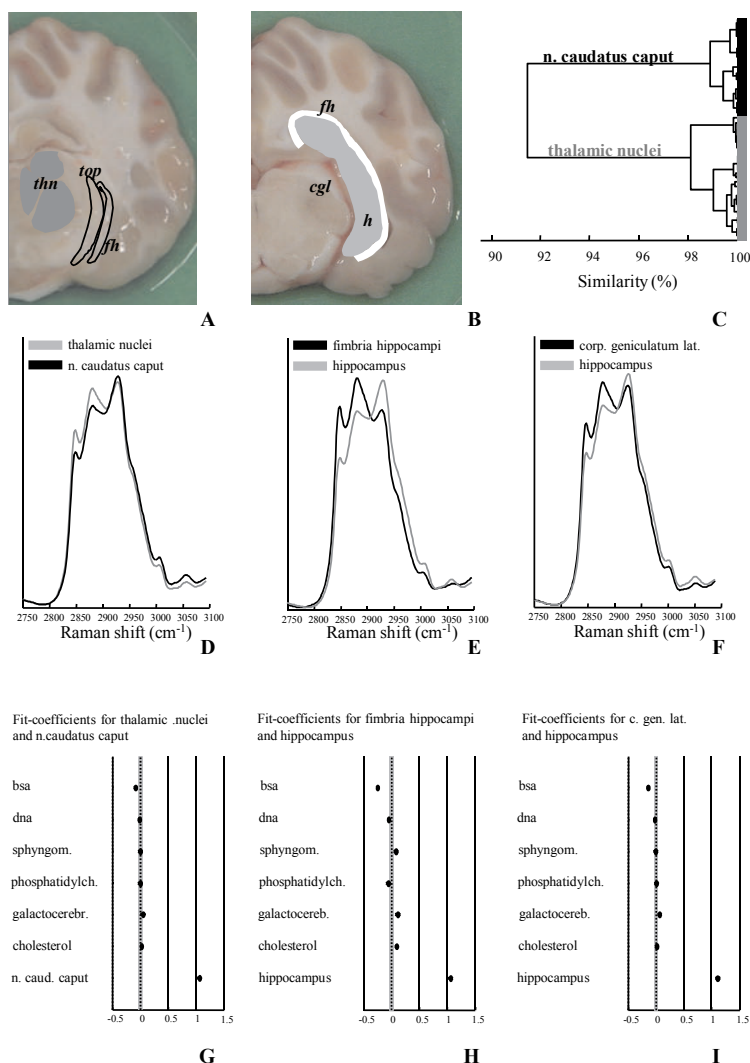


**Figure 3.** Discriminating between adjacent structures on consecutive cross sections toward the occipital part of the domestic pig brain based on HCA of HWVN Raman spectra and analysis of the spectral differences between adjacent structures by least-squares fitting procedure. **A:** Photograph of the coronal cross-section of brain at the level of the thalamus with thalamic nuclei ("thn"), tractus opticus ("top") and fimbria hippocampi ("fh") highlighted. **B:** Photograph of the coronal cross-section toward the occipital site of the brain (i.e., to the back of the head) with hippocampus ("h") with adjoining fimbria hippocampi ("fh"), and corpus geniculatum laterale ("cgl") highlighted. **C:** Dendrogram from a HCA of the averaged spectra of thalamic nuclei and nucleus caudatus caput, from all pig brains. **D:** HWVN averaged Raman spectra of thalamic nuclei and nucleus caudatus caput. **E:** HWVN averaged Raman spectra of hippocampus and fimbria hippocampi. **F:** HWVN averaged Raman spectra of hippocampus and corpus geniculatum laterale. **G:** Fit-coefficients resulting from the fit of the average spectrum of thalamic nuclei with the averaged spectrum of nucleus

caudatus caput plus the set of reference spectra (see the legend of Figure 2, panels C, D and F). Gray bars represent uncertainty interval of fit-coefficients. The fit-coefficients indicate that signal contributions from protein (BSA) appear stronger in the nucleus caudatus caput compared to the thalamic nuclei, which show stronger contributions from lipids such as galactocerebroside. **H:** Fit-coefficients resulting from the fit of the average spectrum of fimbria hippocampi with the averaged spectrum of hippocampus plus the set of reference spectra (see the legend of Figure 2, panels C, D and F). Gray bars represent uncertainty interval of fit-coefficients. Fit-coefficients indicate that the hippocampus compared to the fimbria hippocampi has stronger signal contributions from protein and weaker contributions from galactocerebroside. Moreover, sphingomyelin shows relatively higher spectral contribution to fimbria hippocampi when compared with hippocampus. **I:** Fit-coefficients resulting from the fit of the average spectrum of corpus geniculatum laterale with the averaged spectrum of hippocampus plus the set of reference spectra (see the legend of Figure 2, panels C, D and F). Gray bars represent uncertainty interval of fit-coefficients. Fit-coefficients indicate that the hippocampus has stronger signal contributions from protein and weaker contributions from galactocerebroside compared to the corpus geniculatum laterale.

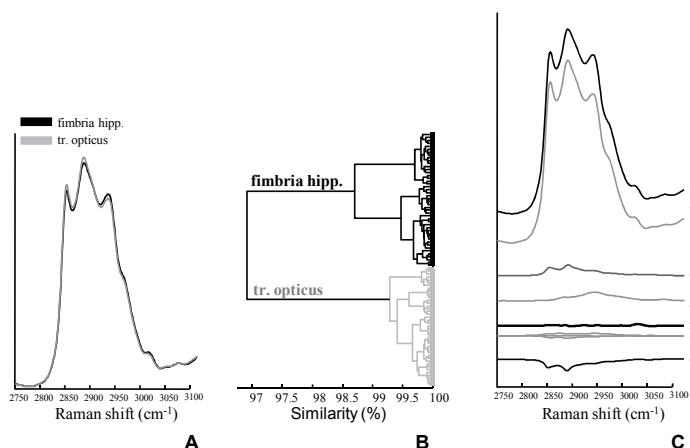
(E). The spectral differences, pointing to differences in chemical composition, were analyzed by a least-squares fitting procedure. The average spectrum of a structure was fitted with the averaged spectrum of the adjoining structure plus the reference spectra obtained from cholesterol, galactocerebroside, phosphatidylcholine, sphingomyelin, BSA, and DNA. The corresponding fit-coefficients are depicted by F - H. For all fit-coefficients, the uncertainty interval is shown (gray zone). The intervals were calculated from 100 repeated fits on the same spectrum, but with a different noise pattern, as described above. The uncertainty in the fit, as defined above, is depicted as a gray zone around 0. If the uncertainty of a fit-coefficient for a compound is in the range of the uncertainty of the fit, the significance of the contribution of that compound to the fit is questionable. Fit-coefficients from panel F show that compared to gray matter, white matter has relatively stronger signal contributions of sphingomyelin, cholesterol, and galactocerebroside but weaker signal contributions from protein (BSA), phosphatidylcholine, and DNA. Similarly fit-coefficients in (G) and (H) indicate that myelinated structures such as corpus callosum and capsula interna have stronger signal contributions from lipids (i.e., sphingomyelin, cholesterol, and galactocerebroside) in comparison with nucleus caudatus caput, which is characterized by stronger protein, phosphatidylcholine, and DNA signal contributions. Furthermore, in all brains measured, the nuclei such as putamen and substantia nigra were separated from capsula interna and from crus cerebri, respectively. As described above for nucleus caudatus, these nuclei also showed relatively higher signal contributions of proteins and lower of lipids (results are not shown).

Figure 3 shows two adjacent pig brain cross sections, from the level of the thalamus (A) towards the occipital site (i.e., to the back of the head, B). In (A), the thalamic nuclei (labeled “*thn*”), and the tractus opticus (labeled “*top*”) with adjoining fimbria hippocampi (labeled “*fh*”) are highlighted. In (B) the hippocampus (labeled “*h*”) with the fimbria hippocampi (labeled “*fh*”) and the corpus geniculatum laterale (labeled “*cgl*”) can be identified. For all brains, the thalamic nuclei and the adjoining, frontally located, nucleus caudatus

caput (see A) were separated by HCA based on their averaged spectra, as shown in (C). The hippocampus could be separated from the fimbria hippocampi and from the corpus geniculatum laterale using HCA based on their averaged spectra from all brains measured (dendrograms not shown). The Raman averaged spectra of these adjoining structures show large differences (D-F), which were analyzed using fitting procedure as described above. The corresponding fit-coefficients for each two adjoining structures are shown in panels G - I. For all fit-coefficients, the uncertainty interval is also shown (gray zone). Judging from the fit-coefficients shown in (G), signal contributions from protein (BSA) appear stronger in the nucleus caudatus caput compared to the thalamic nuclei, which show stronger contributions from lipids such as galactocerebroside. Fit-coefficients in (H) and (I) indicate that the hippocampus compared to the fimbria hippocampi and to the corpus geniculatum laterale, respectively, has stronger signal contributions from protein and weaker contributions from galactocerebroside. Moreover, sphingomyelin shows relatively higher spectral contribution to fimbria hippocampi when compared with hippocampus (H).

Figure 4 shows that HCA based on the averaged spectra of myelinated structures such as fimbria hippocampi and tractus opticus for all brains resulted in two separate clusters (B), despite the fact that there are only slight spectral differences. The underlying biochemical differences between these structures were analyzed using least square fitting procedure as described above. The averaged spectrum of fimbria hippocampi was fitted with the average spectrum of tractus opticus plus the set of pure compounds spectra. Panel C shows the fit-results. For clarity of presentation, the fit-spectra of pure compounds are shown after multiplication by their fit-coefficients (c, d, f and e). Therefore, a positive or negative spectrum signifies that more or less of that compound is present in fimbria hippocampi than in tractus opticus. The fit-results show that fimbria hippocampi (a) has relatively stronger signal contributions from sphingomyelin (c) and protein (BSA, d) but weaker signal from phosphatidylcholine (e) when compared with tractus opticus (b). Although the fit-residual is small (g), the presence of small spectral features does point to other minor differences that are not represented by the spectral fit-set. Note that the spectra of cholesterol, galactocerebroside and DNA are almost flat, which indicate that these compounds did not show significant spectral contributions (labeled together, f).

Similarly, the averaged spectra of white matter of cerebrum and white matter of cerebellum showed small differences. Nevertheless, also, these structures were completely separated by HCA for all pig brains. The least-squares fitting procedure revealed that the most prominent biochemical differences between these two myelinated structures are again related to different spectral contributions from proteins, phosphatidylcholine, and sphingomyelin as shown for fimbria hippocampi and tractus opticus in Figure 4. Compared with the white matter of cerebellum, the white matter of cerebrum has relatively higher spectral contributions from proteins (BSA) and sphingomyelin and lower contributions from phosphatidylcholine.



**Figure 4:** Discrimination of adjacent structures that mainly consist of myelinated fibers, based on HCA of Raman spectra and analysis of the spectral differences by a least-squares fitting procedure. **A:** HWVN averaged Raman spectra of fimbria hippocampi and tractus opticus. **B:** Dendrogram from a HCA based on the spectral averages of fimbria hippocampi and tractus opticus, from all pig brains. **C:** The result of a least-squares fitting procedure. The averaged spectrum collected from fimbria hippocampi was fitted with the averaged spectrum of tractus opticus plus set of reference spectra (see Figure 1). Fit-set spectra are shown after multiplication by their respective fit-coefficients. Note that the intensity of the spectra of cholesterol, galactocerebroside, and DNA (labeled together as **f**) are almost equal to the residual and therefore do not contribute significantly to the fit. (**a**) Average spectrum of fimbria hippocampi; (**b**) Tractus opticus; (**c**) Sphingomyelin; (**d**) Bovine serum albumin (BSA); (**e**) Phosphatidylcholine; (**f**) Cholesterol, Galactocerebroside, and DNA; (**g**) Fit-residual. (The spectra have been shifted along the ordinate for clarity.)

Cholesterol, galactocerebroside, and DNA showed no significant spectral contributions. The results are not shown.

A number of myelinated structures could, however, not be separated from each other by HCA for all brains studied. White matter (cerebrum) was separated from corpus callosum and from fimbria hippocampi for two brains, tractus opticus from capsula interna for five brains, and from crus cerebri for four brains. Moreover, in a number of cases, various adjoining nuclei could also not be separated from each other for all brains. These included nucleus ruber and substantia nigra (separated for three pig brains), thalamic nuclei and putamen (separated for three pig brains), and corpus geniculatum laterale and corpus geniculatum mediale (separated for four brains). The results are not shown.

## Discussion

Brain shift during neurosurgical operations cannot be handled by currently available navigation systems based on the pre-operative MR/ CT images. Although progress in intraoperative

MRI systems has significantly improved neurosurgical procedures, widespread use of such systems is held back due to the need for all surgical devices to be MR-compatible including the patient's bed. Besides the high costs, such devices are not always of sufficient quality for surgical purposes.

The advantages of the application of Raman spectroscopy for investigating *in vitro* biochemical composition of healthy and diseased brain tissues has been demonstrated in a number of studies.<sup>17-22</sup> Thus far, no studies have been published using a single fiber Raman probe for characterization of brain tissue. The aim of this study was to make a first step towards the development of an *in vivo* Raman method for intraoperative guidance of neurosurgical procedures by exploring the feasibility of a single fiber-optic probe in distinguishing between different brain structures. Such a method may be suitable for routine use because it is fast, simple to use and relatively low cost. Thus, Raman spectroscopy in addition to existing pre-operative imaging techniques (CT\ MRI) is particularly attractive.

The results of this study show that the biochemical information represented in Raman spectra enables identification of different brain structures. We used HCA to obtain information about the dissimilarity between spectra of different brain structures. This resulted in a clear separation for a large number of adjoining brain structures, based on the spectra obtained from all brains studied. The biochemical differences represented by the Raman spectra were analyzed by a least-squares fitting procedure. The Raman spectra from white and gray matter show large differences, representing the differences in molecular composition of these brain tissues. Raman spectra of gray matter are characterized by stronger signal contributions from protein, DNA and phosphatidylcholine when compared with white matter. This can be explained by the fact that gray matter is composed of neuronal cell bodies.<sup>40</sup> The lipids such as cholesterol, sphingomyelin, and galactocerebroside are the most prominent features in the spectra obtained on white matter. This was expected since white matter consists of bundles of axons covered by a sheet of myelin. Myelin is a lipoprotein consisting of 70 to 85% lipid.<sup>37</sup> Various nuclei (e.g., nucleus caudatus, putamen, thalamic nuclei, corpus geniculatum laterale, substantia nigra) were separated from white matter and from other structures consisting of myelinated bundles of axons, for all brains. Similar to the gray matter, the Raman spectra of nuclei show stronger signal contributions from protein, DNA and phosphatidylcholine. This is in accordance with the fact that nuclei represent clusters of neuronal bodies, which are function-specific.<sup>40</sup> In some cases, the Raman spectra from structures that mainly consist of myelinated fibers (e.g., fimbria hippocampi and tractus opticus, cerebrum and cerebellum white matter) could be consistently separated for all brains by HCA, despite the small spectral differences. Analysis showed that these differences resulted from variation in their lipid signal contributions, which probably reflects the differences in the level of myelination. Furthermore, a number of nuclei were separated from each other for all brains, based on the different signal contributions of proteins and lipids. This is most probably due to the amount of myelinated fibers that pass through these nuclei.<sup>40</sup>

However, not all (adjacent) structures could be separated for all pig brains. Especially for the smaller and/ or thinner brain structures (e.g., nucleus ruber, substantia nigra, fimbria hippocampi, and tractus opticus), the accuracy of the Raman measurements may be hampered by the effective measurement volume of the probe. A systematic study of probe measurement volume in brain tissue has not yet been carried out. It is likely that for the smaller structures, some signal was also collected from adjoining brain structures either by inaccurate positioning of the probe or by effective measurement volume extending beyond the targeted brain structure. The result of this is that the biochemical differences between small adjacent structures are suboptimally probed and lead to misclassifications.

This will be investigated in more detail in future studies. The fiber core size and numerical aperture are means of controlling the measurement volume of a single fiber probe to a certain extent, but tissue scattering properties also play an important role.

The results of this study show that the combination of a single fiber-optic probe and the use of the HWVN part of the spectrum provides a potential and easy-to-use *in vivo* Raman system that can discriminate between the various structures present in the brain.

The probes used in this study were bare fibers which were not optimized for depth resolution or collection efficiency. By optimizing the probes and the spectrometer, it will be possible to reduce the time needed to obtain a spectrum suitable for tissue discrimination to subsecond levels, making it a feasible tool for real-time guidance of clinical procedures. The laser power applied in the current experiments can safely be applied during brain surgery. The temperature increase in brain tissue as a result of irradiation with laser light of 830nm up to 250 mW is in the order of  $\sim 2$  °C as we have shown in a previous work.<sup>41</sup> Moreover, improvements in the sensitivity of the instrumentation will enable signal collection with even lower laser power than used in this work. Furthermore, earlier Raman spectroscopic studies, using a fiber-optic probe have already shown that real-time interpretation of *in vivo* spectra in these time frames is possible.<sup>42</sup>

These technological advances along with the biochemical information obtained from the Raman spectra open the way for the development of an *in vivo* real-time Raman spectroscopic method for improving image-guided neurosurgical procedures.

## References

1. Black P.M.; Moriarty T.; Alexander E.; Stieg P.; Woodard E.; Gleason P. L.; Martin C. H.; Kikinis R.; Schwartz R. B.; Jolesz F. A. *Neurosurgery* 1997, 41, 831-845.
2. Seifert V.; Zimmermann M.; Trantakis C.; Vitzthum H-E.; Kühnel K.; Raabe A.; Bootz F.; Schneider J-P.; Schmidt F.; Dietrich J. *Acta Neurochir (Wien)* 1999, 141, 455-464.
3. Zimmermann M.; Seifert V.; Trantakis C.; Kühnel K.; Raabe A.; Schneider J-P.; Dietrich J.; Schmidt F. *Acta Neurochir (Wien)* 2000, 143, 327-337.
4. Zimmermann M.; Seifert V.; Trantakis C.; Raabe A. *Acta Neurochir (Wien)* 2001, 143, 327-337.
5. Nimsky C.; Ganslandt.; Cerny, S.; Hastreiter P.; Greiner G.; Fahlbusch R. *Neurosurgery* 2000, 47, 1070-1080.
6. Nimsky C.; Ganslandt O.; Hastreiter P.; Fahlbusch R. *Surg. Neurol.* 2001, 56, 357-65.
7. Hastreiter P.; Rezk-Salama C.; Soza G.; Bauer M.; Greiner G.; Fahlbusch R.; Ganslandt O.; Nimsky C. *Med. Image Anal.* 2004, 8, 447-464.
8. Albayrak B.; Samdani A. F.; Black P. M. *Acta Neurochir (Wien)* 2004, 146, 543-557.
9. Iseki H.; Muragaki Y.; Nakamura R.; Ozawa N.; Taniguchi H.; Hori T.; Takakura K. *Magn. Reson. Med. Sci.* 2005, 4, 129-136.
10. Apuzzo ML.; Sabshin JK. *Neurosurgery* 1983, 12, 277-285,
11. Barnett G. K.; Kormos D. W.; Steiner C. P.; Weisenberger J. *Neurosurg.* 1993, 33, 674-678.
12. Dorward N. L.; Alberti O.; Velani B.; Gerritsen F. A.; Harkness W. F.; Kitchen N. D.; Thomas D. G. J. *Neurosurg.* 1998, 88, 656-662.
13. Roberts D. W.; Hartov A.; Kennedy F. E.; Miga M. I.; Paulsen K. D. *Neurosurgery* 1998, 43, 749-760.
14. Nijssen A.; Bakker Schut T. C.; Heule F.; Caspers P. J.; Hayes D. P.; Neumann M. H.; Puppels G. J. J. *Invest. Dermatol.* 2002, 119, 64-69.
15. Stone N.; Kendall C.; Shepherd N.; Crow P.; Barr H. *Journal of Raman spectroscopy.* 2002, 33, 564-573.
16. Boustany N. N.; Crawford J. M.; Manoharan R.; Dasari R. R.; Feld M. S. *Lab. Invest.* 1999, 79,1201-1214.
17. Mizuno A.; Hayashi T.; Tashibu K.; Maraishi S.; Kawauchi K.; Ozaki Y. *Neurosci. Lett.* 1992, 141, 47-52.
18. Mizuno A.; Kitajima H.; Kawauchi K.; Muraishi S.; Ozaki Y. *Journal of Raman spectroscopy.* 1994, 25, 25-29.
19. Wolthuis R.; van Aken M.; Fountas K.; Robinson Jr. J. S.; Bruining H. A.; Puppels G. J. *Anal. Chem.* 2001, 73, 3915-3920.
20. Koljenović S.; Choo-Smith L-P.; Bakker Schut T. C.; Kros J. M.; van den Berge H. J.; Puppels G. J. *Lab. Invest.* 2002; 82, 1265-1277.
21. Koljenović S.; Bakker Schut T. C.; Vincent A.; Kros J. M.; Puppels G. J. *Anal. Chem.* 2005, 77, 7958-7965.
22. Krafft C.; Neudert L.; Simat T.; Salzer R. *Spectrochim. Acta Part A* 61, 2005, 1529-1535.
23. Mahadevan-Jansen A.; Mitchell M. F.; Ramanujam N.; Utzinger U.; Richards-Kortum R. *Photochem. Photobiol.* 1998, 68, 427-431.
24. Buschman R.; Marple E. T.; Wach M.L.; Bennett B.; Bakker Schut T. C.; Bruining H. A.; Bruschke A. V.; van der Laarse A.; Puppels G. J. *Anal. Chem.* 2000, 72, 3771-3775.
25. Bakker Schut T. C.; Witjes M. J. H.; Sterenborg H. J. C.; Speelman O. C.; Roodenburg J. L. N.; Marple E. T.; Bruining H. A.; Puppels G. P. *Anal. Chem.* 2000, 72, 6010-6018.

26. Huang Z.; McWilliams A.; Lui H.; McLean D.; Lam D. I. S.; Zeng H. *Int. J. Cancer*. 2003, 107, 1047-1052.
27. Molckovsky A.; Wong Kee Song L-M.; Shim M. G.; Marcon N. E.; Wilson B. C. *Gastrointest. Endosc.* 2003, 57, 396-402.
28. Puppels G. J.; van Aken M.; Wolthuis R.; Caspers P.J.; Bakker Schut T. C.; Bruining H. A.; Römer T. J.; Buschman H. P. J.; Wach M.; Robinson J. S. *In vivo tissue characterization by Raman spectroscopy*. Proc SPIE conference proceedings vol. 3257; Mantsch H. H., Jackson M., Katzir A., Eds.; Washington, 1998, 78 – 85.
29. Shim M. G.; Song L. M.; Marcon N. E.; Wilson B. C. *Photochem. Photobiol.* 2000, 72, 146–150.
30. Motz J. T.; Hunter M.; Galindo L. H.; Gradecki J. A.; Kramer J. R.; Dasari R. R.; Feld M. S. *Appl. Opt.* 2004, 20, 542–554.
31. Santos L. F.; Wolthuis R.; Koljenović S.; Almeida R. M.; G. J. Puppels. *Anal. Chem.* 2005, 77, 6747-6752.
32. Caspers P. J.; Lucassen G. W.; Carter E. A.; Bruining H. A.; Puppels G. J. *J. Invest. Dermatol.* 2001, 116, 434-442.
33. S. W. E van de Poll, A. Moelker, R. Wolthuis, T. C. Bakker Schut, S. Koljenović, A. van der Laarse and G. J. Puppels. Thesis 2003, Leiden, Netherlands.
34. Koljenović S.; Bakker Schut T. C.; Wolthuis R.; de Jong B.; Santos L.; Caspers P. J.; Kros J. M.; Puppels G. J. *J. Biomed. Opt.* 2005, 10, 031116.
35. Wolthuis R.; Bakker Schut T. C.; Caspers P. J.; Buschman H. P.; Römer T. J.; Bruining H. A.; Puppels G. J. In: *Fluorescent and luminescent probes for biological activity*; Mason W. T., Ed.; Academic Press: London, 1999; Chapter 32.
36. Martens H.; Stark E. J. *Pharm. Biomed. Anal.* 1991, 9, 625-635.
37. Agranoff B. W.; Benjamins J. A.; Hajra A. K. In: *Basic Neurochemistry*; Siegel G. J., Agranoff B. W., Albers R. W., Fisher S. K., Uhler M. D., Eds.; Lippincott Williams & Wilkins: Philadelphia, 1999, 47-69.
38. Tu A. T. *Basic concept and elementary theory: Raman spectroscopy in biology*. John Wiley & Sons: New York, 1982.
39. Thomas Jr, G. J. *Biopol.* 2002, 67, 214 – 225.
40. Haines D. E. In: *Fundamental Neuroscience*, Haines D.E., Editor; Churchill Livingstone: New York, 1997, 1 – 8.
41. Puppels G. J.; Bakker Schut T. C.; Caspers P. J.; Wolthuis R.; van Aken M.; van der Laarse A.; Bruining H. A.; Buschman H.; Shim M. G.; Wilson B. C. In: *"Handbook for Raman spectroscopy"*; Lewis I. R. and Edwards H. G. M., Eds.; Marcel Dekker, Inc: New York, 2001, 549-574.
42. Boere I. A.; Bakker Schut T. C.; van den Boogert J.; de Bruin R. W. F.; Puppels G. J. *Vib. Spectrosc.* 2003, 32, 47 – 55.



**Summary and  
General Discussion**

**Samenvatting en  
Algemene Discussie**

**Sažetak i Diskusija**

8



In this thesis Raman spectroscopy is presented as a novel tool for real-time guidance of diagnostic and therapeutic procedures. The method provides detailed information about the biochemical composition of cells/ tissues. Although the Raman effect was observed in 1928, it was not applied for high resolution studies at the level of a single cell until the early 1990's when Puppels *et al.* developed a highly sensitive confocal Raman micro-spectrometer.<sup>1</sup> Over the last years efforts in applying Raman spectroscopy for clinico-pathological applications have been made. In many studies spectral differences between normal and diseased tissues were reported, enabling the detection of cancers of various organs/ tissues (e.g. cervix, esophagus, larynx, oral cavity) and their precursor lesions.<sup>2-7</sup> Raman spectroscopy is a highly suitable technique for *in vivo* applications as it is non-destructive, does not require the use of labels or other contrast enhancing agents. The feasibility of *in vivo* Raman spectroscopy has been proven in a number of recent articles.<sup>8-10</sup> In this thesis we describe our initial efforts in developing an *in vivo* Raman method for real-time guidance of clinical procedures. At first, *in vitro* studies of various normal and diseased tissues were performed by means of Raman mapping experiments (Chapters 2, 3, 4 and 5). By correlating Raman spectral maps with histology of the same tissue sections, we were able to identify the morphological origins of specific spectral features. The *in vitro* results served as basis for the construction of a Raman spectroscopic device for *in vivo* clinical application (Chapters 6 and 7).

### *Characterization of Normal Tissues: The Basis for the Identification of Pathological Changes*

The characterization of the biochemical composition of normal tissues is a prerequisite for the identification of the changes accompanying the histomorphological changes that occur with disease. In Chapter 2 the *in situ* analysis of normal bronchial tissue is described. We have studied tissue samples that were snap-frozen directly after collection and performed the Raman analysis without any preceding processing (e.g. dyes, labels). Raman mapping experiments were performed and directly compared with the histology of the tissue sections. By precise linking of spectral features with the histological structure data about the (differences in) molecular composition of bronchial mucus and bronchial wall structures were revealed. The results are promising and assist Raman spectroscopy in becoming an important tool in the identification of pathological changes in the tissues. An illustration of the superiority of this approach is the straightforward way in which the main composition and source of the bronchial mucus could be analyzed. The uncertainty whether the sample that is being analyzed is representative of bronchial mucus is removed by *in situ* analysis of unfixed tissues. Other approaches to studying the composition of bronchial secretion, such as those on material obtained after tracheotomy, tracheal aspirates, bronchopulmonary washings, sputum, surgically removed bronchogenic cysts and secreting cell cultures are obstructed by potential contamination of the sample by alveolar components or sputum.<sup>11,12</sup> However, in various studies it has been suggested that in diseases such as chronic bronchi-

tis, asthma and cystic fibrosis, the bronchial hypersecretion is accompanied by changes in biochemical composition of bronchial mucus.<sup>13-15</sup> Similarly, the presence of (pre-) malignant tissue may affect the formation and/or composition of the bronchial mucus. These are topics of continued research efforts in this area. We expect that in future *in vivo* measurements by means of fiber optics the tissue volumes from which signal is collected will be much larger than in the present study. This implies that several different tissue layers and structures will contribute to the Raman signal. The detailed information gathered in this study may become valuable for the interpretation of such spectra. Similar studies on the pathological changes of bronchial tissue (i.e. malignancies and pre-malignancies) will contribute to a solid basis for the development of the diagnostic applications of Raman spectroscopy.

### *Discrimination of Tumor Tissue from Normal Tissue: The Assessment of Resection Margins*

Complete resection is the treatment of choice for many tumors. An example is meningioma, which is predominantly benign but often recurs due to its incomplete surgical removal. Fifteen-year recurrence rates of over 30% have been observed after complete resections of meningiomas.<sup>16</sup> Complete resection is of great importance as incompletely removed meningiomas may recur as high-grade tumors. In a classic paper by Simpson in 1950 it was postulated that residual nests of meningioma within the regional meninges, within clear defined margins, would be mainly responsible for recurrent tumor.<sup>17</sup> This view was confirmed in later studies.<sup>18,19</sup> So far, no objective per-operative tools are available to verify whether all tumor tissue present in marginal dura-arachnoid is radically removed. Chapter 3 describes a mapping study using Raman spectroscopy on frozen sections of human dura and meningioma tissues. The results show that meningiomas and dura-arachnoid without tumor are distinguished by their Raman spectra. The obvious differences between the Raman spectra of dura-arachnoid and meningioma are caused by the high collagen content of dura, and the increased lipid content of the tumor. A classification model for dura and tumor tissue based on Linear Discriminant Analysis of Raman spectra yielded an accuracy of 100%. An analysis was performed to estimate the minimum amount of tumor tissue in a measurement volume that is still detected within the dura. A Partial Least Squares model showed that the relative amount of meningioma in a mixed meningioma-dura sample is determined with an accuracy of about 13%. These preliminary results serve as proof-of-principle for the development of an *in vivo* Raman spectroscopic method for the real-time guidance of meningioma resection margins in order to detect residual tumor within the dura-arachnoid during surgery and thus reduce recurrence rates of this tumor.

### *Classification of Tumor Heterogeneity: Biopsy Guidance for Optimal Tissue Sampling*

Diagnostic and surgical procedures are currently supported by computed tomography (CT) or magnetic resonance imaging (MRI) guidance. These techniques generally provide

limited clues about the histological composition of tissues. These systems do not provide information about the dynamic changes that occur during the surgical procedures (e.g. brain shift due to edema, tissue removal to make way for taking the target tissue or loss of cerebrospinal fluid). Such changes in local anatomy may impair the precise targeting of lesions. In addition, it may well increase the risk of damaging vital areas that may result in functional impairment.<sup>20-34</sup> Intra-operative MR imaging technology has been put forward as a powerful tool for imaging during neurosurgical procedures.<sup>20-28</sup> However, efficient use of an intra-operative MRI unit is held up because of the need for MR-compatible instruments and radiofrequency-shielded operating rooms. In addition, the costs and sizes of intra-operative MRI systems are considerable.<sup>28</sup> The problem of sampling error during biopsies is addressed by an *in vitro* Raman spectroscopic mapping study on glioblastoma (Chapter 4). The histological malignancy grade of gliomas depends on the presence of parameters such as endothelial proliferation and necrosis, which are often not evenly distributed within the tumor. Because tissue samples obtained by stereotactic surgery are relatively small, sampling errors may easily occur by missing these crucial features. For instance, the feature of necrosis is important for grading gliomas, but specimens containing necrosis only are diagnostically useless, because viable tissue is necessary for the diagnosis. Therefore, one wishes to avoid biopsy samples consisting purely of necrosis. The results of the Raman spectroscopic mapping study indicated that the biochemical information offered by Raman spectra enables to distinguish necrotic tissue from viable glioblastoma tissue. The Linear Discriminant Analysis prediction model that was developed in this *in vitro* study, with still a relatively low number of samples, enabled the distinction of vital glioma and necrotic tissue with a 100%-accuracy. The biochemical differences between necrotic and vital glioblastoma, as revealed by Raman spectroscopy, are in accordance with literature reports<sup>35-44</sup> and add information about the histological origin of these differences. The results herald the development of an *in vivo* Raman spectroscopic method for improving intraoperative, real-time brain biopsy guidance. Biopsy target selection by Raman spectroscopy may substantially influence the histopathological diagnosis, which is essential for treatment selection and prognosis of gliomas. Although complications following a stereotactic brain biopsy procedure are infrequent, the procedure is not entirely without risk (e.g. hemorrhage or damage of structures) for the patient.<sup>45</sup> The application of Raman guided biopsies may decrease the number of non-informative stereotactic biopsies. In addition, the application will be helpful in distinguishing areas of radiation necrosis from viable tumor in glioma patients with tumor recurrence who underwent radiation therapy.

### *Optimizing Raman Spectroscopy for In Vivo Use: Development of a Single Fiber-Optic Probe Setup*

Although various miniaturized fiber-optic probes have been designed,<sup>46-48</sup> the actual implementation of conventional Raman spectroscopy for *in vivo* clinical purposes was hindered

for a long time. This is due to the fact that Raman fiber-optic probes were rather complicated and difficult to create in such a way as to obtain reproducible results. The problem is that a strong background Raman signal is generated in the optical fibers themselves. Unfortunately, probes equipped to eliminate background signal are complex, rigid and/or difficult to miniaturize. Moreover, signal intensity in the so-called fingerprint region ( $400\text{--}2000\text{ cm}^{-1}$ ) is relatively low, necessitating long signal integration times which are impractical for clinical use.

The final chapters of this thesis describe our efforts towards development of small and flexible fiber-optic probes for obtaining Raman spectra from tissues *in vivo*. The solution we have explored was to use the high wave number (HWVN) region ( $2000\text{--}4000\text{ cm}^{-1}$ ) of Raman spectrum. Interestingly, in this spectral region little or no background signal is generated within the probe. This allows a very simple design of fiber-optic probes. Previously, HWVN region was used by Wolthuis *et al.* and by Caspers *et al.* to determine the water concentration in brain tissue<sup>49</sup> and in skin<sup>50</sup>, respectively. Van de Poll *et al.* obtained very detailed information about the composition and heterogeneity of atherosclerotic plaque obtained by using only the  $2400\text{--}3800\text{ cm}^{-1}$  region of its Raman spectrum.<sup>51</sup>

In the work described here (Chapter 5) we investigated whether HWVN Raman spectroscopy is able to provide sufficient information for the discrimination between various histological structures in a variety of tissues (glioblastoma, meningioma and normal bladder tissue) as compared with the fingerprint region. The Raman mapping experiments that were performed using fingerprint and HWVN spectral region were compared with each other. It was shown that in many cases HWVN Raman spectroscopy attains the same level of discrimination between different types of tissue, and provides the same relevant information as Raman spectroscopy in the fingerprint region. These results are important in regard to our goal to miniaturize fiber-optic probes necessary for intravascular use<sup>8,46</sup> or intra-cerebral use (i.e. stereotactic brain biopsy) with reproducible performance.<sup>52</sup> It is essential to keep probes flexible when using them in the auxiliary channel of an endoscope.<sup>10</sup> It is also necessary to enable the production of such probes for use as disposables. To date, small and flexible fiber-optic Raman probes have not been commercially available. We have developed a setup for remote Raman spectroscopic tissue characterization in the HWVN region (Chapter 6). A single, unfiltered, optical fiber is used to guide laser light to the sample and to collect scattered light and guide it to a spectrometer. Several optical fibers were tested for Raman background signal. Although the compositions of core and cladding are primarily responsible for the performance of an optical fiber, different coating materials were also analyzed since they can influence overall behavior of the fiber. The fused silica optical fiber with an acrylate coating proved to be the best performing combination.

Raman fiber-optic setup was tested *ex vivo* on fresh porcine brain. So far, no studies have been published using a single fiber Raman probe for characterization of tissues (Chapter 7). The results of this study show that the biochemical information represented in Raman

spectra enables the identification of distinct brain structures. We used Hierarchical Cluster Analysis to obtain information about the dissimilarity between spectra of the various brain regions. This resulted in a clear separation of adjacent brain structures based on the spectra obtained from all brains studied. The biochemical differences represented by the Raman spectra were analyzed by a *least squares fitting* procedure. The Raman spectra from white and grey matter show large differences, representing the variation in their molecular composition. Compared with white matter, Raman spectra of grey matter are characterized by stronger signal contributions from protein, DNA and phosphatidylcholine. This can be explained by the fact that grey matter is composed of neuronal cell bodies.<sup>53</sup> The lipids such as cholesterol, sphingomyelin and galactocerebroside are the most prominent features in the spectra obtained from white matter. This was expected since white matter consists of abundant myelin. Myelin is a lipoprotein consisting of 70 to 85% lipid.<sup>54</sup> The Raman spectra from distinct white matter areas (e.g. fimbria hippocampi and tractus opticus, cerebrum- and cerebellum white matter) could be consistently separated for all brains by HCA, despite the small spectral differences. Detailed analysis showed that these differences were the result of variation in their lipid signal contributions, which probably reflects the differences in the level of myelinization. Furthermore, a number of grey matter areas (e.g. various basal nuclei) were separated from each other for all brains, based on the different signal contributions of proteins and lipids. This is most probably due to the amount of myelinated fibers that pass through the grey matter areas.<sup>53</sup> For the smaller and/or thinner brain structures (e.g. nucleus ruber, substantia nigra, tractus opticus), the accuracy of the Raman measurements are hindered by the effective measurement volume of the probe. A systematic study of probe measurement volume in brain tissue has not been performed yet. It is likely that for the smaller structures some signal was also collected from adjacent brain structures, either by inaccurate positioning of the probe or by effective measurement volume extending beyond the targeted brain structure. The biochemical differences between small adjacent structures are sub-optimally probed, and lead to misclassifications. This problem needs to be investigated in more detail in future studies. The fiber core size and numerical aperture are means of controlling the measurement volume of a single fiber probe to a certain extent, but tissue scattering properties also play an important role. The results show that the combination of a single fiber-optic probe and the use of the HWVN part of the spectrum provide a potential and easy-to-use *in vivo* Raman system that enables to discriminate between the various brain structures.

So far, the probes used in this study have been bare fibers which have not been optimized for depth resolution or collection efficiency. By optimizing the probes and the spectrometer it will become possible to reduce the time necessary to obtain a spectrum suitable for tissue discrimination to subsecond levels. The laser power applied in the current experiments can safely be applied during brain surgery. The temperature increase in brain tissue as a

result of irradiation with laser light of 830 nm up to 250 mW is in the order of  $\sim 2$  °C, as we have shown in a previous study.<sup>55</sup> Moreover, improvements in the sensitivity of the instrumentation will enable signal collection with even lower laser power than used in this work. Additionally, earlier Raman spectroscopic studies, using a fiber-optic probe have already shown that real-time interpretation of *in vivo* spectra in these time frames is possible.<sup>52</sup> Recently, Nijssen *et al.* have made a crucial step in the development of clinical applications based on fiber-optic Raman spectroscopy in the dermatological practice.<sup>56</sup> A HWVN Raman setup described in this thesis appears to be able to discriminate between basal cell carcinoma (BCC) and normal skin. A Linear Discriminant Analysis-based tissue classification model was developed discriminating between BCC and noninvolved skin with high accuracy. Other applications of *in vivo* fiber-optic Raman spectroscopy that can be envisioned include: Raman-guided biopsy during endoscopy procedures to improve targeting potential areas of dysplasia; Raman-guided laparoscopy to facilitate the identification of tissues and anatomical sites; guiding fine needle aspiration for cytological investigation of suspected malignancies; assistance in onco-surgical procedures for real-time assesment of tumor metastasis in lymph nodes or involvement of neighbouring organs/ tissues; monitoring the effects of local and systemic therapies (e.g. radiotherapy and chemotherapy); intravascular detection and characterization of atherosclerotic plaques.

In conclusion, we have performed pioneer work in the developement of *in vivo* Raman spectroscopic method for applications in clinical practice. Raman spectral characterization of normal tissues like the bronchial tissue and porcine brains is necessary to build datasets to be used for comparison with the spectra of abnormal tissues. We characterized some specific biochemical differnces in healthy tissues and tumor tissues. Meningioma was discerned from normal dura-arachnoid and within glioblastoma tissue sections we were able to discriminate necrosis from viable tumor. The meningioma spectra served to delineate normal from tumor-involved dura-arachnoid, whereas the discrimination of the components of a glioblastoma sample was intended to obtain clues to informative tissue in a biopsy procedure. The promising results of the various experiments described in this thesis merit robust follow-up: the application of Raman spectroscopy may soon become an important addition to the clinical practice in terms of increasing the sensitivity and specificity of making pathological diagnosis.

## Samenvatting en algemene discussie

In dit proefschrift wordt Raman spectroscopie gepresenteerd als een relatief nieuwe techniek die behulpzaam kan zijn bij medisch diagnostische en therapeutische ingrepen. De Raman techniek verschaft nauwkeurige informatie over de biochemische samenstelling van weefsels en cellen. Het Raman effect is al in 1928 beschreven maar werd pas gebruikt voor praktisch onderzoek op cellulair niveau toen Puppels *et al.* rond 1990 de confocale Raman microspectrometer ontwikkelden.<sup>1</sup> De laatste jaren zijn er in de literatuur een aantal publicaties verschenen over de mogelijkheden van het gebruik van Raman spectroscopie bij klinisch-pathologisch onderzoek. Er verschenen publicaties over spectrale verschillen tussen normaal en ziek weefsel, waarbij maligne of premaligne weefselveranderingen konden worden vastgesteld in de cervix, oesofagus, larynx, en mondholte.<sup>2-7</sup> Raman spectroscopie is zeer geschikt voor *in vivo* onderzoek, omdat deze techniek niet destructief is en geen contrast verhogende agentia nodig heeft. De toepasbaarheid van Raman spectroscopie bij *in vivo* onderzoek is al in een aantal artikelen vermeld.<sup>8-10</sup>

Het in dit proefschrift beschreven onderzoek richt zich op de ontwikkeling van een *in vivo* Raman methode voor “real-time” begeleiding van klinische ingrepen. Eerst wordt *in vitro* onderzoek gedaan om Raman spectra van verschillende normale en zieke weefsels in kaart te brengen (Hoofdstuk 2, 3, 4 en 5). Door spectrale beelden te correleren met de histologie van dezelfde weefselcoupes konden wij de morfologische herkomst identificeren van de specifieke spectrale karakteristieken. Deze *in vitro* resultaten dienden als basis voor het ontwikkelen van een nieuwe Raman spectroscopische opstelling voor *in vivo* klinische toepassing (Hoofdstuk 6 en 7).

### *Karakterisering van normale weefsels: de basis voor de identificatie van pathologische veranderingen*

Karakterisering van de biochemische samenstelling van normale weefsels is een noodzakelijke voorwaarde voor de identificatie van histomorfologische veranderingen welke gepaard gaan met ziekte. In Hoofdstuk 2 wordt de *in situ* analyse van normaal bronchusweefsel beschreven. De weefselsamples werden direct na afname ingevroren en gebruikt voor Raman analyse. Hierbij werd geen fixatief of kleurstof gebruikt. Door de spectrale kenmerken te koppelen aan histologische structuren werd informatie verkregen over de moleculaire samenstelling van bronchusslijm enerzijds en verschillende structuren van bronchuswand anderzijds. De resultaten zijn veelbelovend en steunen de veronderstelling dat Raman spectroscopie een belangrijk middel kan worden voor het opsporen van pathologische veranderingen in weefsels. Een illustratie van de kracht van deze benadering is de rechtstreekse manier waarmee de samenstelling en origine van het bronchusslijm kon worden bestudeerd. Doordat *in situ* analyse werd gedaan op niet gefixeerde weefselmonsters was er geen contaminatie met mond/ keelslijm of slijm afkomstig uit de long; dit in tegenstelling

tot andere studies die gebruik maakten o.a. van tracheale aspiraten, broncho-pulmonaire spoelingen, sputum en celkweken.<sup>11</sup> In verschillende studies werd verondersteld dat ziektes zoals chronische bronchitis, astma en cystische fibrose, bronchiale hypersecretie gepaard met veranderingen in de biochemische samenstelling van bronchusslijm.<sup>13-15</sup> Ook premaligne en maligne aandoeningen zouden hun invloed kunnen hebben op de compositie van het slijm. Derhalve is analyse van bronchusslijm interessant en lijkt Raman spectroscopie een ideale techniek daarvoor. We verwachten dat bij toekomstige *in vivo* metingen middels optische vezels, weefselvolumes waarvan signaal is verzameld veel ruimer zullen zijn dan in de huidige studie. Het betekent dat meerdere weefsellagen en -structuren zullen bijdragen aan het Raman signaal, en dus in de analyse kunnen worden betrokken. De gedetailleerde informatie van onze studie is een waardevolle eerste stap naar de interpretatie van *in vivo* spectra. Vergelijkbare studies naar pathologische veranderingen van bronchusweefsel (maligniteiten en premaligniteiten) zullen bijdragen aan het ontwikkelen van diagnostische toepassingen van Raman spectroscopie.

### *Onderscheid tussen tumorweefsel en normaal weefsel: het bepalen van resectieranden*

Complete verwijdering is de voorkeursbehandeling voor veel tumoren. Een voorbeeld is het meningeoom, een tumor van de hersenvliezen, die zich meestal goedaardig gedraagt maar lokaal kan recidiveren indien niet radicaal verwijderd. Recidief percentages van meer dan 30% binnen 15 jaar na de operatie zijn beschreven.<sup>16</sup> Tumorrecidieven zijn vaak niet meer goedaardig maar van hogere maligniteitsgraad. In 1950 veronderstelde Simpson dat overgebleven nesten van meningiomen in de regionale hersenvliezen verantwoordelijk zouden zijn voor tumorrecidieven.<sup>17</sup> Deze hypothese werd later bevestigd door de andere auteurs.<sup>18,19</sup> Tot nu toe bestaat er geen manier om per-operatief uit te maken of al het meningeoomweefsel uit de omgevende hersenvliezen is verwijderd. Hoofdstuk 3 beschrijft een Raman spectroscopische studie op vriescoupes van humane dura en meningeoomweefsel. Raman spectra gaven een duidelijk verschil te zien tussen het tumorweefsel en de hersenvliezen zonder tumor. Deze verschillen konden worden herleid tot verschillen in de bestanddelen zoals relatief meer collageen in de hersenvliezen en relatief veel vetten in het tumorweefsel. Een classificatiemodel voor dura en tumorweefsel gebaseerd op Lineaire Discriminant Analyse van de Raman spectra leverde een nauwkeurigheid op van 100%. Voorts werd een analyse gedaan om de minimum hoeveelheid tumor vast te stellen die nog detecteerbaar was in de dura. Deze voorlopige resultaten kunnen worden gebruikt als basis voor het ontwikkelen van een *in vivo* Raman spectroscopische methode om per-operatief resectieranden van hersenvliezen te onderzoeken en zodoende de recidiefkans te verkleinen.

### *Classificatie van tumor heterogeniteit: geleiding van de biopsie voor optimale weefselmonster afname*

Diagnostische en chirurgische ingrepen worden ondersteund en begeleid door de gecomputeriseerde tomografie (CT) en magnetische resonantie afbeelding (MRI). Deze technieken geven in het algemeen maar een beperkt inzicht in de histologische samenstelling van de betrokken weefsels. Ook verschaffen zij geen informatie over de veranderingen die tijdens de operatie plaatsvinden (zoals bijvoorbeeld verschuiving van het brein, veroorzaakt door oedeem of als gevolg van het verwijderen van regionale weefsels). Deze veranderingen in de lokale anatomie kunnen de nauwkeurigheid van de chirurgische ingreep bemoeilijken waardoor risico bestaat op beschadiging van gezonde weefsels.<sup>20-34</sup> Intra-operatieve MRI technologie wordt gepresenteerd als een effectieve techniek voor afbeelding tijdens neurochirurgische operaties.<sup>20-28</sup> Echter, efficiënt gebruik van een intra-operatieve “MRI unit” wordt tegengehouden door de noodzaak MRI-verenigbare instrumenten en radiofrequentie-beveiligde operatiekamers te gebruiken. Daarbij zijn de afmetingen, en ook de kosten, van zulke systemen aanzienlijk.<sup>28</sup>

Het probleem bij het afnemen van een weefselbiopsie voor pathologisch-diagnostische doeleinden wordt behandeld in een *in vitro* Raman spectroscopische mapping studie van het glioblastoom (Hoofdstuk 4). De histologische maligniteitsgraad van het glioom is afhankelijk van verschillende weefselveranderingen zoals endotheel proliferatie en necrose, welke vaak onregelmatig verspreid zijn in de tumor. Omdat stereotactisch verkregen biopsen relatief klein zijn, kunnen voor de diagnostiek essentiële tumorweefselveranderingen gemakkelijk gemist worden. Necrose is bijvoorbeeld belangrijk voor het graderen van de tumor, maar op een biopsie dat puur uit necrotisch weefsel bestaat kan geen classificerende diagnose worden gesteld en moet de biopsie worden herhaald.

De resultaten van deze studie laten zien dat Raman spectra de biochemische informatie bevatten die het onderscheid van necrotisch weefsel en vitaal glioblastoomweefsel mogelijk maakt. Het Lineaire Discriminant Analyse predictie model dat werd ontwikkeld in deze *in vitro* studie gaf een onderscheid tussen vitaal glioblastoomweefsel en necrotisch weefsel met 100% nauwkeurigheid. De biochemische verschillen tussen necrotisch en vitaal tumorweefsel zoals verkregen door Raman spectra zijn in overeenstemming met de literatuur<sup>35-44</sup> en voegen informatie toe over de histologische origine van deze verschillen. Deze resultaten kunnen worden gezien als een voortraject bij het ontwikkelen van een *in vivo* Raman spectroscopische methode bij de intra-operatieve geleiding van hersenbiopsie. Doordat Raman spectroscopie precisie biedt bij selectie van een weefsel voor de histopathologische evaluatie, kan deze techniek een substantiële bijdrage leveren aan de diagnose, welke op zijn beurt essentieel is voor de therapiekeuze en prognose van gliomen. Hoewel complicaties ontstaan na stereotactische hersenbiopsieën zeldzaam zijn, is de ingreep toch niet geheel zonder risico voor de patiënt (b.v. bloedingen of schade aan gezonde weefsels).<sup>45</sup> Toepassen van Raman spectroscopische geleiding kan het aantal niet-informatieve stereotactische

biopsieën reduceren. Daarnaast, kan deze methode bruikbaar zijn voor het maken van onderscheid tussen gebieden met radiatie necrose en vitaal tumorweefsel bij patiënten met glioomrecidief die radiotherapie ondergaan.

### *Optimalisering van Raman spectroscopie voor in vivo toepassingen: ontwikkelen van een eenvoudige optische glasvezel “probe”*

Hoewel verschillende geminimaliseerde optische glasvezel probes zijn ontworpen<sup>46-48</sup> is tot nu toe de werkelijke implementatie van Raman spectroscopie voor *in vivo* gebruik in de klinische setting nog niet goed van de grond gekomen. Dit hing samen met het feit dat Raman probes nogal ingewikkelde ontwerpen waren en het moeilijk was om met verschillende probes reproduceerbare resultaten te krijgen. Het probleem hierbij is dat de optische glasvezels zelf een sterk Raman achtergrond signaal genereren. Probes uitgerust om dit achtergrond signaal te elimineren zijn complex, dik en star. Bovendien is de signaalintensiteit in het zogenaamde fingerprint gedeelte van het Raman spectrum ( $400\text{--}2000\text{ cm}^{-1}$ ) relatief laag, waardoor langere meettijden nodig zijn. Dit is onpractisch bij gebruik in de klinische setting.

De laatste hoofdstukken van dit proefschrift beschrijven onze inspanningen om dunne en flexibele glasvezel probes te ontwerpen waarmee Raman spectra van weefsels *in vivo* gemeten kunnen worden. De oplossing die we hiervoor hebben gevonden was om gebruik te maken van het “high wavenumber” gebied (HWVN) van het Raman spectrum ( $2000\text{--}4000\text{ cm}^{-1}$ ). Interessant is dat in dit spectraal gebied weinig of geen achtergrond signaal wordt generaliseerd in de optische vezels. Dit maakte een eenvoudig optische vezel probe ontwerp mogelijk. Het HWVN gebied werd al eerder gebruikt door Wolthuis *et al.* en door Caspers *et al.* om de waterconcentratie te bepalen in respectievelijk hersenweefsel en huid.<sup>49,50</sup> Ook van der Poll *et al.* verkregen zeer gedetailleerde informatie over de samenstelling en heterogeniteit van atherosclerotische plaques door alleen het  $2400\text{--}3800\text{ cm}^{-1}$  gebied van het Raman spectrum te gebruiken.<sup>51</sup>

In het werk dat in Hoofdstuk 5 wordt beschreven onderzochten we eerst of HWVN Raman spectroscopie voldoende informatie kon verschaffen om verschillende histologische structuren in verschillende weefsels te onderscheiden (glioblastoom, meningeoom, normaal blaasweefsel) in vergelijking met het fingerprint gebied. De Raman mapping experimenten werden uitgevoerd in beide spectrale gebieden en vergeleken met elkaar. Uit dit onderzoek bleek dat in het HWVN gebied dezelfde onderscheidsniveaus tussen de verschillende weefsels konden worden bereikt en dezelfde relevante gegevens konden worden verkregen als in het fingerprint gebied. Deze resultaten waren gunstig met betrekking tot ons doel om geminiaturiseerde flexibele optische glasvezel probes te ontwikkelen geschikt voor o.a. intravasculair gebruik<sup>8,46</sup> of intra-cerebraal gebruik (b.v. stereotactische hersenbiopsie n).<sup>52</sup> Het is daarbij essentieel om de probes flexibel te maken zodat ze bijvoorbeeld ook in een endoscoop kunnen worden geplaatst.<sup>10</sup> Het is ook nodig dat probes als “disposables” kun-

nen worden gebruikt. Tot op heden waren dunne en flexibele probes niet commercieel verkrijgbaar. Wij hebben daarom een opstelling gemaakt voor Raman spectroscopische weefsel karakterisering in het HWVN gebied waarbij een enkele, niet gefilterde optische glasvezel werd gebruikt zowel om het laserlicht naar het weefsel te leiden als om het teruggekaatste licht op te vangen en naar de spectrometer te voeren (Hoofdstuk 6). Een aantal glasvezel-typen werd getest op achtergrondsignaal. Uitgezocht werd welke samenstelling van glasvezel en de coating ervan het beste resultaat gaf. Een glasvezelkern van gefuseerde silica met een acrylaat-coating bleek de beste combinatie.

Deze Raman fiber-optische HWVN opstelling werd vervolgens *ex vivo* uitgetest op verse varkenshersenen (Hoofdstuk 7). De resultaten van dit onderzoek toonden aan dat met deze opstelling een duidelijk onderscheid kan worden gemaakt tussen de verschillende hersengebieden, samenhangend met verschillen in hun biochemische samenstelling. Hiërarchische Cluster Analyse werd gebruikt om informatie te verkrijgen over verschillen tussen de spectra van verschillende hersengebieden. De in de Raman spectra aanwezige biochemische verschillen werden geanalyseerd met behulp van “*least squares fitting procedure*”. De Raman spectra van grijze en witte stof verschilden sterk van elkaar hetgeen terug te voeren is tot verschillen in hun biochemische samenstelling. Raman spectra van grijze stof werden gekarakteriseerd door sterke signaal bijdrage van eiwitten, DNA en phosphatidylcholine wat verklaard kan worden aan de hand van het feit dat de grijze stof voor een groot deel uit neuronale cellen bestaat.<sup>53</sup> In de spectra van witte stof kwam het meest prominente signaal van lipiden zoals cholesterol, sphingomyeline en galactocerebroside. Dit was te verwachten omdat witte stof grote hoeveelheden myeline bevat, een lipoproteïne dat voor 70%-85% uit lipiden bestaat.<sup>54</sup> Hoewel de spectrale verschillen tussen de verschillende witte stof gebieden onderling (b.v. fimbria hippocampi en tractus opticus, witte stof van grote- en kleine hersenen) klein waren, konden deze gebieden toch goed onderscheiden worden van elkaar. Gedetailleerde analyse liet zien dat deze verschillen werden veroorzaakt door variatie in de signaal bijdrage van lipiden, waarschijnlijk samenhangend met de verschillende mate van myelinisatie van deze witte stof gebieden. Daarnaast werd ook een aantal grijze stof gebieden (b.v. de basale kernen) van elkaar onderscheiden. Ook hier werden verschillen in de biochemische samenstelling gevonden, waarbij de verhouding van signaal bijdrage van eiwitten t.o.v. die van lipiden bepalend was. Dit is naar alle waarschijnlijkheid te verklaren door de hoeveelheid gemyeliniseerde vezels die door de grijze stof gebieden lopen.<sup>53</sup> De nauwkeurigheid van Raman metingen voor kleinere en dunnere hersenstructuren (b.v. de nucleus ruber, de substantia nigra of de tractus opticus) werd belemmerd door het effectieve meetvolume van de probe. Een systematische studie naar probe meetvolume in hersenweefsel is nog niet verricht. Het is waarschijnlijk dat voor kleinere structuren een deel van het signaal afkomstig is van naastgelegen structuren door inaccurate probe plaatsing of doordat het effectieve meetvolume groter was dan de te meten structuur. Dit probleem moet in de toekomst in meer detail worden onderzocht.

De resultaten laten zien dat het gebruik van een enkele optische vezel probe en het HWVN gebied van het spectrum een relatief makkelijk bruikbare en betrouwbare *in vivo* Raman-opstelling kan opleveren voor het maken van onderscheid tussen verschillende hersengebieden. Nijssen *et al.* hebben recent een belangrijke stap gezet in de ontwikkeling van klinisch-dermatologische toepassingen gebaseerd op fiber-optische Raman spectroscopie. Hierbij bleken zij, met de HWVN Raman opstelling zoals beschreven in dit proefschrift, in staat te zijn om met grote nauwkeurigheid basaalcelcarcinoom te onderscheiden van het omringende gezonde weefsel.<sup>56</sup> Toepassingen van *in vivo* fiber-optische Raman spectroscopie zullen ook gevonden kunnen worden in de geleiding van allerlei laparoscopische procedures, voor het opsporen van (pre)maligniteiten, het bepalen van therapie-effecten en de intravasculaire detectie van atherosclerotische plaques en de samenstelling ervan.

Deze thesis is de weerslag van onze inspanningen om Raman spectroscopie geschikt te maken voor zulke *in vivo* toepassingen in de klinische praktijk. Raman spectroscopie zal een waardevolle aanvulling worden voor de diagnostiek in de klinisch-pathologisch praktijk.

## Sažetak i Diskusija

U ovoj tezi, Ramanova spektroskopija predstavljena je kao relativno nova tehnika za upravljanje diagnostičkih i terapijskih podhvata. Ova metoda pruža detaljne informacije o biohemijском sastavu ćelija i tkiva. Premda je Ramanov efekat bio uočen još 1928. godine, on nije mogao biti primjenjen za visokorezolucione studije na nivou jedne ćelije sve do 90-tih godina prošloga stoljeća, kada su Puppels *et al.* konstruirali visokosenzitivni konfokalni Ramanov mikrospektrometar.<sup>1</sup> Tokom proteklih godina, radilo se na primjeni Ramanove spektroskopije u kliničko-patološke svrhe. U mnogim studijama zabilježene su spektralne razlike između zdravog i oboljelog tkiva, što omogućava otkrivanje kancera različitih organa i tkiva (npr. grlića materice, jednjaka, grkljana, usne duplje) i ostećenja koja im prethode. Ramanova spektroskopija je veoma pogodna tehnika za primjenu *in vivo* jer nije destruktivna, ne zahtijeva primjenu etiketa ili drugih kontrast-pojačnih agenasa i može se primjenjivati upotrebom tanke fiber-optičke sonde (engl. probe). Primjenjivost Ramanove spektroskopije *in vivo* dokazana je u brojnim novim člancima.<sup>8-10</sup> U ovoj tezi opisujemo naše početne napore u razvijanju *in vivo* Ramanove metode za navođenje kliničkih procedura. Najprije su obavljani *in vitro* eksperimenti na različitim normalnim i oboljelim tkivima pomoću takozvanih Ramanovih mapping eksperimenata (Poglavlja 2, 3, 4 i 5). Korelacijom Ramanovih spektralnih mapa sa histologijom istih tkivnih sekcija mogli smo identificirati morfološko porijeklo specifičnih spektralnih karakteristika. Ovi *in vitro* rezultati služili su kao osnov za konstruiranje Ramanovog spektroskopskog uređaja za kliničku primjenu *in vivo* (Poglavlja 6 i 7).

### Karakterizacija normalnih tkiva: osnova za identifikaciju patoloških promjena

Karakterizacija biohemijского sastava normalnih tkiva je preduvjet za identifikaciju promjena koje prate histopatološke promjene nastale sa bolešću. U poglavlju 2 opisana je *in situ* analiza normalnog bronhijalnog tkiva. Direktno nakon što su dobiveni, uzorci tkiva su bili zamrznuti i kao takvi bili korišteni za Ramanovu analizu bez ikakve prethodne obrade (npr. boje, fiksativi). Izvršeni su Ramanovi mapping eksperimenti i direktno upoređeni sa histologijom istog tkivnog isječka. Preciznim povezivanjem spektralnih karakteristika sa histološkim strukturama dobivene su informacije o molekularnom sastavu (i izvoru) bronhijalne sluzi kao i o različitim bronhijalnim strukturama. Rezultati su ohrabrujući i podržavaju pretpostavku da Ramanova spektroskopija može postati važna metoda u identifikaciji patoloških promjena u tkivima. Ilustracija preciznosti i valjanost ovakvog pristupa jeste jednostavan način na koji se mogu analizirati sastav i izvor bronhijalne sluzi. Zbog toga što je izvršena *in situ* analiza na nefiksiranom tkivu nije bilo kontaminacije sa florom iz usne duplje/ grla ili sa sluzi iz pluća, što je u protivnom slučaj kod ostalih pristupa koji između ostalih koriste dušničke aspirate, bronhopulmonalne ispirke, pljuvačku, ćelijske kulture. U raznim studijama je sugerirano da je u bolestima poput hroničnog bronhitisa,

astme i cistične fibroze bronhijalna hipersekrecija praćena promjenama biohemijskog sastava sluzi. Isto tako, prisustvo pred-malignog tkiva može utjecati na sastav bronhijalne sluzi. Ovo su teme daljih istraživačkih napora u ovoj oblasti. Detaljne informacije prikupljene u ovoj studiji mogu biti valjane za interpretaciju Ramanovih spektara dobivenih pomoću fiber-opticke sonde u budićim *in vivo* eksperimentima. Slične studije patoloških promjena bronhijalnog tkiva (npr. maligniteti i pred-maligniteti) doprinijeti će razvoju dijagnostičke primjene Ramanove spektroskopije.

### *Razlikovanje tkiva tumora od normalnog tkiva: određivanje resekcionih margina*

Kompletna resekcija je tretman izbora za većinu tumora. Primjer je meningiom, tumor moždanih ovojnica, koji iako obično dobroćudan može lokalno recidivirati ukoliko nije potpuno odstranjen. Petnaestogodišnja stopa povrata tumora nakon hirurske resekcije meningioma može preći 30%.<sup>16</sup> U poređenju sa primarnim meningiomom njegovi recidivi su često zloćudni. U klasičnom Simpsonovom radu iz 1950 godine, navedeno je da su rezidualna žarišta meningioma unutar regionalnih moždanih ovojnica, uglavnom uzročnici povratka tumora.<sup>17</sup> Ovaj stav potvrđen je u kasnijim studijama.<sup>18,19</sup> Za sada ne postoje objektivna per-operativna sredstva koja mogu potvrditi da li je kompletno tkivo tumora odstranjeno iz marginalnih moždanih ovojnica. U Poglavlju 3, opisana je jedna mapping studija koja primjenjuje Ramanovu spektroskopiju na zamrznutim isječcima ljudske moždane ovojnice (lat. dura) i tkiva meningioma. Rezultati su pokazali da se meningiom i zdrava dura jasno razlikuju po njihovim Ramanovim spektrima. Porijekloovih spektralnih razlika se može se objasniti visokim postotkom kolagena u duri i povećanim postotkom lipida u tkivu tumora. Model klasifikacije dure i tkiva tumora zasnovan na Linearnoj Diskriminativnoj Analizi Ramanovih spektara dao je 100% tačnost. Također je napravljena analiza za procijenu minimalne količine tkiva tumora u duri koju je još moguće detektirati. Ovi preliminarni rezultati mogu poslužiti kao osnova za razvoj jedne *in vivo* Ramanove spektroskopske metode da se per-operativno ispituju resekcione margine moždanih ovojnica i tako smanji stopa recidiva meningioma.

### *Klasifikacija heterogenosti tumora: vođenje biopsijske procedure za optimalno uzimanje tkivnog uzorka*

Dijagnostički i hirurški postupci su potpomognuti i vođeni metodama kompjuterske tomografije (CT) ili magnetne rezonance (MRI). Ove tehnike generalno ne pružaju informacije o histološkom sastavu kao niti o dinamičkim promjenama do kojih dolazi tokom hirurških postupka (npr. pomicanje mozga izazvano edema ili nakon otklanjanja (tumorskog) tkiva). Ovakve promjene u lokalnoj anatomiji mogu omesti preciznost hirurškog zahvata što također može povećati rizik oštećenja zdravih tkiva.<sup>20-28</sup> U novije vrijeme, intra-operativna MRI je predstavljena kao efektivna tehnika za navigiranje neurohirurških intervencija. Međutim, efikasna primjena intra-operativne MRI je sprijećena potrebom za MR-kompatibilnim

instrumentima i operacionim salama zaštićenim od radiofrekvencije. Pored toga, troškovi i veličina intra-operativnih MRI sistema su zabrinjavajući.<sup>28</sup> Problem nedovoljne preciznosti pri uzimanju tkivnog uzorka za diagnostičke svrhe tretiran je u jednoj *in vitro* Ramanovoj spektroskopskoj mapping studiji na glioblastomu (stupanj IV gliom), koji je jedan od najfrekventnijih i najzloćudnijih primarnih tumora mozga (Poglavlje 4). Histološki stupanj malignosti glioma zavisi od prisustva tkivnih promjena kao što su endotelialna proliferacija i nekroza, koje su često neravnomjerno raspoređene unutar tumora. Pošto se uzorci tkiva dobiveni stereotaktičkom biopsijom relativno mali, greške se mogu lako desiti zbog nedostatka ovih ključnih obilježja u bioptu. Na primjer, obilježje nekroze je važno za gradiranje glioma, ali uzorci koji sadrže samo nekrozu dijagnostički su beskorisni te je ponovna biopsija često neminovna.

Rezultati ovdje opisane Ramanove spektroskopske mapping studije indicirali su da biohemijske informacije koje pružaju Ramanovi spektri omogućavaju razlikovanje nekrotičnog tkiva od vitalnog tkiva glioma. Klasifikacioni model na temelju Linearne Diskriminativne Analize, razvijen u ovoj *in vitro* studiji, omogućio je razlikovanje vitalnog tkiva glioblastoma i nekrotičnog tkiva sa 100% tačnošću. Biohemijske razlike između nekroze i vitalnog tkiva glioblastoma, kako je utvrđeno Ramanovom spektroskopijom, poklapaju se sa podacima u literaturi<sup>35-44</sup> i pružaju informacije o histološkom porijeklu ovih razlika. Ovi rezultati najavljuju razvoj *in vivo* Ramanove spektroskopske metode za poboljšanje intra-operativnog vođenja biopsije mozga. Ciljana biopsija putem Ramanove spektroskopije može suštinski utjecati na histopatološku dijagnozu, koja je ključna za izbor tretmana i prognozu glioma. Premda komplikacije koje prate stereotaktičku biopsiju mozga nisu česte, ova procedura nije potpuno bez rizika (npr. krvavljenja ili oštećenja zdravog tkiva) za pacijenta.<sup>45</sup> Primjenom Ramanove biopsije može se smanjiti broj ne diagnostičkih stereotaktičnih biopsija. Uz to, primjena će biti korisna u razlikovanju radiacijske nekroze od vitalnog tkiva glioma kod pacijenata sa recidivom tumora, podloženim radioterapiji.

### *Optimalizacija Ramanove spektroskopije za primjenu in vivo: konstrukcija tzv. "singel fiber-optic probe"*

Iako su različite minijaturne fiber-optičke sonde dizajnirane,<sup>46-48</sup> aktualna primjena konvencionalne Ramanove spektroskopije za upotrebu *in vivo* u kliničke svrhe bila je zadugo nemoguća. Razlog tome jeste činjenica da su Ramanove fiber-optičke sonde bile prilično komplicirane i teško ih je (bilo) proizvoditi tako da bi se mogli omogućiti reproduktivni rezultati. Problem je u tome što je sama optička vlakna generiraju jak pozadinski Ramanov signal. Nažalost, sonde opremljene da mogu eliminirati pozadinski signal su složene, krute i teško ih je minimizirati. Pored toga, intenzitet signala u tzv. fingerprint spektralnom području ( $400-2000\text{ cm}^{-1}$ ) je relativno nizak, zahtijevajući dugo vrijeme mjerenja što je nepraktično za kliničku upotrebu.

Završna poglavlja ove teze opisuju naše napore u pravcu razvoja tankih fiber-optičkih sondi za *in vivo* mjerenje Ramanovog tkivnog spektra. Solucija koju smo istražili jeste da se koristi područje visoke talasne dužine (engl. high wavenumber, HWVN) Ramanovog spektra ( $2000-4000\text{ cm}^{-1}$ ). Interesantno je da se u ovom spektralnom području generira malo ili nimalo pozadinskog signala u sondi. Time se omogućava veoma jednostavan dizajn fiber-optičkih sondi. Ranije su HWVN regiju koristili Wolthius *et al.* i Caspers *et al.* za mjerenje koncentracija vode u moždanom tkivu<sup>49</sup> i u koži.<sup>50</sup> Također su van de Poll *et al.* dobili veoma detaljnu informaciju o sastavu i heterogenosti aterosklerotičkih ploča upotrebom HWVN regiona Ramanovog spektra.<sup>51</sup> U ovdje opisanom radu (Poglavlje 5) najprije smo ispitali da li je HWVN Ramanova spektroskopija u stanju osigurati dovoljno informacija za razlikovanje morfoloških struktura u različitim tkivima (glioblastomu, meningiomu i tkivu normalnog mokraćnog mjehura) u poređenju sa “fingerprint” regijom. Ramanovi mapping eksperimenti izvedeni upotrebom “fingerprint” i HWVN spektralne regije međusobno su upoređeni. Pokazalo se da u mnogim slučajevima HWVN Ramanova spektroskopija omogućava isti supanj razlikovanja tkiva i daje iste relevantne informacije kao Ramanova spektroskopija u “fingerprint” regionu. Ovi rezultati podudarili su se sa našim ciljem da se minijaturiziraju fiber-optičke sonde što je neophodno za njihovu intravaskularnu<sup>8,46</sup> ili intracerebralnu primjenu (npr. stereotaktička biopsija mozga) sa reproduktivnim rezultatima.<sup>52</sup> Ključno je zadržati fleksibilnost sondi kada ih se koristi u kanalu endoskopa.<sup>10</sup> Također je neophodno omogućiti proizvodnju sondi za jednokratnu upotrebu. Zasada, male i fleksibilne Ramanove sonde još uvijek nisu dostupne na tržištu. Mi smo konstruirali aparat za Ramanovu spektroskopsku karakterizaciju tkiva u HWVN regiji, koji posjeduje samo jednu, nefiltriranu optičku sondu koja navodi lasersko svjetlo na uzorak, sakuplja rasijano svjetlo i navodi ga na spektrometar (Poglavlje 6). Nekoliko tipova optičkih sondi testirano je za Ramanov pozadinski signal. Premda su sastavi srži i obloge primarno odgovorni za djelotvornost optičke sonde, također su analizirani različiti vanjski materijali budući da oni mogu utjecati na ukupno ponašanje sonde. Fuzirana silikatna optička sonda sa akrilnom oblogom pokazala se kao najučinkovitija kombinacija.

Ramanov fiberoptički uređaj bio je testiran *ex vivo* na svježem svinjskom mozgu (Poglavlje 7). Rezultati ove studije pokazali su da ovaj uređaj omogućava identifikaciju i razlikovanje struktura mozga na osnovi razlika u njihovom biohemijском sastavu. Hijerarhijska Kluster Analiza (engl. Chierarchical Cluster Analysis) je korištena da bi se dobile informacije o različitim spektarima različitih područja mozga. Razlike sadržane u Ramanovim spektrima analizirane su tzv. “least squares fitting” procedurom. Ovo je rezultiralo jasnom separacijom Ramanovih spektara bijele i sive moždane tvari predstavljajući razlike u njihovom biohemijском sastavu. U poređenju sa bijelom moždanom tvari, Ramanov spektar sive tvari karakteriziran je prisustvom jakog signala proteina, DNK i fosfatidilholina što se može objasniti činjenicom da se siva moždana tvar većim dijelom sastoji od nervnih ćelija.<sup>53</sup> U spektrima dobivenim od bijele moždane tvari, najjači signal dolazi od lipida kao što su

holesterol, sfingomyelin i glaktocerebrosid. Ovo je očekivano jer se bijela tvar sastoji od obilja myelina, koji je lipoprotein sačinjen od 70 do 85% lipida.<sup>54</sup> Unatoč tome su spektralne razlike između pojedinih područja bijele moždane tvari (npr. fimbria hippocampi i tractus opticus, bijela tvar malog- i velikog mozga) bile male, ovi dijelovi mozga su ipak bili međusobno razlikovani. Detaljna analiza je pokazala da ove razlike proizlaze iz varijacija u signalnim doprinosima lipida, što najvjerojatnije odražava razlike u stupnju myelinizacije ovih područja bijele moždane tvari. Pored toga je i jedan broj područja sive tvari (npr. bazalna jezgra) bio međusobno razdvojen, što se također temelji na različitostima u biohemijom sastavu. Odnos u signalnom doprinosu iz proteina i lipida je bio odlučujući, što se na svu vjerojatnoću, da objasniti količinom myeliniziranih vlakana koja prolaze kroz područja sive tvari.<sup>53</sup> Preciznost Ramanovih mjerenja za manje i/li tanje moždane strukture (npr. nucleus ruber, substantia nigra, tractus opticus), bila je poremećena efektivnom mjernom zapreminom sonde. Još uvijek nisu izvršene sistematske studije na mjernoj zapremini sonde u moždanom tkivu. Vjerojatno je da je signal iz manjih struktura bio jednim dijelom dobiven iz susjednih moždanih struktura radi nepreciznog pozicioniranja sonde ili radi toga što je efektivna mjerna zapremina sonde bila veća od ispitivane strukture. Ovaj problem treba detaljnije istražiti u budućim studijama.

Rezultati pokazuju da korištenje jednostruke fiber-optičke sonde i HWVN dijela spektra mogu dati jedan relativno lak i povjerljiv *in vivo* Ramanov sistem za diferencijaciju različitih moždanih struktura.

Nedavno su Nijssen *et al.* napravili važan korak u razvoju kliničko-dermatološke primjene Ramanove fiber-optičke spektroskopije.<sup>56</sup> U njihovoj studiji je pokazano da Ramanov HWVN uređaj opisan u ovoj tezi može sa visokom tačnošću razlikovati karcinom bazalne ćelije od susjedne zdrave kože. Primjene *in vivo* Ramanove fiber-optičke spektroskopije koje mogu biti predočene uključuju vođenje laparoskopskih procedura, identifikaciju pred-malignih promjena tkiva, nadziranje učinka lokalne i sistemske terapije (npr. radio- i kemoterapije) te intravaskularnu detekciju aterosklerotičkih pločica i raspoznavanje njihovog sastava.

Ova teza je odraz naših napora da se Ramanova spektroskopija napravi podobnom za ovakve *in vivo* primjene u kliničkoj praksi. Ramanova spektroskopija može na ovaj način postati dragocjeno dodatno sredstvo za lakše, brže i tačnije diagnosticiranje u kliničko-patološkoj praksi.

## References

1. Puppels GJ, de Mul FF, Otto C, Greve J, Robert-Nicoud M, Arndt-Jovin DJ, Jovin TM. *Studying single living cells and chromosomes by confocal Raman microspectroscopy*. *Nature* 1990; 347: 301-303.
2. Mahadevan-Jansen A, Mitchell MF, Ramanujam N, Malpica A, Thomsen S, Utzinger U, Richards-Kortum R. *Near-infrared Raman spectroscopy for in vitro detection of cervical precancers*. *Photochem Photobiol* 1998; 68: 123-132.
3. Shetty G, Kendall C, Shepherd N, Stone N, Barr H. *Raman spectroscopy: elucidation of biochemical changes in carcinogenesis of oesophagus*. *Br J Cancer* 2006; 22: 1460-4.
4. Stone N, Kendall C, Smith J, Crow P, Barr H. *Raman spectroscopy for identification of epithelial cancers*. *Faraday Discuss* 2004; 126: 141-157.
5. Kendall C, Stone N, Shepherd N, Geboes K, Warren B, Bennett R, Barr H. *Raman spectroscopy, a potential tool for the objective identification and classification of neoplasia in Barrett's oesophagus*. *J Pathol* 2003; 200: 602-609.
6. Stone N, Stavroulaki P, Kendall C, Birchall M, Barr H. *Raman spectroscopy for early detection of laryngeal malignancy: preliminary results*. *Laryngoscope* 2000; 110: 1756-1763.
7. Malini R, Venkatakrishna K, Kurien J, Pai KM, Rao L, Kartha VB, Krishna CM. *Discrimination of normal, inflammatory, premalignant, and malignant oral tissue: a Raman spectroscopy study*. *Biopolymers* 2006; 81: 179-193.
8. Buschman R, Marple ET, Wach ML, Bennett B, Bakker Schut TC, Bruining HA, Bruschke AV, van der Laarse A, Puppels GJ. *In vivo determination of the molecular composition of artery wall by intravascular Raman spectroscopy*. *Anal Chem* 2000; 72: 3771-3775.
9. Bakker Schut TC, Witjes M, Sterenborg M, Speelman O, Roodenburg J, Marple E, Bruining HA, Puppels GJ. *In vivo detection of dysplastic tissue by Raman spectroscopy*. *Anal Chem* 2000; 72: 6010-6018.
10. Molckovsky A, Wong Kee Song L-M, Shim MG, Marcon NE, Wilson BC. *Diagnostic potential of near-infrared Raman spectroscopy in the colon: differentiating adenomatous from hyperplastic polyps*. *Gastrointestinal Endoscopy* 2003; 57: 396-402.
11. Widdicombe JG. *Role of lipids in airway function*. *Eur J Respir Dis* 1987; 71: 197-204.
12. Roussel P, Degand P, Lamblin G, Laine A, Lafitte J.J. *Biochemical definition of human tracheobronchial mucus*. *Lung* 1978; 154: 241-260.
13. Widdicombe JH, Widdicombe JG. *Regulation of human airway surface liquid*. *Respiration Physiology* 1995; 99: 3-12.
14. Kim KC, Opaskar-Hincman H, Bhaskar KR. *Secretions from primary hamster tracheal surface epithelial cells in culture: mucine-like glycoproteins, proteoglycans, and lipids*. *Exp Lung Res* 1989; 15: 299-314.
15. Reid LM, Bhaskar KR. *Macromolecular and lipid constituents of bronchial epithelial mucus*. *Symp Soc Exp Biol* 1986; 43: 201-219.
16. Mirimanoff RO, Dosoretz DE, Linggood RM, Ojemann RG, Martuza RL. *Meningioma: analysis of recurrence and progression following neurosurgical resection*. *J Neurosurg* 1985; 62: 18-24.
17. Simpson D. *The recurrence of intracranial meningiomas after surgical treatment*. *J Neurol Neurosurg Psychiatry* 1957; 20: 22-39.
18. Borovich B, Doron Y. *Recurrence of intracranial meningiomas: the role played by regional multicentricity*. *J Neurosurg* 1986; 64: 58-63.
19. Jaaskelainen J. *Seemingly complete removal of histologically benign intracranial meningioma: late recurrence rate and factors predicting recurrence in 657 patients. A multivariate analysis*. *Surg Neurol* 1986; 26: 461-469.

20. Black PM, Moriarty T, Alexander E, Stieg P, Woodard E, Gleason PL, Martin CH, Kikinis R, Schwartz RB, Jolesz FA. *Development and implementation of intraoperative magnetic resonance imaging and its neurosurgical applications*. Neurosurgery 1997; 41: 831-845.
21. Seifert V, Zimmermann M, Trantakis C, Vitzthum H-E, Kühnel K, Raabe A, Bootz F, Schneider J-P, Schmidt F, Dietrich J. *Open MRI-guided neurosurgery*. Acta Neurochir (Wien) 1999; 141: 455-464.
22. Zimmermann M, Seifert V, Trantakis C, Kühnel K, Raabe A, Schneider J-P, Dietrich J, Schmidt F. *Open MRI-guided microsurgery of intracranial tumours. Preliminary experience using a vertical open MRI-scanner*. Acta Neurochir (Wien) 2000; 142: 177-186.
23. Zimmermann M, Seifert V, Trantakis C, Raabe A. *Open MRI-guided microsurgery of intracranial tumours in or near eloquent brain areas*. Acta Neurochir (Wien) 2001; 143: 327-337.
24. Nimsky C, Ganslandt O, Cerny S, Hastreiter P, Greiner G, Fahlbusch R. *Quantification of, visualization of, and compensation for brain shift using intraoperative magnetic resonance imaging*. Neurosurgery 2000; 47: 1070-1080.
25. Nimsky C, Ganslandt O, Hastreiter P, Fahlbusch R. *Intraoperative magnetic resonance imaging combined with neuronavigation: a new concept*. Surg Neurol 2001; 56: 357-365.
26. Hastreiter P, Rezk-Salama C, Soza G, Bauer M, Greiner G, Fahlbusch R, Ganslandt O, Nimsky C. *Strategies for brain shift evaluation*. Med Image Anal 2004; 8: 447-464.
27. Albayrak B, Samdani AF, Black PM. *Intra-operative magnetic resonance imaging in neurosurgery*. Acta Neurochir (Wien) 2004; 146: 543-557.
28. Iseki H, Muragaki Y, Nakamura R, Ozawa N, Taniguchi H, Hori T, Takakura K. *Intelligent operating theater using intraoperative open-MRI*. Magn Reson Med Sci 2005; 4: 129-136.
29. Apuzzo ML, Sabshin JK. *Computed tomographic guidance stereotaxis in the management of intracranial mass lesions*. Neurosurgery 1983; 12: 277-285.
30. Barnett GK, Kormos DW, Steiner CP, Weisenberger J. *Use of a frameless, armless stereotactic wand for brain tumor localization with two-dimensional and three-dimensional neuroimaging*. Neurosurg 1993; 33: 674-678.
31. Dorward NL, Alberti O, Velani B, Gerritsen FA, Harkness WF, Kitchen ND, Thomas DG. *Postimaging brain distortion: magnitude, correlates, and impact on neuronavigation*. J Neurosurg. 1998; 88: 656-662.
32. Roberts DW, Hartov A, Kennedy FE, Miga MI, Paulsen KD. *Intraoperative brain shift and deformation: a quantitative analysis of cortical displacement in 28 cases*. Neurosurgery 1998; 43: 749-760.
33. Sibbain NA, Howe FA, Saunders DE. *The clinical value of proton magnetic resonance spectroscopy in adult brain tumours*. Clinical Radiology 2007; 62: 109-119.
34. Martin W. *MR Spectroscopy in Neurodegenerative Disease*. Mol Imaging Biol 2007; 9: 196-203.
35. Campanella R. *Membrane lipids modifications in human gliomas of different degree of malignancy*. J Neurosurg Sci 1992; 36: 11-25.
36. Gopal K, Grassi E, Paoletti P, Usardi M. *Lipid composition of human intracranial tumors: a biochemical study*. Acta Neurochir (Wien) 1963; 11: 334-347.
37. Barba I, Cabañas ME, Arús C. *The relationship between Nuclear Magnetic Resonance-visible lipids, lipid droplets, and cell proliferation in cultured C6 cells*. Cancer Res 1999; 59: 1861-1868.
38. Nygren C, von Holst H, Månsson J-E, Fredman P. *Increased levels of cholesterol esters in glioma tissue and surrounding areas of human brain*. Br J Neurosurg 1997; 11: 216-220.
39. Nagedank WG, Sauter R, Brown TR, Evelhoch JL, Falini A, Gotsis ED, Heerschap A, Kamada K, Lee BC, Menger MM, Moser E, Padavic-Shaller KA, Sanders JA, Spraggins TA, Stillman AE, Terwey B, Vogl TJ, Wicklow K, Zimmerman RA. *Proton magnetic resonance spectroscopy in patients with glial tumors: a multicenter study*. J Neurosurg 1996; 84: 449-458.

40. Galarraga J, Loreck DJ, Graham JF, DeLaPaz RL, Smith BH, Hallgren D, Cummins CJ. *Glucose metabolism in human gliomas: correspondence of in situ and in vitro metabolic rates and altered energy metabolism*. *Metab Brain Dis* 1986; 1: 279-291.
41. Hirakawa T, Maruyama K, Kohl NE, Kodama T, Ruley EH. *Massive accumulation of neutral lipids in cell conditionally transformed by an activated H-ras oncogene*. *Oncogene* 1991; 6: 289-295.
42. Rémy C, Fouilhé, Barba I, Sam-Lai E, Lahrech H, Cucurella M-G, Izquierdo M, Moreno A, Ziegler A, Massarelli R, Décorps M, Arús C. *Evidence that mobile lipids detected in rat brain glioma by 1H nuclear magnetic resonance correspond to lipid droplets*. *Cancer Res* 1997; 57: 404-414.
43. Ross BD, Higgins RJ, Boggan JE, Willis JA, Knittel B, Unger SW. *Carbohydrate metabolism of the rat C6 glioma. An in vivo 13C and in vitro 1H magnetic resonance spectroscopy study*. *NMR Biomed* 1988; 1: 20-26.
44. Mizuno A, Kitajima H, Kawauchi K, Muraishi S, Ozaki Y. *Near-Infrared Transform Raman spectroscopic study of human brain tissues and tumors*. *J Raman Spect* 1994; 25: 25-29.
45. Field M, Witham TF, Flickinger JC, Kondziolka D, Lunsford LD. *Comprehensive assessment of hemorrhage risks and outcomes after stereotactic brain biopsy*. *J Neurosurg* 2001; 94: 545-551.
46. Motz JT, Hunter M, Galindo LH, Gradecki JA, Kramer JR, Dasari RR, Feld MS. *Optical fiber probe for biomedical Raman spectroscopy*. *Appl Opt* 2004; 20: 542-554.
47. Shim MG, Song LM, Marcon NE, Wilson BC. *In vivo near-infrared Raman spectroscopy*. *Photochem Photobiol* 2000; 72: 146-150.
48. Puppels GJ, van Aken M, Wolthuis R, Caspers PJ, Bakker Schut TC, Bruining HA, Romer TJ, Buschman HPJ, Wach M, Robinson JS. *In vivo tissue characterization by Raman spectroscopy*. *Proc SPIE Biomed Soc* 1998; 3257: 78-85.
49. Wolthuis R, van Aken M, Fountas K, Robinson Jr JS, Bruining HA, Puppels GJ. *Determination of water concentration in brain tissue by Raman spectroscopy*. *Anal Chem* 2001; 73: 3915-3920.
50. Caspers PJ, Lucassen GW, Carter EA, Bruining HA, Puppels GJ. *In vivo confocal Raman microspectroscopy of skin: noninvasive determination of molecular concentration profiles*. *J Invest Dermatol* 2001; 116: 434-442.
51. van de Poll SWE, Moelker A, Wolthuis R, Bakker Schut TC, Koljenovi S, van der Laarse A, Puppels GJ. *Chemical characterization of atherosclerotic plaque by high-wavenumber Raman spectroscopy*, (unpublished results).
52. Boere IA, Bakker Schut TC, van den Boogert J, de Bruin RWF, Puppels GJ. *Use of fiber optic probes for detection of Barrett's epithelium in the rat oesophagus by Raman spectroscopy*. *Vibrational Spectroscopy* 2003; 32: 47-55.
53. Haines DE. In: *Fundamental Neuroscience*, Haines DE, Editor; Churchill Livingstone: New York, 1997, 1-8.
54. Agranoff BW, Benjamins JA, Hajra AK. In: *Basic Neurochemistry*; Siegel GJ, Agranoff BW, Albers RW, Fisher SK, Uhler MD, Eds.; Lippincott Williams & Wilkins: Philadelphia, 1999, 47-69.
55. Puppels GJ, Bakker Schut TC, Caspers PJ, Wolthuis R, van Aken M, van der Laarse A, Bruining HA, Buschman H, Shim MG, Wilson BC. In: *"Handbook for Raman spectroscopy"*; Lewis IR and Edwards HGM, Eds.; Marcel Dekker, Inc: New York, 2001, 549-574.
56. Nijssen A, Maquelin K, Santos LF, Caspers PJ, Bakker Schut TC, den Hollander JC, Neumann MH, Puppels GJ. *Discriminating basal cell carcinoma from perilesional skin using high wave-number by Raman spectroscopy*. *J Biomed Opt* 2007; 12: 034004.

## Curriculum vitae

Senada Koljenović is op 21 juni 1968 geboren in Ivangrad, Montenegro (ex-Joegoslavië). In 1985 behaalde zij het diploma aan het Gymnasium “Braća Ribar” te Sarajevo (Bosnië en Herzegovina). In datzelfde jaar is zij met de studie Geneeskunde begonnen aan de Universiteit Sarajevo. In het eindjaar, 1992, werd haar studie onderbroken en in 1994 is zij naar Nederland gekomen, alwaar zij in 1996 opnieuw begon met de studie Geneeskunde aan de Erasmus Universiteit te Rotterdam. Tijdens haar afstudeeronderzoek maakte zij kennis met Ramanspectroscopie bij het Centrum voor Optische Diagnostiek en Therapie van het Erasmus Medisch Centrum te Rotterdam. Na het behalen van het doctoraalexamen deed zij, gedeeltelijk in de avonduren, promotieonderzoek bij voornoemde onderzoeksgroep van 2000 tot 2006. Het onderzoek werd verricht onder begeleiding van Dr.ir. G.J. Puppels en Dr.ir. T.C. Bakker Schut, in samenwerking met de afdelingen Pathologie (Prof.dr. J.M. Kros en Prof.dr. J.W. Oosterhuis), Neurochirurgie, Thoraxchirurgie en Longziekten. Gedurende deze periode werd in 2004 de studie Geneeskunde afgerond. Sinds april 2004 is zij in opleiding tot klinisch patholoog aan het Erasmus Medisch Centrum, Josephine Nefkens Instituut met Dr. M.A. den Bakker als opleider.



## Publications

Koljenović S, Choo-Smith LP, Bakker Schut TC, Kros JM, van den Berge HJ, Puppels GJ. Discriminating vital tumor from necrotic tissue in human glioblastoma tissue samples by Raman spectroscopy. *LAB INVEST.* 2002 OCT; 82 (10): 1265-1277.

Koljenović S, Bakker Schut TC, van Meerbeeck JP, Maat AP, Burgers SA, Zondervan PE, Kros JM, Puppels GJ. Raman microspectroscopic mapping studies of human bronchial tissue. *J BIOMED OPT.* 2004 NOV-DEC; 9 (6): 1187-1197.

Koljenović S, Bakker Schut TC, Wolthuis R, de Jong B, Santos L, Caspers PJ, Kros JM, Puppels GJ. Tissue characterization using high wave number Raman spectroscopy. *J BIOMED OPT.* 2005 MAY- JUN; 10 (3): 031116.

Santos LF, Wolthuis R, Koljenović S, Almeida RM, Puppels GJ. Fiber-optic probes for in vivo Raman spectroscopy in the high-wavenumber region. *ANAL CHEM.* 2005 OCT 15; 77 (20): 6747- 6752.

Koljenović S, Bakker Schut TC, Vincent AJ, Kros JM, Puppels GJ. Detection of meningioma in dura mater by Raman spectroscopy. *ANAL CHEM.* 2005 DEC 15; 77 (24): 7958- 7965.

Koljenović S, Bakker Schut TC, Wolthuis R, Vincent AJ, Hendriks-Hagevi G, Santos L, Kros JM, Puppels GJ. Raman Spectroscopic Characterization of Porcine Brain Tissue Using a Single Fiber-Optic Probe. *ANAL CHEM.* 2007 JAN 15; 79 (2): 557- 564.

